Dissertation zur Erlangung des Doktorgrades
der Fakultät für Chemie und Pharmazie
der Ludwig-Maximilians-Universität München

Low-dimensional transition metal chalcogenides

Synthesis and characterization of β-FeSe- and Fe_3GeTe_2-related structures

Juliane Stahl

aus
Bochum, Deutschland

2019

Erklärung

Diese Dissertation wurde im Sinne von §7 der Promotionsordnung vom 28. November 2011 von Herrn Prof. Dr. Dirk Johrendt betreut.

Eidesstattliche Versicherung

Diese Dissertation wurde eigenständig und ohne unerlaubte Hilfe erarbeitet.

München, 17.01.2020

Juliane Stahl

Dissertation eingereicht am 24.10.2019
1. Gutachter: Prof. Dr. Dirk Johrendt
2. Gutachter: Prof. Dr. Wolfgang Schnick
Mündliche Prüfung am 03.12.2019

Danksagung

Zu allererst möchte ich mich bei Prof. Dr. Dirk Johrendt für die ausgezeichnete Betreuung während der Anfertigung dieser Dissertation bedanken. Vor allem für die Freiheit die Arbeit zu meiner zu machen, die Geduld und die immer offene Tür.

Herrn Prof. Dr. Wolfgang Schnick danke ich für die Übernahme der Zweitgutachtens. Für die Teilnahme an der Prüfungskommission danke ich außerdem Herrn Prof. Dr. Oliver Oeckler, Herrn Prof. Dr. Stefan Schwarzer, Herrn Prof. Dr. Konstantin Karaghiosoff und Herrn Prof. Dr. Hans-Christian Böttcher.

Vielen Dank an Lukas Neudert und Oliver Oeckler für die Aufnahme und Interpretation von TEM-Daten sowie an Theresa Block, Rainer Pöttgen und Hans-Henning Klauß für diverse Mößbauer-Messungen. Arthur Haffner danke ich für seine Unermüdlichkeit bei der Aufnahme von Einkristall-Beugungsdaten.

Meinen Praktikantinnen Linh Nguyen, Evgeniya Shlaen, Helena Singer, Victoria Laura Di Bacco und Tabea Haug bin ich sehr dankbar für ihr Mitwirken an dieser Dissertation.

Ich danke allen Mitgliedern des AK Johrendt mit denen ich in den letzten Jahren zusammenarbeiten durfte, Gina Friederichs, Arthur Haffner, Franziska Hummel, Catrin Löhnert, Ursula Pachmayr, Simon Peschke, Roman Pobel, Tobias Rackl, Bettina Rendenbach, Marlo Schöneich, Rudolf Schönmann, Christine Stürzer, Tobias Stürzer, Valentin Weippert und Erwin Wiesenmayer. Dank euch allen hatte ich eine wunderbare Zeit, in und außerhalb des Labors. Danke *Muddi*, dass du immer da bist, egal ob es um forscherische oder andere Problemstellungen geht. Danke Betti, dass du so

bist wie du bist und ich mit dir eine so gute Freundin finden durfte. Danke Tobi, dass du die ganze Zeit über an meiner Seite bzw. in meinem Rücken geblieben bist.

Ich bedanke mich außerdem bei den ehemaligen und aktuellen Mitgliedern der Arbeitskreise Schnick, Hoch und Lotsch für viele schöne Erlebnisse und sehr viele gemeinsame Stunden in der Kaffeeküche.

Thomas Miller und Wolfgang Wünschheim danke ich dafür, dass sie für die verschiedensten Probleme immer eine Lösung parat hatten und ihre unentwegt geduldige Hilfe.

Bei Fabian Keßler, Robin Niklaus, Tobias Rackl und Bettina Rendenbach bedanke ich mich für das Korrekturlesen dieser Arbeit. Patrick Jüstel danke ich für die regelmäßige Beratung aus der Sichtweise eines Organikers.

Für ihre Freundschaft während des Studiums und der inzwischen doch schon langen Zeit danach danke ich meinen ehemaligen Kommilitonen Sabine Auras, Martin Grundei, Patrick Jüstel, Fabian Keßler, Leonhard Kick und Anne Schulz. Danke, dass ich mir sicher sein kann, dass wir uns auch in den kommenden Jahren nicht aus den Augen verlieren werden.

Meiner Familie danke ich für die unaufhörliche Unterstützung in allen Lebenslagen. Danke Mattea, dass du so oft schon verstehst was ich sagen will bevor ich es überhaupt ausgesprochen habe und für deine stete Hilfe bei den erstaunlich häufig auftretenden, gestalterischen Fragestellungen im Laufe dieser Arbeit. Danke Mama, dass du immer von Anfang an weißt, dass alles gut laufen wird und dafür, dass nach Hause kommen jedesmal alle Sorgen so viel kleiner macht. Danke Papa, dass du auf irgendeine Art und Weise immer da sein wirst.

Bei Patrick bedanke ich mich dafür, dass er immer alles leicht nimmt, auch für mich mit. Danke, dass du jeden Tag an meiner Seite bist.

"It is our choices, that show
what we truly are, far more than our abilities."

Albus Dumbledore

Table of Contents

1 Introduction

"Since solids bring to mind the idea of volume it may seem paradoxical to speak about *low-dimensional solids*, at least from the stand point of chemistry." (Jean Rouxel, 1996, p. 1)[1]

Existing in a three-dimensional world, the concept of lowered dimensionality is scarcely tangible. The term alone is already vague, since real two-, one- or zero-dimensional solids cannot exist. Therefore it is preferable to refer to this concept as anisotropy or quasi-dimensionality instead [Figure 1-1 turquoise box]. In addition, anisotropy of physical properties and anisotropy of the chemical structure must be considered separately, since they do not necessarily cohere.[1,2] In terms of anisotropic physical properties, examples range from simple mechanical motion, over electrical conductivity or optical response, to modern phenomena such as charge density waves or the quantum Hall effect.[1-3] This leads to a variety of potential applications, for instance in micromechanical systems, shape memory devices, solar-cells or waste-heat-recovery technologies.[4-10] The abundance of possibilities is steadily increased by new research fields concerned with design and fabrication of appropriate materials.[4] However, elaborating new approaches is not trivial, since the physical properties of a 3D bulk material are not mandatorily transferable to dimensionally reduced phases. In addition, completely unaccustomed physical properties can occur in low-dimensional systems.[1] Conversely, there are also long-range ordered physical phenomena, like magnetic order, which do not exist below 2D space at all.[11,12]

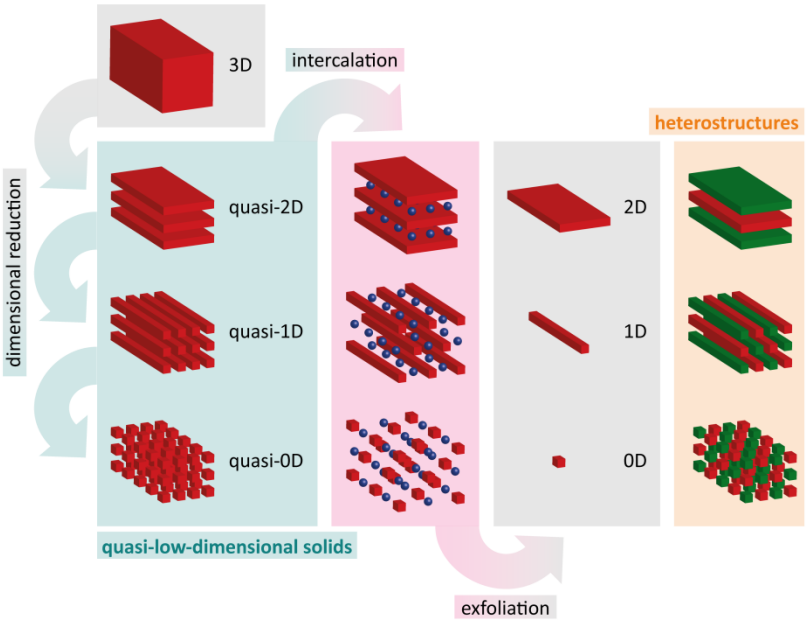

Figure 1-1 Schematic representation of dimensional reduction of a three-dimensional solid to quasi-low-dimensional structures [turquoise box], intercalation of neutral spacers into the van der Waals gaps [pink box], exfoliation to two-, one- and zero-dimensional solids [grey box] and heterostructures by juxtaposition of different low-dimensional structures [orange box].

When considering quasi-dimensionality from a chemical point of view, the presence of multiple types of chemical bonds in the crystal structure is decisive for its occurrence. Building blocks held together by strong chemical interaction, like covalent or metallic bonds, form extended motifs such as layers or chains. They are connected by weak van der Waals forces overcoming the Coulomb repulsion.[13] For this reason the term *van der Waals materials* has become established, especially for quasi-2D structures.[14,15] Examples of such layered compounds are numerous, comprising unary systems like graphene or silicene, binary materials like

h-BN or transition metal chalcogenides, or ternary metal chalcogenides and halides.[15] The richness of chemically and physically diverse quasi-two-dimensional compounds opens the possibility of combining these van der Waals materials to novel heterostructures, which, in turn, can exhibit unexpected properties [orange box in Figure 1-1].[14]

The construction of two-dimensional heterostructures, especially for application in electronic devices, has become the focus of current research, since quasi-2D materials cover the full range of electronic properties, from insulators to metals or even superconductors.[14,15] For design and fabrication, theoretical, physical and chemical methods complement each other to overcome difficulties arising in both manufacturing and characterization.[16] Nowadays, the most common methods of production divide into direct synthesis by chemical vapor deposition and manual stacking after exfoliation of quasi-2D precursors.[17] For the latter, the exfoliation technique depends on the corresponding compound and can be for instance mechanical, electrochemical or supported by solvent treatment or intercalation [pink box in Figure 1-1].[18-23] The task of chemists towards usable low-dimensional materials is therefore not only to synthesize new precursors, but also to find possibilities for weakening the van der Waals attraction with regard to exfoliation.

One of the best studied groups of low-dimensional solids are transition metal chalcogenides, since they exhibit a great variety of structures and physical properties. Considering only binary compounds, the most common structures are layered, with stoichiometries *MCh* or MCh_2.[15,24] The latter are composed of hexagonal layers of edge-sharing trigonal prismatic or octahedral MCh_6 polyhedra and are found in trigonal, hexagonal and rhombohedral polymorphs and different stacking variants.[25] The best known example of this group is MoS_2, which is a semiconduc-

tor as bulk material, but whose properties dramatically change for ultrathin crystals.[21,26] Through additional intercalation, heterostructuring or gating, a variety of properties, like photosensitivity, photo- and electrocatalytic activity, luminescence or transport inhibition are accessible. This gives rise to applications in solar cells, water electrolysis or field effect tunneling transistors.[26-32]

Stoichiometric transition metal chalcogenides, *MCh*, typically exhibit either a layered tetragonal or a three-dimensional hexagonal structure.[24] The tetragonal anti-PbO type is built up from layers of edge-sharing MCh_4 tetrahedra and is mostly found for the iron chalcogenides.[33-35] *β*-FeSe definitely represents the most intensely studied among these, since in 2008 superconductivity below 8 K has been detected for this compound [Figure 1-2 left].[36] It is the simplest compound within the family of iron based superconductors, since the structurally similar iron arsenides require intermediate layers to compensate the charge of the FeAs layers.[37] In terms of its physical characteristics, however, *β*-FeSe is not simple at all.[38] An iron based superconductor typically passes a tetragonal-to-orthorhombic phase transition, a nematic region and the emergence of an antiferromagnetic order upon cooling. Superconductivity is induced by suppression of this magnetic order through chemical doping or external pressure.[37,39] This is not true for *β*-FeSe, since apparently undoped samples show superconductivity. Furthermore, no magnetic order is observed upon cooling, whereas a phase transition to orthorhombic symmetry at 90 K and a nematic phase have been reported.[40-43] This is unusual, because it is widely assumed that these properties cohere.[38] An increase in the superconducting transition temperature of *β*-FeSe is achieved by intercalation of spacing layers into the van der Waals gap. These additional layers can consist of single cations to form $A_xFe_2Se_2$ [A = K, Rb, Cs, Tl; T_c up to 32 K], cointercalates with

organic molecules like in $A_x(NH_3)_yFe_2Se_2$ [A = Li, K, Rb, Cs, Ba; T_c up to 44 K] or $A_x(\text{diamine})_yFe_{2-z}Se_2$ [A = Li, Na, Sr; T_c up to 46 K], or quasi-2D layers as in $[(Li_{1-x}Fe_x)OH](Fe_{1-y}Li_y)Se$ [T_c = 43 K].[44-60] The T_c of pure β-FeSe also increases under hydrostatic pressure with a maximum of 37 K at 7 GPa.[61,62] The most remarkable findings, however, were transition temperatures above 100 K in single FeSe layers grown on $SrTiO_3$ substrates.[63,64] Although further investigations showed a strong dependence of T_c on the electronic doping by the substrate, the underlying mechanism leading to high T_c still remains inexplicable.[65,66] Due to this, β-FeSe still remains in the focus of research despite numerous studies published so far. With regard to exfoliation to thin films, solution-based processes and intercalation with neutral spacer layers to weaken the van der Waals interactions have also gained increasing scientific attention in recent years.

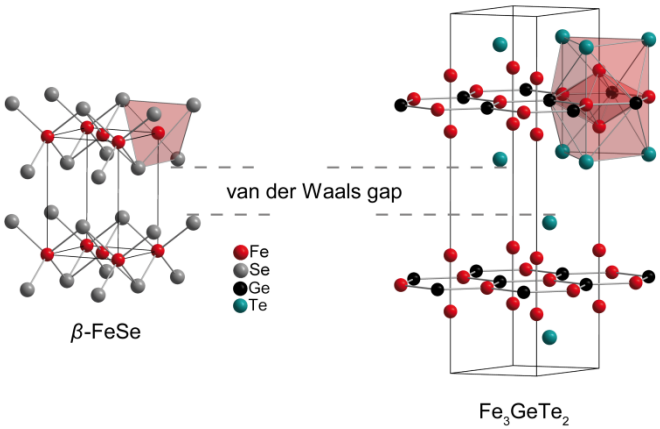

Figure 1-2 Crystal structures of the quasi-two-dimensional transition metal chalcogenides β-FeSe [left] and Fe_3GeTe_2 [right].

Looking at ternary transition metal chalcogenides, one group of quasi-two-dimensional compounds with a particularly large number of representatives stands out, the so called metal phosphorous trichalcogenides *M*P*Ch*$_3$. Their layers are composed of *MCh*$_6$ octahedra and P$_2$*Ch*$_6$ units and stacked to either build a rhombohedral or a monoclinic lattice.[67] The materials of this compound class cover a wide range of physical properties, with magnetic materials recently arousing increased interest. This is mainly caused by the fact that magnetism in 2D films has been realized despite the Mermin-Wagner theorem, which excludes magnetic ordering in low-dimensional solids.[11,68] The effect was first shown for monolayers of $FePS_3$ and the structurally similar compounds $CrSiTe_3$ and $Cr_2Ge_2Te_6$, which are all ferromagnetic in their bulk phases.[69-72] Although the properties are not necessarily preserved upon transition to single layers, many ferromagnetic quasi-2D compounds have since been investigated in order to obtain further two-dimensional magnets.[11] One of the most intensively studied compounds is the iron germanium chalcogenide Fe_3GeTe_2, with a Curie temperature of 230 K.[73-77] Its structure is composed of layered Fe-FeGe-Fe blocks separated by van der Waals gaps between the Te atoms [Figure 1-2 right]. The ferromagnetic order is retained when the structure is exfoliated, but associated with a lowering of T_C, depending on the method.[78-80] However, ionic gating raises the ordering temperature above room temperature, which demonstrates the great potential of Fe_3GeTe_2 thin films for application in magnetoelectronic devices.[80] The compound is even more interesting for future applications, since it has already been shown, that its properties can be further modified by substitution or intercalation. In $Fe_{3-\delta-x}Ni_xGeTe_2$ the magnetic ordering is continuously suppressed with increasing x due to dilution of the magnetic moments, while in $Fe_{3-\delta}Ge_{1-x}As_xTe_2$ the lowered transition temperature is attributed to structural changes.[77,81,82] In con-

trast to these substitutions, intercalation of Na atoms into the van der Waals gap only slightly changes T_C.[83] Altogether, through potential interplay of magnetic dilution, structural alteration and electronic doping *via* intercalation, numerous possibilities remain to further drive the system towards suitable 2D magnets.

This thesis is divided into two parts, both of which are based on quasi-two-dimensional transition metal chalcogenides, *β*-FeSe and Fe_3GeTe_2. In the first part solvothermal synthesis is presented as a method to obtain *β*-FeSe and dimensionally reduced phases. This method offers the advantage of relatively mild conditions and, at the same time, provides a multitude of parameters potentially affecting the products.[84] In chapter 2 ethylenediamine [*en*] is used as a solvent, which is known to dimensionally reduce the FeSe layers to quasi-1D chains by incorporation into the structure to form $Fe_3Se_4(en)_2$.[85] In chapter 2.1 a gradual reduction of the *β*-FeSe structure is achieved by diluting *en* with *glycerol* and thereby gaining close control over the ligand-to-metal ratio during synthesis. In this context the quasi-2D compound $Fe_{0.85}Se(en)_{0.3}$ and the quasi-1D compounds $Fe_{10}Se_{12}(en)_7$ and $Fe_3Se_4(en)_3$ were synthesized and characterized for the first time. $Fe_3Se_4(en)_3$ and $Fe_{0.85}Se(en)_{0.3}$ are examined in more detail in chapters 2.1.1 and 2.1.2, respectively. Since strong dependencies between the parameters in solvothermal synthesis are extant, chapter 2.2 concentrates on the influence of the dilution, especially on the reaction pressure. On this account, *glycerol* is replaced by methanol, which leads to incorporation into the double chain structure forming $Fe_{20}Se_{24}(en)_{13}$(MeOH). In chapter 3 *β*-FeSe is synthesized under solvothermal conditions using a mixture of propane-1,3-diamine [*1,3-dap*] and *glycerol*. The product is superconducting, which is not self-evident, as previous solvent-based attempts often led to non-

superconducting phases.[86,87] Furthermore, *β*-FeSe obtained by the solvothermal route in *1,3-dap* exhibits no tetragonal-to-orthorhombic phase transition, which has been considered to be crucial for superconductivity until today. The product is therefore carefully characterized and compared to samples produced by vapor-transport and hydrothermal synthesis.

In the second part of the thesis two new compounds closely related to Fe_3GeTe_2 are synthesized *via* solid state reactions. $Fe_{2.3}GeTe$ [chapter 4.1] and $Fe_{5-\delta}GeTe_2$ [chapter 4.2] are both quasi-two-dimensional with different numbers of atomic Fe and FeGe layers between the Te layers. Both compounds show stacking disorder and exhibit a ferromagnetic order upon cooling. Furthermore, the influence of Ni substitution on the magnetic order is investigated for the solid solution $Fe_{5-\delta-x}Ni_xGeTe_2$.

1 J. Rouxel, in *Physics and Chemistry of Low-Dimensional Inorganic Conductors*, Plenum Press, New York, **1996**, 1-14.

2 T. Cleason and M. Jonson, in *Low Dimensional Properties of Solids*, Physica Scripta/World Scientific, Gothenburg, **1992**, 3.

3 D. W. Bruce, D. O'Hare and R. I. Walton, *Low-Dimensional Solids*, Wiley, **2010**.

4 S. Fan, X. Feng, Y. Han, Z. Fan and Y. Lu, *Nanoscale Horiz.* **2019**, *4*, 781-788.

5 S. Hao, L. Cui, D. Jiang, X. Han, Y. Ren, J. Jiang, Y. Liu, Z. Liu, S. Mao, Y. Wang, Y. Li, X. Ren, X. Ding, S. Wang, C. Yu, X. Shi, M. Du, F. Yang, Y. Zheng, Z. Zhang, X. Li, D. E. Brown and J. Li, *Science* **2013**, *339*, 1191-1194.

6 H. S. Cho, K. J. Hemker, K. Lian, J. Goettert and G. Dirras, *Sens. Actuator A-Phys.* **2003**, *103*, 59-63.

7 R. Amer Moh, Y. Alaskar, H. Qasem, F. Alsaffar and A. Alhussain, *Nanotechnol. Rev.* **2016**, *5*, 549-566.

8 Z.-G. Chen, G. Han, L. Yang, L. Cheng and J. Zou, *Prog. Nat. Sci.* **2012**, *22*, 535-549.

9 M. S. Dresselhaus, G. Chen, M. Y. Tang, R. G. Yang, H. Lee, D. Z. Wang, Z. F. Ren, J.-P. Fleurial and P. Gogna, *Adv. Mater.* **2007**, *19*, 1043-1053.

10 A. J. Minnich, M. S. Dresselhaus, Z. F. Ren and G. Chen, *Energy Environ. Sci.* **2009**, *2*, 466-479.

11 M. Gibertini, M. Koperski, A. F. Morpurgo and K. S. Novoselov, *Nat. Nanotechnol.* **2019**, *14*, 408-419.

12 R. Peierls, *Math. Proc. Camb. Philos. Soc.* **2008**, *32*, 477-481.

13 J. Rouxel, in *Organic and Inorganic Low-Dimensional Crystalline Materials*, Springer, New York, **1987**, 1-16.

14 P. Ajayan, P. Kim and K. Banerjee, *Phys. Today* **2016**, *69*, 38-44.

15 D. L. Duong, S. J. Yun and Y. H. Lee, *ACS Nano* **2017**, *11*, 11803-11830.

16 W. Hu and J. Yang, *J. Mater. Chem. C* **2017**, *5*, 12289-12297.

17 M.-Y. Li, C.-H. Chen, Y. Shi and L.-J. Li, *Mater. Today* **2016**, *19*, 322-335.

18 V. Nicolosi, M. Chhowalla, M. G. Kanatzidis, M. S. Strano and J. N. Coleman, *Science* **2013**, *340*, 1226419.

19 C.-Y. Su, A.-Y. Lu, Y. Xu, F.-R. Chen, A. N. Khlobystov and L.-J. Li, *ACS Nano* **2011**, *5*, 2332-2339.

20 J. N. Coleman, M. Lotya, A. O'Neill, S. D. Bergin, P. J. King, U. Khan, K. Young, A. Gaucher, S. De, R. J. Smith, I. V. Shvets, S. K. Arora, G. Stanton, H.-Y. Kim, K. Lee, G. T. Kim, G. S. Duesberg, T. Hallam, J. J. Boland, J. J. Wang, J. F. Donegan, J.C. Grunlan, G. Moriarty, A. Shmeliov, R. J. Nicholls, J. M. Perkins, E. M. Grieveson, K. Theuwissen, D. W. McComb, P. D. Nellist and V. Nicolosi, *Science* **2011**, *331*, 568-571.

21 E. Benavente, M. A. Santa Ana, F. Mendizábal and G. González, *Coord. Chem. Rev.* **2002**, *224*, 87-109.

22 Z. Zeng, Z. Yin, X. Huang, H. Li, Q. He, G. Lu, F. Boey and H. Zhang, *Angew. Chem. Int. Ed.* **2011**, *50*, 11093-11097.

23 K. S. Novoselov, A. K. Geim, S. V. Morozov, D. Jiang, Y. Zhang, S. V. Dubonos, I. V. Grigorieva and A. A. Firsov, *Science* **2004**, *306*, 666-669.

24 Z. Guo, F. Sun and W. Yuan, *Cryst. Growth Des.* **2017**, *17*, 2238-2253.

25 M. Chhowalla, H. S. Shin, G. Eda, L.-J. Li, K. P. Loh and H. Zhang, *Nat. Chem.* **2013**, *5*, 263-275.

26 H. Wang, H. Yuan, S. Sae Hong, Y. Li and Y. Cui, *Chem. Soc. Rev.* **2015**, *44*, 2664-2680.

27 E. Gourmelon, O. Lignier, H. Hadouda, G. Couturier, J. C. Bernède, J. Tedd, J. Pouzet and J. Salardenne, *Sol. Energy Mater. Sol. Cells* **1997**, *46*, 115-121.

28 W. Ho, J. C. Yu, J. Lin, J. Yu and P. Li, *Langmuir* **2004**, *20*, 5865-5869.

29 A. Splendiani, L. Sun, Y. Zhang, T. Li, J. Kim, C.-Y. Chim, G. Galli and F. Wang, *Nano Lett.* **2010**, *10*, 1271-1275.

30 H. Wang, Z. Lu, S. Xu, D. Kong, J. J. Cha, G. Zheng, P.-C. Hsu, K. Yan, D. Bradshaw, F. B. Prinz and Y. Cui, *PNAS USA* **2013**, *110*, 19701-19706.

31 M. A. Lukowski, A. S. Daniel, F. Meng, A. Forticaux, L. Li and S. Jin, *J. Am. Chem. Soc.* **2013**, *135*, 10274-10277.

32 L. Britnell, R. V. Gorbachev, R. Jalil, B. D. Belle, F. Schedin, A. Mishchenko, T. Georgiou, M. I. Katsnelson, L. Eaves, S. V. Morozov, N. M. R. Peres, J. Leist, A. K. Geim, K. S. Novoselov and L. A. Ponomarenko, *Science* **2012**, *335*, 947-950.

33 W. Schuster, H. Mikler and K. L. Komarek, *Monatsh. Chem.* **1979**, *110*, 1153-1170.

34 P. Walder and A. D. Pelton, *JPED* **2005**, *26*, 23-38.

35 H. Okamoto and L. E. Tanner, *Bull. Alloy Phase Diagr.* **1990**, *11*, 371-376.

36 F.-C. Hsu, J.-Y. Luo, K.-W. Yeh, T.-K. Chen, T.-W. Huang, P. M. Wu, Y.-C. Lee, Y.-L. Huang, Y.-Y. Chu, D.-C. Yan and M.-K. Wu, *PNAS USA* **2008**, *105*, 14262-14264.

37 D. Johrendt, *J. Mater. Chem.* **2011**, *21*, 13726-13736.

38 A. E. Böhmer and A. Kreisel, *J. Phys.: Condens. Matter* **2018**, *30*, 023001.

39 J. Paglione and R. L. Greene, *Nat. Phys.* **2010**, *6*, 645-658.

40 S. Margadonna, Y. Takabayashi, M. T. McDonald, K. Kasperkiewicz, Y. Mizuguchi, Y. Takano, A. N. Fitch, E. Suard and K. Prassides, *Chem. Commun.* **2008**, 5607-5609.

41 T. M. McQueen, A. J. Williams, P. W. Stephens, J. Tao, Y. Zhu, V. Ksenofontov, F. Casper, C. Felser and R. J. Cava, *Phys. Rev. Lett.* **2009**, *103*, 057002.

42 M. A. Tanatar, A. E. Böhmer, E. I. Timmons, M. Schütt, G. Drachuck, V. Taufour, K. Kothapalli, A. Kreyssig, S. L. Bud'ko, P. C. Canfield, R. M. Fernandes and R. Prozorov, *Phys. Rev. Lett.* **2016**, *117*, 127001.

43 S. H. Baek, D. V. Efremov, J. M. Ok, J. S. Kim, J. van den Brink and B. Büchner, *Nat. Mater.* **2014**, *14*, 210-214.

44 J. Guo, S. Jin, G. Wang, S. Wang, K. Zhu, T. Zhou, M. He and X. Chen, *Phys. Rev. B: Condens. Matter* **2010**, *82*, 180520.

45 M.-H. Fang, H.-D. Wang, C.-H. Dong, Z.-J. Li, C.-M. Feng, J. Chen and H. Q. Yuan, *EPL* **2011**, *94*, 27009.

46 A. Krzton-Maziopa, Z. Shermadini, E. Pomjakushina, V. Pomjakushin, M. Bendele, A. Amato, R. Khasanov, H. Luetkens and K. Conder, *J. Phys.: Condens. Matter* **2011**, *23*, 052203.

47 A. F. Wang, J. J. Ying, Y. J. Yan, R. H. Liu, X. G. Luo, Z. Y. Li, X. F. Wang, M. Zhang, G. J. Ye, P. Cheng, Z. J. Xiang and X. H. Chen, *Phys. Rev. B: Condens. Matter* **2011**, *83*, 060512.

48 M. Burrard-Lucas, D. G. Free, S. J. Sedlmaier, J. D. Wright, S. J. Cassidy, Y. Hara, A. J. Corkett, T. Lancaster, P. J. Baker, S. J. Blundell and S. J. Clarke, *Nat. Mater.* **2012**, *12*, 15-19.

49 T. Ying, X. Chen, G. Wang, S. Jin, X. Lai, T. Zhou, H. Zhang, S. Shen and W. Wang, *J. Am. Chem. Soc.* **2013**, *135*, 2951-2954.

50 L. Zheng, M. Izumi, Y. Sakai, R. Eguchi, H. Goto, Y. Takabayashi, T. Kambe, T. Onji, S. Araki, T. C. Kobayashi, J. Kim, A. Fujiwara and Y. Kubozono, *Phys. Rev. B: Condens. Matter* **2013**, *88*, 094521.

51 K. V. Yusenko, J. Sottmann, H. Emerich, W. A. Crichton, L. Malavasi and S. Margadonna, *Chem. Commun.* **2015**, *51*, 7112-7115.

52 T. Noji, T. Hatakeda, S. Hosono, T. Kawamata, M. Kato and Y. Koike, *Physica C* **2014**, *504*, 8-11.

53 T. Hatakeda, T. Noji, T. Kawamata, M. Kato and Y. Koike, *J. Phys. Soc. Jpn.* **2013**, *82*, 123705.

54 T. Hatakeda, T. Noji, S. Hosono, T. Kawamata, M. Kato and Y. Koike, *JPCS* **2014**, *568*, 022032.

55 S. Hosono, T. Noji, T. Hatakeda, T. Kawamata, M. Kato and Y. Koike, *J. Phys. Soc. Jpn.* **2014**, *83*, 113704.

56 S. Hosono, T. Noji, T. Hatakeda, T. Kawamata, M. Kato and Y. Koike, *J. Phys. Soc. Jpn.* **2015**, *85*, 013702.

57 S. Jin, X. Fan, X. Wu, R. Sun, H. Wu, Q. Huang, C. Shi, X. Xi, Z. Li and X. Chen, *Chem. Commun.* **2017**, *53*, 9729-9732.

58 F. Hayashi, H. Lei, J. Guo and H. Hosono, *Inorg. Chem.* **2015**, *54*, 3346-3351.

59 U. Pachmayr, F. Nitsche, H. Luetkens, S. Kamusella, F. Brückner, R. Sarkar, H.-H. Klauss and D. Johrendt, *Angew. Chem. Int. Ed.* **2015**, *54*, 293-297.

60 X. F. Lu, N. Z. Wang, H. Wu, Y. P. Wu, D. Zhao, X. Z. Zeng, X. G. Luo, T. Wu, W. Bao, G. H. Zhang, F. Q. Huang, Q. Z. Huang and X. H. Chen, *Nat. Mater.* **2014**, *14*, 325-329.

61 Y. Mizuguchi, F. Tomioka, S. Tsuda, T. Yamaguchi and Y. Takano, *Appl. Phys. Lett.* **2008**, *93*, 152505.

62 S. Margadonna, Y. Takabayashi, Y. Ohishi, Y. Mizuguchi, Y. Takano, T. Kagayama, T. Nakagawa, M. Takata and K. Prassides, *Phys. Rev. B: Condens. Matter* **2009**, *80*, 064506.

63 Q.-Y. Wang, Z. Li, W.-H. Zhang, Z.-C. Zhang, J.-S. Zhang, W. Li, H. Ding, Y.-B. Ou, P. Deng, K. Chang, J. Wen, C.-L. Song, K. He, J.-F. Jia, S.-H. Ji, Y.-Y. Wang, L.-L. Wang, X. Chen, X.-C. Ma and Q.-K. Xue, *Chin. Phys. Lett.* **2012**, *29*, 037402.

64 J.-F. Ge, Z.-L. Liu, C. Liu, C.-L. Gao, D. Qian, Q.-K. Xue, Y. Liu and J.-F. Jia, *Nat. Mater.* **2014**, *14*, 285-289.

65 I. I. Mazin, *Nat. Mater.* **2015**, *14*, 755-756.

66 Y. Miyata, K. Nakayama, K. Sugawara, T. Sato and T. Takahashi, *Nat. Mater.* **2015**, *14*, 775-779.

67 R. Gusmão, Z. Sofer and M. Pumera, *Angew. Chem. Int. Ed.* **2019**, *58*, 9326-9337.

68 N. D. Mermin and H. Wagner, *Phys. Rev. Lett.* **1966**, *17*, 1133-1136.

69 J.-U. Lee, S. Lee, J. H. Ryoo, S. Kang, T. Y. Kim, P. Kim, C.-H. Park, J.-G. Park and H. Cheong, *Nano Lett.* **2016**, *16*, 7433-7438.

70 X. Wang, K. Du, Y. Y. Fredrik Liu, P. Hu, J. Zhang, Q. Zhang, M. H. S. Owen, X. Lu, C. K. Gan, P. Sengupta, C. Kloc and Q. Xiong, *2D Mater.* **2016**, *3*, 031009.

71 M.-W. Lin, H. L. Zhuang, J. Yan, T. Z. Ward, A. A. Puretzky, C. M. Rouleau, Z. Gai, L. Liang, V. Meunier, B. G. Sumpter, P. Ganesh, P. R. C. Kent, D. B. Geohegan, D. G. Mandrus and K. Xiao, *J. Mater. Chem. C* **2016**, *4*, 315-322.

72 C. Gong, L. Li, Z. Li, H. Ji, A. Stern, Y. Xia, T. Cao, W. Bao, C. Wang, Y. Wang, Z. Q. Qiu, R. J. Cava, S. G. Louie, J. Xia and X. Zhang, *Nature* **2017**, *546*, 265-269.

73 H.-J. Deiseroth, K. Aleksandrov, C. Reiner, L. Kienle and R. K. Kremer, *Eur. J. Inorg. Chem.* **2006**, *2006*, 1561-1567.

74 V. Y. Verchenko, A. A. Tsirlin, A. V. Sobolev, I. A. Presniakov and A. V. Shevelkov, *Inorg. Chem.* **2015**, *54*, 8598-8607.

75 A. F. May, S. Calder, C. Cantoni, H. Cao and M. A. McGuire, *Phys. Rev. B: Condens. Matter* **2016**, *93*, 014411.

76 B. Chen, J. Yang, H. Wang, M. Imai, H. Ohta, C. Michioka, K. Yoshimura and M. Fang, *J. Phys. Soc. Jpn.* **2013**, *82*, 124711.

77 J. Stahl, V. Pomjakushin and D. Johrendt, *Z. Naturforsch., B: Chem. Sci.* **2016**, *71*, 273-276.

78 C. Tan, J. Lee, S.-G. Jung, T. Park, S. Albarakati, J. Partridge, M. R. Field, D. G. McCulloch, L. Wang and C. Lee, *Nat. Commun.* **2018**, *9*, 1554.

79 Z. Fei, B. Huang, P. Malinowski, W. Wang, T. Song, J. Sanchez, W. Yao, D. Xiao, X. Zhu, A. F. May, W. Wu, D. H. Cobden, J.-H. Chu and X. Xu, *Nat. Mater.* **2018**, *17*, 778-782.

80 Y. Deng, Y. Yu, Y. Song, J. Zhang, N. Z. Wang, Z. Sun, Y. Yi, Y. Z. Wu, S. Wu, J. Zhu, J. Wang, X. H. Chen and Y. Zhang, *Nature* **2018**, *563*, 94-99.

81 G. Drachuck, Z. Salman, M. W. Masters, V. Taufour, T. N. Lamichhane, Q. Lin, W. E. Straszheim, S. L. Bud'ko and P. C.Canfield, *Phys. Rev. B: Condens. Matter* **2018**, *98*, 144434.

82 D. Yuan, S. Jin, N. Liu, S. Shen, Z. Lin, K. Li and X. Chen, *Mater. Res. Express* **2017**, *4*, 036103.

83 D. Weber, A. H. Trout, D. W. McComb and J. E. Goldberger, *Nano Lett.* **2019**, *19*, 5031-5035.

84 G. Demazeau, *J. Mater. Sci.* **2008**, *43*, 2104-2114.

85 C. Pak, S. Kamali, J. Pham, K. Lee, J. T. Greenfield and K. Kovnir, *J. Am. Chem. Soc.* **2013**, *135*, 19111-19114.

86 U. Pachmayr, N. Fehn and D. Johrendt, *Chem. Commun.* **2016**, *52*, 194-197.

87 J. T. Greenfield, S. Kamali, K. Lee and K. Kovnir, *Chem. Mater.* **2015**, *27*, 588-596.

2 Solvothermal synthesis of β-FeSe-related structures

2.1 Systematic dimensional reduction of the layered β-FeSe structure by solvothermal synthesis

Juliane Stahl, Evgeniya Shlaen, Helena Singer and Dirk Johrendt

Published in: *Dalton Transactions* **2018**, *47*, 3264-3271.[a]

Reproduced from Reference with permission from the Royal Society of Chemistry.

Abstract

Dimensional reduction of superconducting anti PbO-type iron selenide has been achieved by terminating the tetragonal square layers of $FeSe_{4/4}$ tetrahedra by ethylenediamine [*en*] ligands. We obtained three new structures in the Fe-Se-*en* system. $Fe_3Se_4(en)_3$ contains $FeSe_2$ single chains bridged *via* $Fe(en)_3$ complexes. $Fe_{10}Se_{12}(en)_7$ has Fe_2Se_3 double strands separated by $Fe(en)_3$ complexes and free *en* molecules. $Fe_{0.85}Se(en)_{0.3}$ conserves the tetragonal layers of bulk FeSe which are now widely separated by *en* molecules. Through systematic dilution of the solvent we were able to introduce an additional parameter in solvothermal synthesis and thus have control over the connectivity of the tetrahedra. Additionally, a

[a] Supplementary Information in appendix A.1

phase diagram of the Fe-Se-*en* system is generated by variation of the reaction temperature. The magnetic properties of the FeSe derivatives range from superconductivity and antiferromagnetism to paramagnetism.

Introduction

The concept of dimensional reduction of solid state materials has recently attracted increased attention and new strategies have been developed to change the framework connectivity of inorganic lattices.[1] The properties of the less tightly connected derivates, *e.g.* optical, electronic or magnetic behavior, differ from those of the parent structures, while the metal coordination geometry mode is still preserved.[1-3] One approach to reduce the dimensionality is to terminate the framework along specific axes by organic ligands.[1,2,4,5] These ligands often have the advantage of only weak coordination to the reduced fragments. As a result the properties of single building blocks of the inorganic lattice can be investigated.[4] Furthermore, organic ligands show a rich structural diversity, so tuning of the connectivity and properties is possible by changing the ligand structure or binding type.[1,5] In addition, there is a wide range of parameters, including starting materials, ligand-to-metal ratio, reaction type and reaction conditions, which affect the connectivity of the stabilized fragments.[1,2]

Ligands containing amino groups are versatile to terminate inorganic frameworks due to their behavior as uncharged Lewis bases. For example, the dimensional reduction of II–VI binary chalcogenide compounds is realized in compounds with a general formula $M_nQ_nL_{0.5}$ [M = Zn, Cd; Q = S, Se; L = monoamine], where the 3D zinc-blende or wurtzite bulk structure (MQ) is confined to single atomic layers [n = 1] or double layers [n = 2].[6] Further reduction of a layered metal chalcogenide structure

down to one-dimensional fragments has been achieved in the Ti-S-*en* system [*en* = ethylenediamine].[2] The TiS_2 structure can be either intercalated by *en* to form 2D hybrid frameworks, or terminated by the *en* ligands to form single chains.[7,8] For thiogallate based structures even the reduction of a 3D network to a quasi-1D compound has been accomplished.[9] GaS_2 chains in $Ga_2S_4Mn(en)_2$ are connected to a 3D network *via* $Mn(en)_2$ complexes. GaS_4 and GaS_3N tetrahedra in $Ga_4S_7(en)_2(enH_2)$ form a layered structure and in $Ga_2S_4Mn(en)_3$ the GaS_2 chains are separated by $Mn(en)_3$ complexes. Comparable dimensional reduction of the quasi-2D PbO-type structure of the superconductor FeSe has been realized in $Fe_3Se_4(en)_2$, where $FeSe_2$ chains are connected *via* $Fe(en)_2$ complexes.[4] The chains are arranged parallel and are composed of FeSe tetrahedra sharing opposing edges. Superconductivity does not persist in $Fe_3Se_4(en)_2$, but antiferromagnetism can be found within the chains.

By changing the ligand-to-metal ratio in solvothermal synthesis we demonstrate, how the condensation of the tetrahedra in the Fe-Se-*en* system can be tuned. The dilution of ethylenediamine with *glycerol* leads to reduction of the amine available for the reaction. On this account we were able to synthesize two new compounds. $Fe_{10}Se_{12}(en)_7$ and $Fe_{0.85}Se(en)_{0.3}$ show higher connectivity of the FeSe tetrahedra and dimensionality changes from Fe_2Se_3 chains to isolated FeSe layers, respectively. The degree of condensation increases with the amount of *glycerol*. Thus we have chemical control over the polyhedral connectivity in the Fe-Se-*en* system. Additionally, we were able to produce a phase diagram of the system by varying the reaction temperature. In this context, we detected the new compound $Fe_3Se_4(en)_3$ with similar tetrahedra connectivity as in $Fe_3Se_4(en)_2$ but different terminating ligands, so the 3D character is attenuated.

Experimental

Solvothermal syntheses were carried out in Teflon-lined steel autoclaves [50 mL]. Fe powder [Chempur, 99.9%] and Se powder [Chempur, 99.999%] were weighted in 1 : 1 molar ratio for a total amount of 50 mg and 100 mg of NH_4Cl [Kraft, purissimum] were added as a mineralizer. Ethane-1,2-diamine [*en*, Merck, ≥99%] and propane-1,2,3-triol [*glycerol*, Grüssing, 99%] were added in corresponding ratio to a filling fraction of the autoclave of 70% [35 mL]. The autoclaves were heated to 160-220 °C for 5 days. For $Fe_3Se_4(en)_2$, $Fe_3Se_4(en)_3$ and $Fe_{10}Se_{12}(en)_7$ black needle shaped crystals were obtained as a product while $Fe_{0.85}Se(en)_{0.3}$ resulted in plate like metallic crystals. The products were washed with water, ethanol and acetone and treated by ultrasound and centrifugation at each step. Samples were dried under vacuum at room temperature. All products are stable at dry air for several days.

X-ray diffraction patterns of the powdery samples were collected using either a Stoe Stadi P diffractometer [Mo-$K_{\alpha1}$ radiation; Ge-111 monochromator] with capillary sample holder or a Huber G670 diffractometer [Cu-$K_{\alpha1}$ radiation; Ge-111 monochromator] with flat specimen holder. The former was also used for high temperature PXRD measurements between 293 and 1073 K. Low temperature measurements between 10 and 290 K were done on a Huber G670 diffractometer [Co-$K_{\alpha1}$ radiation; Ge-111 monochromator] with Low Temperature Device 670.4 and closed cycle He cryostat. Rietveld refinements were done using TOPAS package.[10] Single crystal analyses were performed on a Bruker D8-Quest diffractometer [Mo-K_α radiation; graphite monochromator] and structure refinements were done using Jana2006 program package.[11] The composition of the compounds regarding the Fe : Se ratio were verified by energy-dispersive spectroscopy measurements on a Zeiss Evo-Ma10 micro-

scope with Bruker X-Flash 410-M detector. For analysis of the C : N : H ratio CHNS elemental analysis was used. Magnetic measurements were carried out on a Quantum Design SQUID Magnetometer MPMS XL-5.

Results and discussion

Crystal structures. $Fe_3Se_4(en)_3$ has a triclinic structure with space group $P\bar{1}$ and the lattice parameters a = 9.104(4) Å, b = 10.398(4) Å, c = 11.675(5) Å, α = 109.88(1)°, β = 96.37(2)° and γ = 114.09(1)°. The structure was solved from single crystal X-ray data [Mo-K_α radiation]. Hydrogen positions were not determined from the data, but added with C-H distances of 1.09 Å and N-H distances of 1.04 Å.[12] The positions were then refined with constrained bond lengths, angles and ADPs [isotropic, extension factor 1.2].

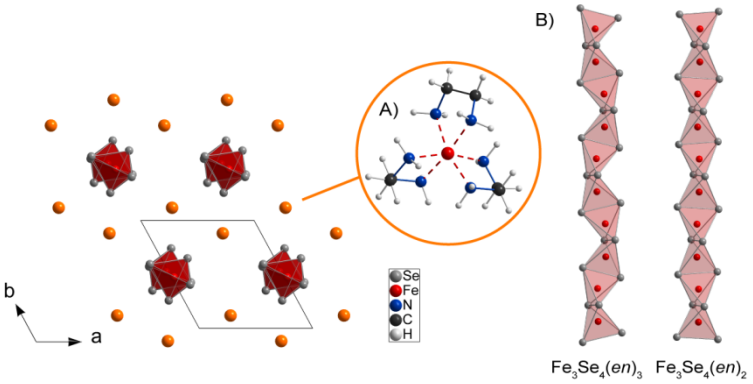

Figure 2-1 Schematic view of the $Fe_3Se_4(en)_3$ structure along [001]: orange spheres represent $Fe(en)_3$ complexes (A); (B) $FeSe_2$ single chain of $Fe_3Se_4(en)_3$ with tilted tetrahedra compared to single chain of $Fe_3Se_4(en)_2$.

The structure of $Fe_3Se_4(en)_3$ [Figure 2-1] is similar to the structure of the literature known compound $Fe_3Se_4(en)_2$.[4] Both contain parallel $FeSe_2$

chains consisting of FeSe tetrahedra sharing opposing edges. In $Fe_3Se_4(en)_3$ the chains are slightly distorted because the tetrahedra are alternately tilted towards each other [Figure 2-1 B]. The distortion of the tetrahedra itself with Fe-Se distances of 2.339(1)-2.423(1) Å and angles ∢Se-Fe-Se of 100.0(1)-118.1(1)° is also stronger than in $Fe_3Se_4(en)_2$ [*d*(FeSe) = 2.353-2.397 Å, ∢Se-Fe-Se = 103.8-117.1°].[4] The $FeSe_2$ chains in the new structure are not connected *via* $Fe(en)_2$ complexes as in $Fe_3Se_4(en)_2$, but $Fe(en)_3$ complexes are located between the chains [Figure 2-1 A]. The central Fe atom binds to six nitrogen atoms of the three *en* molecules in a distorted octahedral coordination with average Fe-N distance of 2.216(20) Å. While in $Fe_3Se_4(en)_2$ Fe-Se bonds connect the chains, in $Fe_3Se_4(en)_3$ they are only linked *via* hydrogen bonds. The shortest Se···H-N distances of the H atoms of the coordinating *en* and the chains are 2.473(1)-2.944(1) Å. In comparison, the average Se-H distance in $Fe_3Se_4(en)_2$ is 2.56 Å. So the chains in the new structure are less tightly connected due to missing Fe-Se bonds and weaker hydrogen bonds. A similar situation is realized in the compound $Fe_3Se_4(dien)_2$ with the tridentate ligand diethylenetriamine [*dien*].[5] Here also slightly tilted $FeSe_2$ chains are separated by $Fe(dien)_2$ complexes which are only connected to the chains by hydrogen bonds [*d*(Se···H-N) = 2.62-3.00 Å]. Other structures with comparable single chains are found in the system of the thiogallates solvothermally reacted with *en*.[9] $Ga_2S_4Mn(en)_2$ shows similar structural motifs as $Fe_3Se_4(en)_2$ with GaS_2 chains connected to a 3D network by $Mn(en)_2$ complexes, while in $Ga_2S_4Mn(en)_3$ the GaS_2 chains are isolated by $Mn(en)_3$ complexes like in $Fe_3Se_4(en)_3$.

The crystal structure of $Fe_{10}Se_{12}(en)_7$ was determined by single crystal X-ray diffraction [Mo-K_α radiation] at 120 K due to the large movement of the *en* molecules in the structure. Positions of the H atoms of the *en* molecules were not resolved from the data but treated as described

above. $Fe_{10}Se_{12}(en)_7$ exhibits an orthorhombic cell with monoclinic space group $P2_1/n$ and the lattice parameters a = 9.323(2) Å, b = 12.273(2) Å and c = 20.821(4) Å [a = 9.416(5) Å, b = 12.345(7) Å, c = 20.993(11) Å at room temperature].

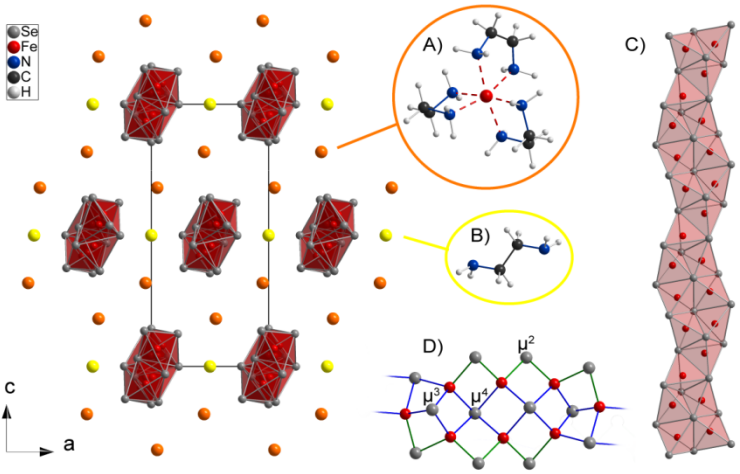

Figure 2-2 Schematic view of the $Fe_{10}Se_{12}(en)_7$ structure along [010]: orange spheres represent $Fe(en)_3$ complexes (A), yellow spheres represent *en* molecules (B); (C) Fe_2Se_3 double chain; (D) detail of the Fe_2Se_3 chain with longer [blue] and shorter [green] Fe-Se distances.

The structure shows three different structural motifs [Figure 2-2]. Slightly distorted Fe_2Se_3 double chains composed of distorted FeSe tetrahedra sharing three edges run along the b axis [Figure 2-2 C]. The linkage of the tetrahedra results in different bridging Se atoms [Figure 2-2 D]. Fe-Se distances of the μ^3 and μ^4 Se atoms in the backbone of the chains are slightly larger [2.380(1)-2.473(1) Å] than the Fe-Se distances of the μ^2 Se atoms at the edges [2.322(1)-2.380(1) Å]. These differing bond lengths and the angles ∢Se-Fe-Se with 100.9(1)-123.5(1)° show the strong distortion of the tetrahedra compared to β-FeSe

[d(FeSe) = 2.393 Å, ∢Se-Fe-Se = 104.0-112.3°] and the structures containing single $FeSe_2$ chains [see above].[13] Fe_2Se_3 double chains are known in the literature for example in the structure of $BaFe_2Se_3$, where the chains are separated by Ba atoms.[14] Although all tetrahedra are connected *via* three edges, as in $Fe_{10}Se_{12}(en)_7$, the arrangement results only in μ^2 and μ^4 Se atoms due to the more regular structure of the chains. The tetrahedra show Fe-Se distances of 2.396-2.444 Å and angles ∢Se-Fe-Se of 107.8-112.6° and are therefore also less distorted.[14] In $Fe_{10}Se_{12}(en)_7$ $Fe(en)_3$ complexes with average Fe-N distance of 2.219(13) Å are located between the double chains [Figure 2-2 A]. These are similar to those found in $Fe_3Se_4(en)_3$. The chains are also only linked by hydrogen bonds with shortest Se···H-N distances of 2.520(1)-2.712(1) Å of the H atoms of the coordinating *en* and the μ^2 Se atoms. In addition to the $Fe(en)_3$ complexes non-coordinating *en* molecules are found between the chains [Figure 2-2 B]. These molecules are held in space by Se···H-N and Se···H-C bonds to Se atoms of the double chains [2.799(1)-3.182(1) Å] and are located between the chains along the *a* axis. Due to these large Se-H distances the non-coordinating *en* molecules are weakly bound in the framework and show large thermal displacements at higher temperatures. The *en* molecules of the $Fe(en)_3$ complexes show anisotropic ADPs as well [see Table A-2], even at 120 K. Anisotropy of all ellipsoids of the N and C atoms show the facilitated movement around the central Fe atom of the $Fe(en)_3$ complex, while the Fe-C and Fe-N distances are affected little by the thermal movement.

$Fe_{0.85}Se(en)_{0.3}$ exhibits a monoclinic structure with space group $C2/c$ and lattice parameters a = 3.904(1) Å, b = 21.527(2) Å, c = 3.859(1) Å and β = 91.35(2)°. Single crystal X-ray diffraction [Mo-K_α radiation] yielded only low-resolution data [1.1 Å] due to the poor crystal quality. Additional twinning finally impeded a satisfactory refinement of the parame-

ters, especially the site occupation factors. Only the C-centered cell and the positions of the Fe and Se atoms could be determined. Therefore the structure was subsequently refined from X-ray powder diffraction data. The atoms of the *en* molecules are not resolved, so the molecules were treated as rigid bodies with fixed geometry according to the literature.[12] The scattering contributions of the *en* molecules are very low, but even this very small additional scattering improves the Rietveld fit. Nevertheless, we point out that the *en* positions given here should be considered as a model consistent with but not strictly determined from powder diffraction data.

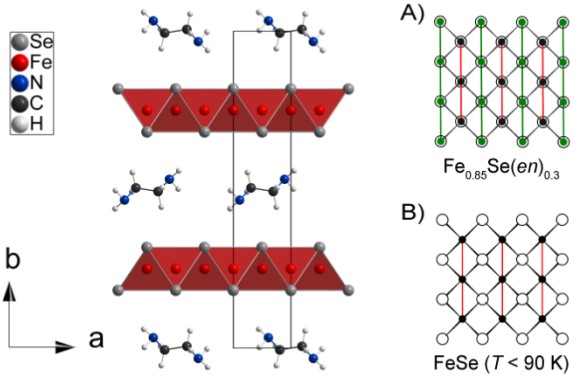

Figure 2-3 $Fe_{0.85}Se(en)_{0.3}$ structure along [001] [*en* partly omitted]. A), B) Projections of $Fe_{0.85}Se(en)_{0.3}$ and FeSe layers with shorter Fe-Fe distances marked by red and green lines.

The structure consists of FeSe tetrahedral layers intercalated by *en* [Figure 2-3]. Refinement of the site occupation indicates an iron deficiency of about 15-25%, but the strong correlations of the occupation with the displacement parameter at the iron site allowed no reliable determination from diffraction data. The site occupation factors for Rietveld refinement were at last taken from chemical analysis [see Table A-8

and Table A-9] with a resulting stoichiometry of $Fe_{0.85}Se(en)_{0.3}$. The distance of the layers in the structure of $Fe_{0.85}Se(en)_{0.3}$ amounts to 10.78 Å and agrees with those of the superconducting compounds $A_x(en)_yFe_{2-z}Se2$ [A = Li, Na] [10.37-10.95 Å] which contain additional alkali ions.[15-17] The stacking of the layers in $Fe_{0.85}Se(en)_{0.3}$ however differs from those in the alkaline-containing compounds as well as from the binary β-FeSe. In the latter iron and selenium atoms are stacked one above the other [Figure 2-3 B] while every second layer is shifted in the new compound, where iron and selenium are stacked alternatively [Figure 2-3 A]. Similar stacking of layers is known from $LaMnSi_2$-type structures.[18] The FeSe tetrahedra are weakly distorted with Fe-Se distances of 2.405 Å and 2.426 Å and angles ∢Se-Fe-Se between 106.7° and 111.7°. The Fe-Fe distances in the distorted square Fe net are 2.712 Å and 2.776 Å and reveal the typical stripe-type motif of the shorter Fe-Fe bonds shown as red and green lines in Figure 2-3 A and B. Thus the structures of the respective iron selenide layers are very similar in $Fe_{0.85}Se(en)_{0.3}$ and orthorhombic FeSe [T < 90 K].

Rietveld refinement of powder patterns of $Fe_3Se_4(en)_3$, $Fe_{10}Se_{12}(en)_7$ and $Fe_{0.85}Se(en)_{0.3}$ yield good results [Figure 2-4], so the structure solutions are considered accurate. For $Fe_3Se_4(en)_3$ Fe is detected as a side phase [<1 wt%] and additional reflexions of a so far unknown phase are visible in the diffractogram [d = 10.7 Å, 10.2 Å, 8.6 Å, 8.4 Å; see chapter 2.1.1]. The new structures are shown in Figure 2-5 together with β-FeSe and $Fe_3Se_4(en)_2$.[4,19] In $Fe_{0.85}Se(en)_{0.3}$ the FeSe layers are isolated by neutral spacer layers with almost doubled layer distance [10.78 Å] compared to PbO-type FeSe [5.52 Å].[13] The degree of condensation of the FeSe tetrahedra is decreased from four to three shared edges in $Fe_{10}Se_{12}(en)_7$ and two edges in $Fe_3Se_4(en)_2$ and $Fe_3Se_4(en)_3$. So stepwise dimensional reduction of the β-FeSe structure is realized in the Fe-Se-*en* system with iso-

lated layers in $Fe_{0.85}Se(en)_{0.3}$, double chains in $Fe_{10}Se_{12}(en)_7$ and single chains in $Fe_3Se_4(en)_2$ and $Fe_3Se_4(en)_3$. While the single chains in $Fe_3Se_4(en)_2$ are connected *via* Fe-Se bonds the chains are almost not connected in $Fe_3Se_4(en)_3$.

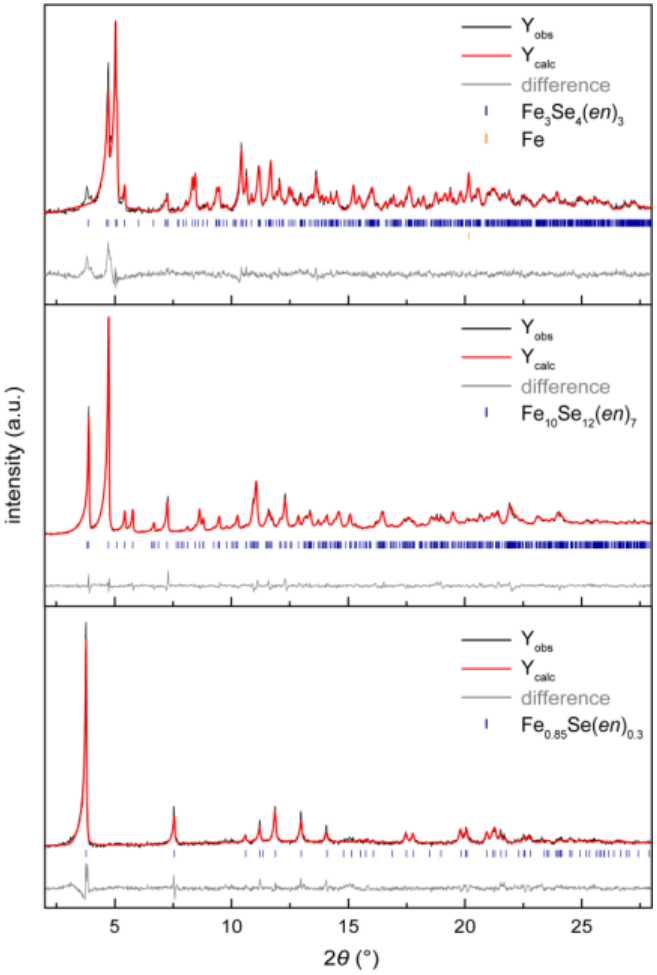

Figure 2-4 Rietveld refinement of powder diffraction patterns [Mo-$K_{\alpha 1}$] of $Fe_3Se_4(en)_3$ [top], $Fe_{10}Se_{12}(en)_7$ [middle] and $Fe_{0.85}Se(en)_{0.3}$ [bottom].

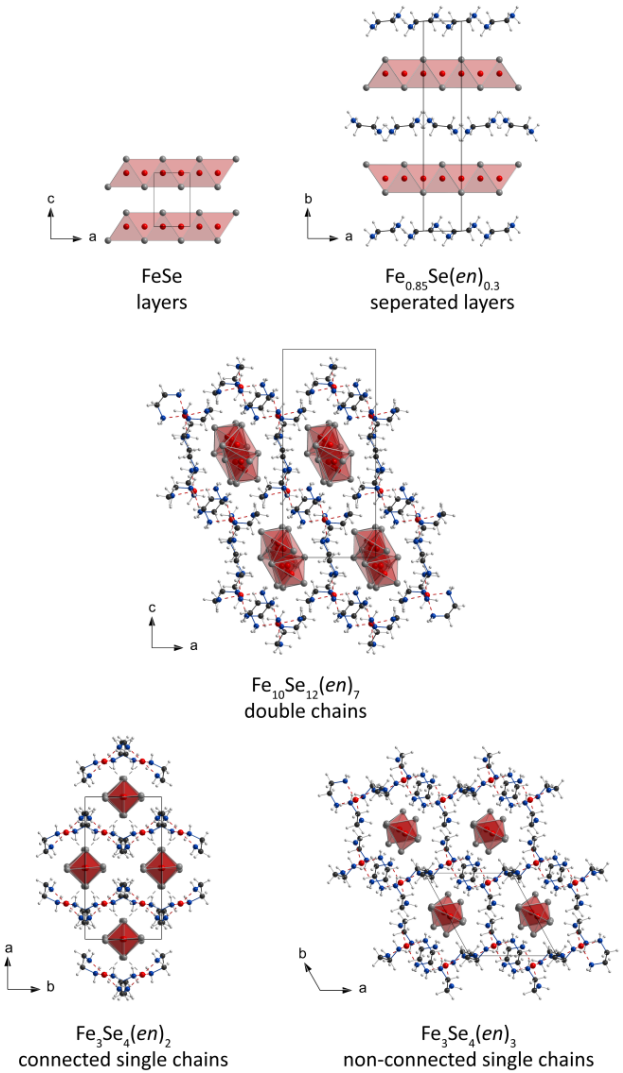

Figure 2-5 Crystal structures of β-FeSe, $Fe_{0.85}Se(en)_{0.3}$, $Fe_{10}Se_{12}(en)_7$, $Fe_3Se_4(en)_2$ and $Fe_3Se_4(en)_3$.

Phase diagram. The new compounds in the Fe-Se-*en* system were obtained by changing the ligand-to-metal ratio in solvothermal synthesis. This was achieved by diluting the solvent *en* by *glycerol* while the amount of Fe and Se was maintained. We investigated the stability ranges of the phases regarding the degree of dilution and the synthesis temperature. Figure 2-6 shows the resulting phase space diagram between 160 °C and 220 °C and 0% and 50% *glycerol* content. The composition of the products was calculated from powder diffraction data by Rietveld refinement and phase ranges were estimated from the main phases of the obtained products [see Table A-10]. Higher ratios of *en* : *glycerol* than 50 : 50 yielded mixed phases containing FeSe, $FeSe_2$ and Fe_3Se_4 in various compositions. So if the ligand-to-metal ratio is too low no *en* is inserted into the structure. Below 170 °C and 30% glycerol just amorphous products containing traces of the educts were obtained. $Fe_3Se_4(en)_2$ is stable from 190 °C and between 0% and 10% of *glycerol*. Phase pure synthesis is possible for 0% *glycerol* between 200 °C and 220 °C. For lower temperatures and pure *en* $Fe_3Se_4(en)_3$ is found as main phase. Small amounts of iron and an unknown component [see chapter 2.1.1] are found at 170 °C as side phases. For dilution between 10% and 40% and temperatures between 180 °C and 210 °C phase pure $Fe_{10}Se_{12}(en)_7$ is synthesized. At higher degrees of dilution the intercalated structure $Fe_{0.85}Se(en)_{0.3}$ represents the main phase. At 200 °C and 50% of *glycerol* phase pure synthesis with good crystallinity is achieved.

Increasing crystallinity with synthesis temperature is found for all phases by analysis of the full width at half maximum [FWHM] of the corresponding main reflex of the powder patterns [Cu-$K_{\alpha 1}$ radiation]. For $Fe_3Se_4(en)_2$ the FWHM decreases from 0.163° at 190 °C to 0.130° at 220 °C at 0% *glycerol* [2θ = 12.54°]. For $Fe_3Se_4(en)_3$ at 0% *glycerol* FWHMs

of 0.182° at 170 °C and 0.156° at 180 °C are determined [2θ = 10.93°]. At 20% *glycerol* for $Fe_{10}Se_{12}(en)_7$ a decrease from 0.220° to 0.204° is found at 180 °C and 210 °C, respectively [2θ = 10.23°]. The largest effect of the temperature is observed for $Fe_{0.85}Se(en)_{0.3}$ with a FWHM of 0.320° at 160 °C and 0.211° at 220 °C at 50% dilution [2θ = 8.12°]. The phase diagram shows the dependence of the connectivity of the tetrahedra on the degree of dilution and therefore on the ligand-to-metal ratio. The degree of condensation of the FeSe tetrahedra is increased with the *glycerol* content. Thus by this additional parameter in solvothermal synthesis we have chemical control over the connectivity of the polyhedra in the Fe-Se-*en* system.

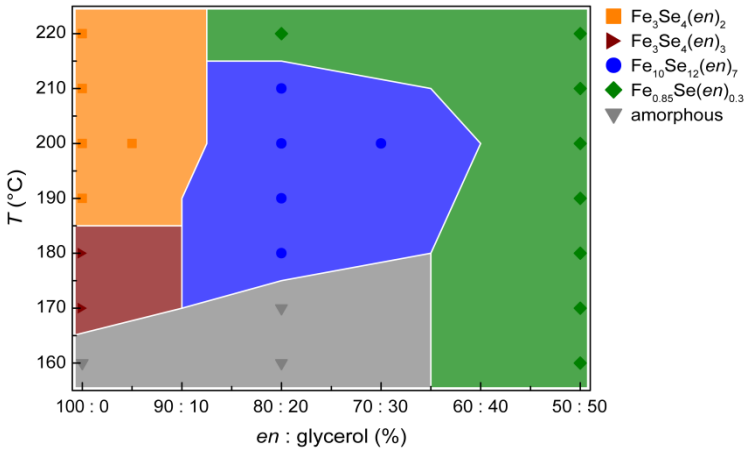

Figure 2-6 Synthetic phase space diagram of the Fe-Se-*en* system in dependence of the composition of the solvent and the temperature. Markings show main phases of the obtained products.

Thermal expansion. The dimensional reduction in the Fe-Se-*en* system can be illustrated by means of the thermal expansion of the lattice parameters. We measured temperature dependent powder diffraction pat-

terns [Co-$K_{\alpha 1}$ radiation] of $Fe_3Se_4(en)_3$, $Fe_3Se_4(en)_2$, $Fe_{10}Se_{12}(en)_7$ and $Fe_{0.85}Se(en)_{0.3}$ between 10 K and 290 K and determined the lattice parameters by Rietveld refinements. Figure 2-7 shows the relative lattice parameters in dependence of the temperature with a_0, b_0, and c_0 from refinement at 10 K, respectively. For $Fe_3Se_4(en)_3$ strong differences in the relative expansion are observed for the different directions. While *c* remains almost constant in the measured temperature range [$\Delta c < 0.1\%$], *a* and *b* axis show a significant increase with temperature [$\Delta a = 2.0\%$, $\Delta b = 0.5\%$]. That is expected since the single chains in the structure are arranged parallel to the *c* axis and strong Fe-Se bonds prevent the expansion in this direction. In *a* and *b* direction only weak hydrogen bonds connect the chains so expansion in these directions is facilitated. The larger increase in the *a* parameter compared to *b* may be due to the position of the $Fe(en)_3$ complexes in the structure, which are stacked alternately with the chains in *b* direction. So there are less hydrogen bonds of *en* molecules in *a* direction. For $Fe_3Se_4(en)_2$ all three lattice parameters exhibit almost the same low relative expansion [$\Delta a = 0.4\%$, $\Delta b = 0.8\%$, $\Delta c = 0.6\%$]. This is because in contrast to $Fe_3Se_4(en)_3$ the chains in this structure are connected *via* Fe-Se bonds to $Fe(en)_2$ complexes, so expansion is hindered in all three directions. For $Fe_{10}Se_{12}(en)_7$, the situation is similar to that for $Fe_3Se_4(en)_3$. While the *b* parameter is almost unchanged with temperature [$\Delta b = 0.2\%$] due to the double chains running along this direction, *a* and *c* show an increase [$\Delta a = 1.1\%$, $\Delta c = 0.7\%$]. The different expansion in these two directions may also be due to different hydrogen bonding. In *a* direction non-coordinating *en* molecules are located between the chains, while in *c* direction the $Fe(en)_3$ complexes are found. The complexes show shorter Se-H distances to the Fe_3Se_4 chains than the molecules [see above]. The smaller relative increase in the lattice parameters compared to $Fe_3Se_4(en)_3$ could also be an account of the

shorter hydrogen bonds of the complexes to the chains. In $Fe_3Se_4(en)_3$ the average Se···H-N distance is 2.70(20) Å compared to 2.64(7) Å in $Fe_{10}Se_{12}(en)_7$. In $Fe_{0.85}Se(en)_{0.3}$ the thermal expansion in the *ac* plane is prevented by the Fe-Se bonds in the FeSe layer [$\Delta a = 0.4\%$, $\Delta c = 0.1\%$]. Along the layer stacking in *b* direction the expansion is facilitated due to the weak hydrogen bonds between the *en* molecules and the FeSe layers [$\Delta b = 1.2\%$].

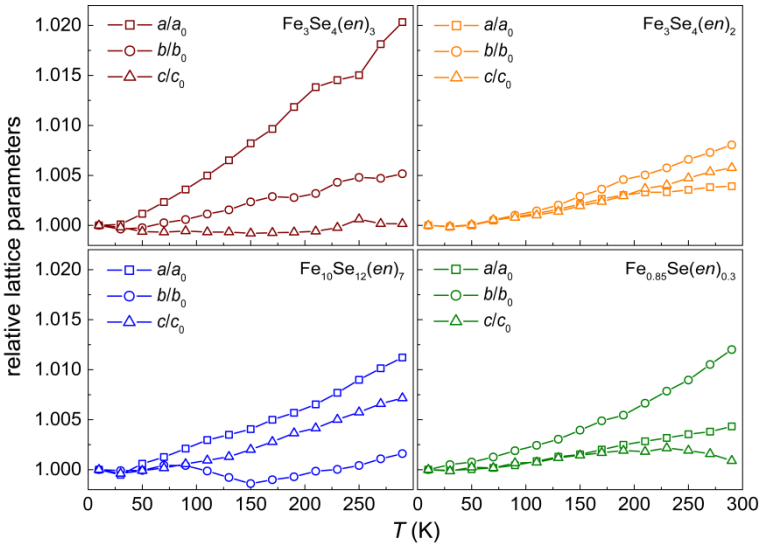

Figure 2-7 Relative lattice parameters between 10 K and 290 K for $Fe_3Se_4(en)_3$, $Fe_3Se_4(en)_2$, $Fe_{10}Se_{12}(en)_7$ and $Fe_{0.85}Se(en)_{0.3}$ from Rietveld refinement.

Overall, the thermal expansion measurements of the compounds reflect the dimensional reduction. While the layered structure of $Fe_{0.85}Se(en)_{0.3}$ exhibits facilitated expansion in one direction, the 1D structures of $Fe_3Se_4(en)_3$ and $Fe_{10}Se_{12}(en)_7$ with weakly connected chains show facilitated expansion in two directions. Although $Fe_3Se_4(en)_2$ shows 1D struc-

tural elements with the $FeSe_2$ single chains, the prevented thermal expansion in all directions reveals more a 3D network character of the compound. In addition to the thermal expansion we measured the decomposition of the compounds by high temperature powder diffraction between 30 °C and 300 °C. After a monoclinic to orthorhombic phase transition *en* is deintercalated from $Fe_{0.85}Se(en)_{0.3}$ above 200 °C and *β*-FeSe is formed [see chapter 2.1.2 for further details]. $Fe_3Se_4(en)_2$ and $Fe_{10}Se_{12}(en)_7$ decompose above 140 °C and 110 °C, respectively, to $FeSe_2$ and elemental Fe and Se.

Magnetic properties. $Fe_3Se_4(en)_2$ is reported to exhibit an antiferromagnetic transition below 150 K.[4] The interactions within the chains are stronger than between the chains, so a complete 3D ordering is not accomplished even at 10 K. *β*-FeSe is superconducting below 8 K.[19] Figure 2-8 shows the temperature dependence of the magnetic susceptibilities of $Fe_{10}Se_{12}(en)_7$, $Fe_3Se_4(en)_3$ and $Fe_{0.85}Se(en)_{0.3}$ between 1.8 K and 300 K at 1 T. $Fe_{10}Se_{12}(en)_7$ is paramagnetic above 10 K, while below a deviation from the linear behavior in the inverse susceptibility is observed. Modified Curie-Weiss fitting of the paramagnetic region gives $\chi_0 =$ 0.0058(2) cm^3 mol^{-1}, $\Theta =$ -1.7(4) K and $C =$ 8.48(5) cm^3 mol^{-1} K. This yields an effective paramagnetic moment μ_{eff} of 8.23(2) μ_B per formula unit. If all Fe atoms contribute to the magnetization, this would lead to much smaller moments per Fe atom than expected for Fe^{2+} [4.90 μ_B, S = 2] or Fe^{3+} [1.73 μ_B, S = 1/2 or 5.92 μ_B, S = 5/2]. Assuming that only the Fe atoms in $Fe(en)_3$ complexes contribute to the magnetization, a moment of $\mu_{eff}(Fe_{complex}) = 5.82(2)\ \mu_B$ is obtained, which is near to the value expected for high-spin Fe^{3+}. However, in the literature several compounds with $Fe(en)_3$ complexes are found, which mainly contain high spin Fe^{2+} or low spin Fe^{3+}.[20-24] Moreover, typical Fe-N distances for

high spin Fe^{3+} complexes are 2.0 Å, while the average distance of 2.219(13) Å in $Fe_{10}Se_{12}(en)_7$ indicates high spin Fe^{2+} ions (typical distance 2.2 Å).[25,26] Given the fact that we do not concretely know the contribution of the FeSe tetrahedral chains to the magnetic susceptibility, a Fe^{2+} high spin state for the *en*-coordinated Fe atoms in $Fe_{10}Se_{12}(en)_7$ is more likely. Therefore the formula $[Fe^{2+}{}_4Fe^{3+}{}_4Se^{2-}{}_{12}][Fe^{2+}(en)_3]_2(en)$ is assumed which leads to different oxidation states of the Fe atoms in the double chains. This may be a consequence of the different environment of the Fe atoms due to different bridging Se atoms and the strong displacement of the chains. Both Fe^{2+} and Fe^{3+} oxidation states are found in the literature for edge-sharing FeSe tetrahedra.[4,27] In $Fe_3Se_4(en)_2$ the tetrahedral single chains show Fe^{3+} while β-FeSe and $BaFe_2Se_3$ contain Fe^{2+}.[4,28,29] With AFe_2Se_3 [A = K, Rb, Cs] also mixed valence compounds are known which exhibit similar structures to $BaFe_2Se_3$.[30,31] As already mentioned above, the structure of $BaFe_2Se_3$ contains more regular Fe_2Se_3 double chains than $Fe_{10}Se_{12}(en)_7$. The compound shows long range antiferromagnetic order below ~ 255 K.[28,29] Whether the deviation from paramagnetism in $Fe_{10}Se_{12}(en)_7$ can be attributed to a similar ordering remains to be clarified.

The inverse susceptibility of $Fe_3Se_4(en)_3$ shows no linear temperature dependence, whereby it must be noted that Fe [<1 wt%] is present in the sample. Modified Curie-Weiss fitting of the almost linear range between 100 K and 300 K nevertheless yields satisfactory results with χ_0 = 0.0227(1) $cm^3\ mol^{-1}$, Θ = -6.42(47) K and C = 4.39(2) $cm^3\ mol^{-1}$ K. The small paramagnetic moment of 5.93(2) μ_B per formula unit again suggests the assumption that mainly the Fe atoms in $Fe(en)_3$ complexes contribute to the magnetization. The moment $\mu_{eff}(Fe_{complex})$ = 5.93(2) μ_B would give high spin Fe^{3+} for the $Fe(en)_3$ complexes. Under consideration of the average Fe-N distance of 2.216(20) Å in $Fe_3Se_4(en)_3$ and the similar struc-

ture as $Fe_3Se_4(en)_2$, however, a high spin Fe^{2+} state appears more likely here as well. Therefore the formula $[Fe^{3+}{}_2Se^{2-}{}_4][Fe^{2+}(en)_3]$ is obtained. So $Fe_3Se_4(en)_3$ like $Fe_3Se_4(en)_2$ would contain only Fe^{3+} in the chains.[4] The cause of the deviation from paramagnetism remains to be examined. Isothermal magnetization curves at 1.8 K indicate no ferromagnetism besides the Fe side phase [see Figure A-1].

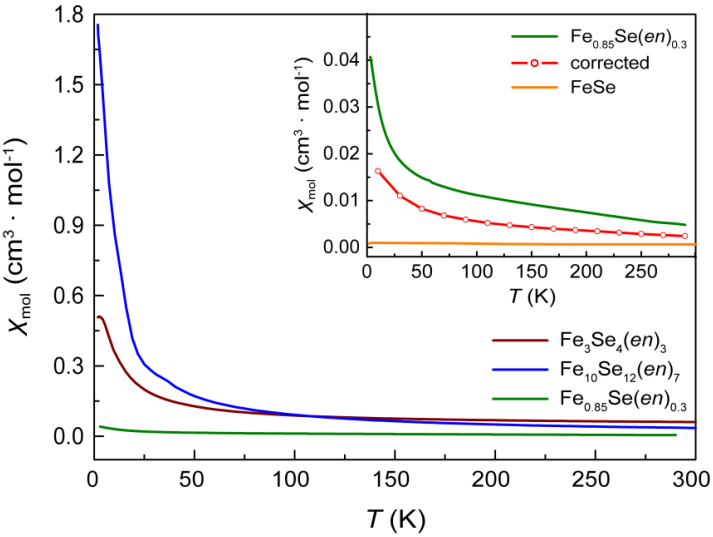

Figure 2-8 Temperature dependence of the magnetic susceptibilities of $Fe_3Se_4(en)_3$ [red], $Fe_{10}Se_{12}(en)_7$ [blue] and $Fe_{0.85}Se(en)_{0.3}$ [green] at 1 T. Insert: Hondo-Owen corrected susceptibility of $Fe_{0.85}Se(en)_{0.3}$ [red] compared to susceptibility of FeSe [orange] at 1 T.

$Fe_{0.85}Se(en)_{0.3}$ is paramagnetic in the whole temperature range, but the inverse susceptibility is not linear and gives no suitable Curie-Weiss fitting. Isothermal magnetization curves [see Figure A-1] and the field dependency of the susceptibility indicate a ferromagnetic component, which may origin from traces of ferromagnetic impurities like Fe or

Fe_3O_4. In order to estimate the true paramagnetic susceptibility, the data were corrected by the Hondo-Owen method [insert in Figure 2-8], which is basically an extrapolation of the magnetization to infinite external field ($1/B \rightarrow 0$).[32] The correction yields 2×10^{-3} cm^3 mol^{-1} at 295 K which is still one order of magnitude larger than in β-FeSe with 6.6×10^{-4} cm^3 mol^{-1} [see inset in Figure 2-8]. The reason for the absence of superconductivity in $Fe_{0.85}Se(en)_{0.3}$ is not clear. In the literature the composition of β-FeSe is discussed to play an important role and superconductivity only occurs near to 1 : 1 stoichiometry.[33] This assessment is limited to iron rich phases though, because binary compounds $Fe_{1-x}Se$ with significant iron deficiency do not exist in PbO-type structure. In contrast to this, superconducting amine intercalated compounds $A_x(en)_yFe_{2-z}Se_2$ [A = Li, Na, Sr] are Fe deficient with z up to 0.14.[15-17,34] At least in these compounds superconductivity is not suppressed by iron vacancies. Other reasons for the absence of superconductivity in $Fe_{0.85}Se(en)_{0.3}$ may be the different stacking of the FeSe layers compared with β-FeSe or the lack of electron doping due to the neutral amine molecules in the interlayers. The latter assumption is supported by the literature where $Na_{0.39}(en)_{0.77}Fe_2Se_2$ with T_c = 45 K is found to deintercalate Na by air exposure to form a dopant free phase.[35] The deintercalation is accompanied by the disappearance of superconductivity in the compound so electron doping seems to be a decisive factor for superconductivity in separated $Fe_{1-x}Se$ layers.

Conclusions

We achieved systematic dimensional reduction in the Fe-Se-*en* system by introducing dilution as a new control parameter in solvothermal synthesis. By diluting the solvent *en* with *glycerol*, which does not participate in the reaction, we were able to stabilize different terminated fragments of

the β-FeSe layered structure. In $Fe_{0.85}Se(en)_{0.3}$ the layers are maintained but separated by uncharged molecular interlayers. $Fe_{10}Se_{12}(en)_7$ shows double chains composed of tetrahedra sharing three edges. Further reduction to single chains is realized in $Fe_3Se_4(en)_3$ and $Fe_3Se_4(en)_2$ which exhibit comparable $FeSe_2$ chains but different connections between the chains. A temperature dependent phase diagram shows the stability ranges of the compounds and the strong dependence of the structure dimensionality on dilution. Measurements of the thermal expansion of the lattice parameters illustrate the different dimensionalities of the compounds. Additionally we investigated the impact of the dimensional reduction on the magnetic properties, which range from superconductivity and antiferromagnetism to paramagnetism.

2.1.1 Polymorphism of $Fe_3Se_4(en)_3$

Abstract

The unknown side phase in samples of $Fe_3Se_4(en)_3$ [described in chapter 2.1] was successfully uncovered by single crystal X-ray diffraction measurements. Structure solution yielded the monoclinic space group $P2_1$ and lattice parameters a = 9.811(2) Å, b = 11.417(1) Å, c = 16.639(3) Å and β = 92.18(1)°. The structural motifs, $FeSe_2$ chains and $Fe(en)_3$ complexes, are almost identical to those in $Fe_3Se_4(en)_3$ and differ only in the distortion of the chains. $Fe_3Se_4(en)_3$ thus occurs in two polymorphs, α- and β-phase, which cannot be separated *via* synthesis.

Introduction

Low-dimensional crystal structures are created by a high anisotropy of the chemical bonding. Within layers or chains there are strong ionic, covalent or metallic bonds, while between these motifs only weak interactions exist.[36] Considering transition metal chalcogenides, low-dimensional structures are more likely to occur for sulfides and selenides, since oxides preferentially exhibit ionic bonds, while tellurides tend to form metallic 3D networks.[9,36] Beside the well-known group of 2D layered transition metal dichalcogenides MCh_2, the interest in stoichiometric MCh layered compounds built up by edge-sharing tetrahedra is growing.[37] This is also due to the discovery of superconductivity in iron based chalcogenides.[19] Corresponding one-dimensional structure motifs appear in AFeCh_2 compounds [A = K, Rb, Cs; Ch = S, Se], for example, where the tetrahedral chains are separated by alkali ions.[27,38] Through solution-based reactions the incorporation of organic ligands between the 1D chains succeeds, thereby reducing the strength of the ionic inte-

ractions.[4,5,39,40] In $Fe_3Se_4(dien)_2$ and $Fe_3Se_4(en)_3$ the chains are only connected *via* hydrogen bonds from Se atoms of the $FeSe_{4/2}$ tetrahedra to H atoms of Fe coordinating amine molecules.[5,39] Depending on the strength of the bonding, the $FeSe_2$ chains in all compounds show different distortion.

In this chapter the structure of the *β*-polymorph of $Fe_3Se_4(en)_3$, solved from single crystal X-ray diffraction, is shown. Despite similar structural motifs and interactions between $FeSe_2$ chains and $Fe(en)_3$ complexes the distortion of the 1D chains differs in comparison to the α-polymorph.

Experimental

Samples of $Fe_3Se_4(en)_3$ were prepared *via* solvothermal synthesis in Teflon-lined steel autoclaves [50 mL]. Fe powder [Chempur, 99.9%] and Se powder [Chempur, 99.999%] in 1 : 1 molar ratio for a total amount of 50 mg, 100 mg of NH_4Cl [Kraft, purissimum] and 35 mL Ethane-1,2-diamine [*en*, Merck, ≥99%] were filled in the autoclave and heated up to 170 °C or 180 °C for 5 days. The black, needle shaped products were washed with water, ethanol and acetone and subsequently dried under vacuum at room temperature.

Single crystals were isolated using a light microscope and the unit cells were determined by X-ray diffraction on a Bruker D8-Quest diffractometer [Mo-K_α radiation; graphite monochromator]. Entire data collection was done for a crystal with hitherto unknown cell parameters. Structure solution and refinement was carried out using Jana2006 program package.[11] X-ray diffraction patterns at room temperature and temperatures between 373 K and 473 K were collected on a Stoe Stadi P diffrac-

tometer [Mo-$K_{\alpha 1}$ radiation; Ge-111 monochromator] with capillary sample holder, and Rietveld refinements were performed with TOPAS.[10]

Results and Discussion

All powder diffractograms of $Fe_3Se_4(en)_3$ samples contain unknown reflections, as exemplary visible in Figure 2-4. Single crystals with lattice parameters deviating from $Fe_3Se_4(en)_3$, isolated by X-ray diffraction tests, show a monoclinic cell with a = 9.811(2) Å, b = 11.417(1) Å, c = 16.639(3) Å and β = 92.18(1)°. Final structure solution [Mo-K_α radiation] gives the space group $P2_1$ and a similar structure to $Fe_3Se_4(en)_3$, shown in Figure 2-9 [hydrogen bond lengths, angles and ADP extension factors [1.2] were constrained according to the literature].[12]

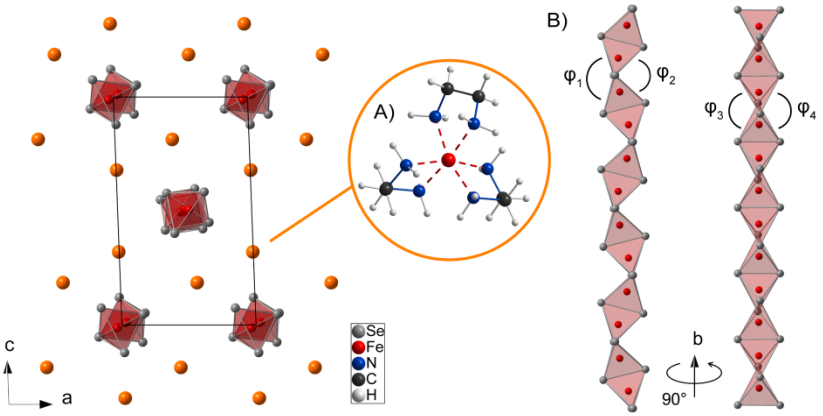

Figure 2-9 Schematic view of the β-$Fe_3Se_4(en)_3$ structure along [010]: orange spheres represent $Fe(en)_3$ complexes (A); (B) One $FeSe_2$ single chain of β-$Fe_3Se_4(en)_3$ projected along two directions linked by a 90° rotation around the b axis. Tilting of the chains is defined by the angles φ_1 to φ_4 between adjacent faces of two edge sharing tetrahedra.

The new structure is built up by the same structural motifs as $Fe_3Se_4(en)_3$, parallel $FeSe_2$ single chains separated by $Fe(en)_3$ complexes [Figure 2-9 B and A]. The compounds therefore exhibit the identical stoichiometry and are polymorphs. Hence, in the following the monoclinic structure, described in this chapter, is referred to as β-$Fe_3Se_4(en)_3$, while the triclinic structure, described in chapter 2.1, is referred to as α-$Fe_3Se_4(en)_3$.

Table 2-1 Average Fe-Se distances and angles ∢Se-Fe-Se, describing the distortion of the FeSe tetrahedra, and angles φ_1-φ_4, describing the distortion of the $FeSe_2$ chains, for the polymorphs of $Fe_3Se_4(en)_3$ in comparison with $Fe_3Se_4(en)_2$.

	α-$Fe_3Se_4(en)_3$	**β-$Fe_3Se_4(en)_3$**		**$Fe_3Se_4(en)_2$** [4]
		chain 1	**chain 2**	
d(Fe-Se)	2.34(1)-2.42(1) Å	2.35(1)-2.40(1) Å	2.34(1)-2.40(1) Å	2.35-2.40 Å
∢(Se-Fe-Se)	100.0(1)-118.1(1)°	104.3(1)-115.8(1)°	101.6(1)-114.7(1)°	103.8-117.1°
φ_1, φ_2	88.51(2)°, 145.83(3)°	100.43(4)°, 127.00(5)°	85.71(5)°, 144.87(6)°	110.2°, 119.1°
φ_3, φ_4	117.34(2)°, 117.38(2)°	101.29(4)°, 127.48(5)°	115.65(5)°, 116.54(5)°	114.5°, 114.5°

Despite the very similar arrangement of the structural motifs differences between the two polymorphs can be identified. The main reason for the approximate doubling of the unit cell volume in the monoclinic β-polymorph is the appearance of two crystallographic independent $FeSe_2$ chains with different distortion. Thereby, the distortion of the tetrahedra themselves is not crucial with average Fe-Se distances of 2.37(2) Å for both chains and angles ∢Se-Fe-Se of 104.3(1)-115.8(1)° and 101.6(1)-114.7(1)°, respectively. Rather, the tilting of the edge shar-

ing tetrahedra towards each other is decisive, which is defined by the four angles φ_1-φ_4 between adjacent faces of neighboring tetrahedra [see Figure 2-9 B]. Table 2-1 gives φ_1-φ_4 for both chains in comparison to the α-polymorph and $Fe_3Se_4(en)_2$, which also exhibits $FeSe_2$ chains connected *via* $Fe(en)_2$ complexes.[4] Chain 1, located at the center of the unit cell [see Figure 2-9], is more distorted than the almost regular chains in $Fe_3Se_4(en)_2$, but less than the chains in α-$Fe_3Se_4(en)_3$. Chain 2, located at the cell edges, shows similar values as the significantly distorted chain in the α-compound. Nevertheless, the Fe-Se distances and angles ∢Se-Fe-Se, which reflect the distortion of the tetrahedra, are in the same range for all structures.

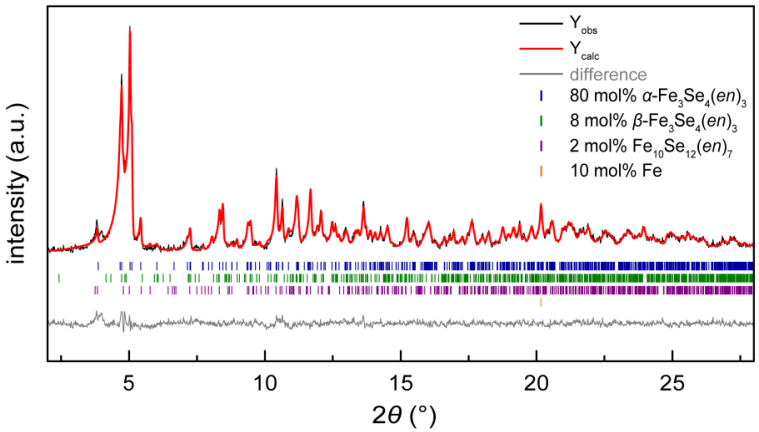

Figure 2-10 Rietveld refinement of a powder X-ray diffraction pattern [Mo-$K_{\alpha1}$] with 80 mol% *α*-$Fe_3Se_4(en)_3$ [blue], 8 mol% *β*-$Fe_3Se_4(en)_3$ [green], 2 mol% $Fe_{10}Se_{12}(en)_7$ [purple] and 10 mol% Fe [orange].

The distances of the parallel $FeSe_2$ chains are slightly increased in the *β*-polymorph with 9.50(1) Å compared to the α-compound with 9.10(1) Å. Average distances of the centers of the $Fe(en)_3$ complexes are

comparable with 8.01(7) Å and 8.17(2) Å perpendicular to the chain direction and 11.42(1) Å and 11.67(1) Å along chain direction, for the *β*- and α-polymorph, respectively. Fe-N distances within the complexes are d_{avg}(Fe-N) = 2.24(3) Å and shortest hydrogen bonds to the chains are d_{avg}(Se···H-N) = 2.72(15) Å. These values are also comparable to the known structures in the Fe-Se-*en* system containing Fe(*en*)$_3$ complexes, α-$Fe_3Se_4(en)_3$ [d_{avg}(Fe-N) = 2.22(2) Å, d_{avg}(Se···H-N) = 2.77(19) Å] and $Fe_{10}Se_{12}(en)_7$ [d_{avg}(Fe-N) = 2.22(1) Å, d_{avg}(Se···H-N) = 2.75(16) Å].

For the powder X-ray diffraction data of all synthesized samples Rietveld refinements reveal α-$Fe_3Se_4(en)_3$ as the main phase accompanied by around 10 mol% *β*-$Fe_3Se_4(en)_3$. No samples containing pure α- or *β*-phase were produced. Figure 2-10 exemplary shows a Rietveld refinement of a sample additionally containing 2 mol% $Fe_{10}Se_{12}(en)_7$ and 10 mol% elemental Fe. In order to investigate a potential phase transition at high temperatures *in-situ* powder X-ray diffraction data was measured between 100 °C and 200 °C [see Figure 2-11]. Decomposition of the sample starts at 140 °C, under formation of $FeSe_2$ and little Fe_3Se_4 by release of *en*, and is complete above 180°C. Interestingly, a continuous decrease of the *β*-$Fe_3Se_4(en)_3$ molar fraction is observed upon heating before the decomposition starts [see insert in Figure 2-11]. Above 130 °C the *β*-phase vanishes completely, while the fraction of the α-phase increases till that temperature. This indicates a phase transition from *β*- to α-polymorph at elevated temperatures. However, due to the poor resolution of the measurements, a decomposition of *β*-$Fe_3Se_4(en)_3$ to amorphous products cannot be excluded.

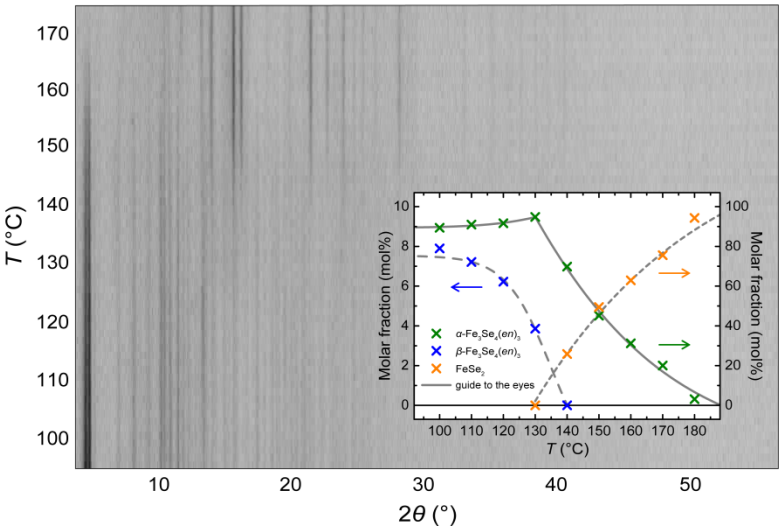

Figure 2-11 Film plot of the *in-situ* high-temperature powder X-ray diffraction data [Mo-$K_{\alpha 1}$]. Insert: Molar fraction of β-$Fe_3Se_4(en)_3$ [blue], α-$Fe_3Se_4(en)_3$ [green] and $FeSe_2$ [orange] in mol% from Rietveld refinement. Grey lines are guides to the eyes.

Conclusions

The presence of the unknown side phase in samples of $Fe_3Se_4(en)_3$ can now be attributed to polymorphism revealed by structure solution of the β-phase through single crystal X-ray diffraction measurements. α- as well as β-$Fe_3Se_4(en)_3$ are built up by parallel $FeSe_2$ chains and $Fe(en)_3$ complexes, and differ only in the distortion of the chains. Due to this pronounced structural similarity, no synthetic separation of the polymorphs is possible. *In-situ* high temperatures powder X-ray diffraction measurements are consistent with a phase transition from β- to α-polymorph before decomposition of the sample.

2.1.2 $Fe_{0.85}Se(en)_{0.3}$ – Separated FeSe layers with stripe-type crystal structure by intercalation of neutral spacer molecules

Juliane Stahl and Dirk Johrendt

Parts published online: *arXiv:1706.00314* [cond-mat.supr-con] **2017**.

Abstract

Solvothermal intercalation of ethylenediamine molecules into FeSe separates the layers by 10.78 Å and creates a different stacking. $Fe_{0.85}Se(en)_{0.3}$ is not superconducting although each layer exhibits the structure and Fermi surface of superconducting FeSe. $Fe_{0.85}Se(en)_{0.3}$ requires electron-doping for high-T_c like monolayers FeSe@$SrTiO_3$, whose much higher T_c may arise from the oxide surface proximity.

Introduction

The most exciting discovery in the field of iron based superconductors during the last five years is probably the observation of superconductivity as high as 65-100 K in iron selenide [β-FeSe] monolayers grown on $SrTiO_3$ substrates with oxygen defects.[41-43] This has demonstrated the general potential of iron selenide layers to achieve superconductivity near or even above liquid nitrogen temperature, however, reasons for the giant increase of the transition temperature from 8 K in bulk FeSe are still under debate.[44] Calculations suggest an increased electron-phonon-coupling through the proximity of the substrate, which remains never-

theless too weak to explain a critical temperature of 65 K.[45] Interestingly, FeSe monolayers grown on defect-free $SrTiO_3$ or on graphene are not superconducting, while recent experiments with potassium-doped three-layer films suggest that high-T_c superconductivity in FeSe requires electron doping of the layers.[46,47] This is in line with the fact that the T_c of FeSe increases from 8 K to about 30 K through intercalation of alkaline metals.[48] Unfortunately, these materials are phase separated into a strongly magnetic non-superconducting phase and a superconducting phase of still unclear structure.[49] Relatively high transition temperatures up to 45 K occur in intercalation compounds of FeSe with organic molecules as spacers and alkaline metals as electron donors.[15-17,50,51] Consequently, neutrally intercalated FeSe with a large interlayer distance and weak interactions would serve as a bulk analogue of the undoped non-superconducting FeSe monolayers mentioned above without the proximity of the oxide surface. Given that the detailed structure of the monolayers are still lacking, the structure of such a 'free monolayer' between weak interacting neutral molecules is a new piece in the unresolved puzzle of superconductivity in iron selenide.

Here, we report the synthesis of $Fe_{0.85}Se(en)_{0.3}$ through a solvothermal route from Fe and Se on the one hand and from β-FeSe on the other. While the determination of the monoclinic crystal structure is shown in chapter 2.1, this chapter focuses on the phase transition to orthorhombic symmetry and the deintercalation of *en* by thermal treatment. Furthermore, we show why the non-superconducting compound can be interpreted as a bulk analogue of undoped FeSe monolayers.

Experimental

β-FeSe was prepared by vapor-transport growth.[52] Fe powder [437.6 mg; Chempur, 99.9%] and Se powder [562.4 mg; Chempur, 99.999%] in a molar ratio of 1.1 : 1 and a mixture of KCl [2.25 g; Grüssing, 99.5%, dried] and $AlCl_3$ [7.75 g; Alfa Aesar, 99.985%] were sealed in a glass ampoule of 4 cm length and 5 cm diameter. The ampoule was heated to 390 °C at the bottom and 260-280 °C at the top for 5-10 days. $Fe_{0.85}Se(en)_{0.3}$ was synthesized *via* a solvothermal route from Fe and Se or *β*-FeSe, respectively, in a Teflon-lined steel autoclave [50 ml]. 20.7 mg Fe [Chempur, 99.9%] and 29.3 mg Se [Chempur, 99.999%] or 50 mg *β*-FeSe together with 100 mg NH_4Cl [Kraft, purissimum] as mineralizer were mixed with 17.5 mL ethylenediamine [*en*; Merck, > 99%] and 17.5 mL propane-1,2,3-triol [*glycerol*; Grüssing, 99%] and reacted at 220 °C for 5-20 days. After washing with water, ethanol and acetone the products were dried under vacuum at room temperature.

Room temperature and *in-situ* high temperature X-ray diffraction patterns were collected using a Stoe Stadi P diffractometer [Mo-$K_{\alpha 1}$ radiation; Ge-111 monochromator] with capillary sample holder. TOPAS was used for Rietveld refinements.[10] Compositions of the samples were investigated by energy-dispersive spectroscopy measurements on a Zeiss Evo-Ma10 microscope with Bruker X-Flash 410-M detector.[53,54] Since carbon containing pads were used the amount of *en* was determined solely by the nitrogen content. Magnetic measurements were carried out using a custom-made dual-coil AC-susceptometer [$3 \cdot 10^{-4}$ T, 1333 Hz].

Results and Discussion

Solution and refinement of the crystal structure and determination of the composition of $Fe_{0.85}Se(en)_{0.3}$ are shown in chapter 2.1 [detailed information in Table A-6 to Table A-9]. The FeSe layers composed of $FeSe_{4/4}$ tetrahedra are separated by 10.78 Å in $Fe_{0.85}Se(en)_{0.3}$ and show different stacking than β-FeSe but comparable to $LaMnSi_2$-type structures.[18] Deintercalation of *en* molecules by thermal treatment can be observed through thermogravimetric measurements. Heating to 230 °C in argon atmosphere completely removes *en* and β-FeSe is regained. High-temperature PXRD data indicate an irreversible structural transition beginning at 180°C [Figure 2-12] with a continuous decrease of the monoclinic angle till 200°C [insert in Figure 2-12], where the deintercalation of the *en* molecules starts.

To further investigate the phase transition, samples of $Fe_{0.85}Se(en)_{0.3}$ were prepared by intercalation of *en* into transport grown β-FeSe crystals [blue curve in Figure 2-13]. Intercalation of *en* is not complete under these conditions and the products contain some unreacted FeSe [red curve in Figure 2-13]. Heating of the monoclinic product to 210 °C for 4.5 h under argon atmosphere yields only orthorhombic $Fe_{0.85}Se(en)_{0.3}$ [β = 90°, space group *Cmcm*] with a slightly increased amount of FeSe [orange curve in Figure 2-13]. This indicates that the onset of the decomposition occurs simultaneously with the irreversible structural transition. We suggest that the transition is driven by the beginning deintercalation of *en*, which impedes further studies of the high temperature phase. Further heating to 300 °C leads to completely deintercalated FeSe and Fe_3Se_4 [back curve in Figure 2-13] which is consistent with the *in-situ* high-temperature PXRD measurements.

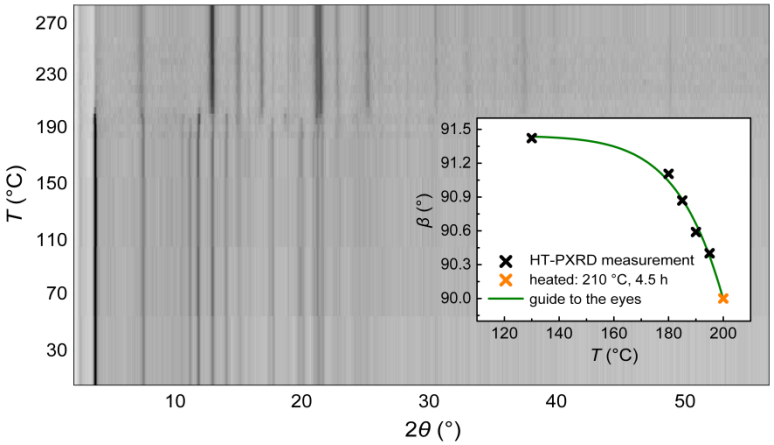

Figure 2-12 Film plot of the *in-situ* high-temperature powder X-ray diffraction data [Mo-$K_{\alpha1}$]. Insert: Trend of the monoclinic angle β from Rietveld refinements. Additionally the angle β of the orthorhombic sample heated to 210 °C is inclosed [orange].

Through AC susceptibility measurements down to 4 K we were able to examine the influence of the intercalation, the phase transition and the deintercalation on the magnetic properties. The transport grown FeSe sample is superconducting below 9 K [blue curve in Figure 2-14]. The intercalation of *en* reduces the superconducting volume fraction to about 12 Vol%, which is consistent with $Fe_{0.85}Se(en)_{0.3}$ being paramagnetic over the whole temperature range [see chapter 2.1] and the superconducting FeSe impurity remaining after solvothermal reaction [red curve in Figure 2-14]. The critical temperature drops to about 5.5 K displaying the impact of the solvothermal conditions on the superconducting properties of the FeSe crystals. Heating to 210 °C under argon atmosphere accomplishes the complete phase transition and increases the FeSe impurity by incipient deintercalation of *en*. The superconducting volume fraction and transition temperature do not change considering the inac-

curacy of the method [orange curve in Figure 2-14]. Disappearance of the superconducting transition is observed if *en* is fully deintercalated from the sample [black curve in Figure 2-14]. The slight increased values of the susceptibility compared to transport grown FeSe in paramagnetic state are due to the ferrimagnetic impurity phase Fe_3Se_4.[55,56]

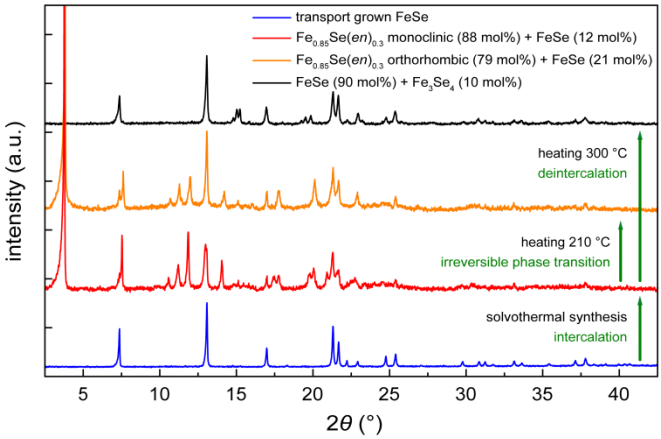

Figure 2-13 Powder X-ray diffraction patterns [Mo-$K_{\alpha1}$] of transport grown β-FeSe [blue], after intercalation of *en via* solvothermal method [red], product heated to 210 °C [orange] and 300 °C [black], respectively. Molar proportions given were determined by Rietveld refinements.

Since the stoichiometry of $Fe_{1-x}Se$ phases is considered to be crucial for the magnetic properties, we examined the composition of the samples using EDS analysis. The transport grown β-FeSe crystals show a ratio of Fe : Se = 1.12(12) : 1. Contrary to previous findings in the literature, this deviation from the ideal stoichiometry does not prevent the superconducting transition.[33,57,58] It should be noted, however, that EDS analyses show a large systematic error, which affects the absolute values but not the comparability of our samples. The intercalated monoclinic product exhibits a stoichiometry of $Fe_{0.78(2)}Se(en)_{0.28(9)}$ which is in line with the

results for products synthesized from the elements [see chapter 2.1 and Table A-9]. The loss of Fe compared to the amount in the starting FeSe crystals is plausible for the applied solvothermal method. Fe can be extracted by the solvent and removed during washing. After the phase transition to orthorhombic symmetry the stoichiometry changes to $Fe_{0.77(1)}Se(en)_{0.19(8)}$. While the Fe content does not change, the product contains significantly less *en* molecules. This in turn shows that the phase transition is accompanied by the starting deintercalation of *en*. The loss of *en* results in a shrinkage of the crystallographic axes from a = 3.90(1) Å, b = 21.60(1) Å and c = 3.86(1) Å of the monoclinic product to a = 3.87(1) Å, b = 21.35(1) Å and c = 3.84(1) Å after structural transition [values taken from Rietveld refinement of PXRD data]. Nevertheless, it is noteworthy that at such low *en* content the compound still comprises widely separated FeSe layers [d = 10.7 Å].

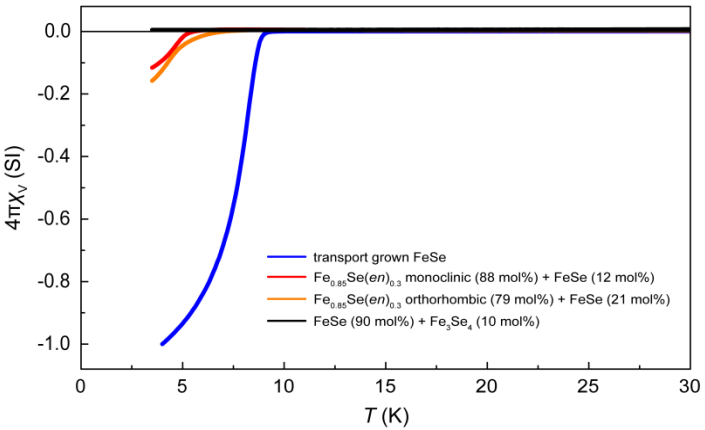

Figure 2-14 AC-susceptibility measurements at $3 \cdot 10^{-4}$ T of transport grown β-FeSe [blue], monoclinic $Fe_{0.85}Se(en)_{0.3}$ after intercalation of *en* [red], orthorhombic $Fe_{0.85}Se(en)_{0.3}$ after heating to 210 °C [orange] and deintercalated FeSe after heating to 300 °C [black].

After complete deintercalation the recovered FeSe crystals are iron deficient with a ratio of Fe : Se = 0.79(5) : 1. The stoichiometry of the layers therefore does not change on return to the stacking sequence of tetragonal β-FeSe. Interestingly, the deintercalated product exhibits the same lattice parameters of a = 3.77(1) Å and c = 5.52(1) Å as the transport grown starting material according to Rietveld refinement of powder X-ray diffraction data. This is unexpected with regard to the different occupation of the Fe site. Similar iron deficient $Fe_{1-x}Se$ samples with x = 0.2 can be produced by extracting K from $K_2Fe_4Se_5$ crystals using iodine.[59] These samples are not superconducting, like our deintercalated product.

Iron deficiency may also account for the absence of superconductivity in the *en* intercalated samples. On the contrary, compounds with intercalated alkali metal $A_{1-x}Fe_{2-y}Se_2$ [A = K, Rb, Cs] or co-intercalated alkali metal and diamine $A_{1-x}Fe_{2-y}Se_2(C_nH_{2n+4}N_2)_z$ [A = Li, Na; n = 0, 2, 3, 6] are superconducting in spite of significant Fe vacancies up to y = 0.2.[15-17,34,60-64] The layer stacking of these compounds is $ThCr_2Si_2$-type like and therefore differs from the stacking in $Fe_{0.85}Se(en)_{0.3}$, which also may be responsible for the absence of superconductivity in our samples. In order to study the effect of layer stacking on the electronic structure, we have calculated the Fermi surfaces of orthorhombic β-FeSe, FeSe layers stacked as in $Fe_{0.85}Se(en)_{0.3}$ [*en* molecules were omitted in the calculation] and hypothetically electron-doped layers [Figure 2-15]. $Fe_{0.85}Se(en)_{0.3}$ largely retains the typical Fermi surface topology of β-FeSe in spite of the different layer stacking, whereby the two-dimensional character becomes more pronounced due to the much larger layer separation. Adding about 0.2 electrons per formula unit increases the Fermi energy and the hole-like parts of the surface around the Γ-point vanish. This is exactly what has been observed in three-layer FeSe which becomes superconducting

only by doping with potassium.[44,47] Since superconducting $A_{1-x}Fe_{2-y}Se_2(en)_z$ compounds show comparable iron deficiency and FeSe layer distances, and the layer stacking does not change the Fermi surface structure, we suggest the lack of electron doping to be the decisive reason for the absence of superconductivity in $Fe_{0.85}Se(en)_{0.3}$.[15-17] Therefore, it can be interpreted as a parent compound for the alkali metal and *en* co-intercalated superconductors. This is supported by the possibility of Na deintercalation from $Na_{0.39}Fe_2Se_2(en)_{0.77}$ [T_c = 45 K] resulting in a non-superconducting dopant free phase.[35] In contrary, *Gao et al.* report on solvothermally produced samples of $Fe_{1.04}Se(en)_{0.3}$ exhibiting a T_c of about 10 K without doping by additional metal intercalation.[65] However, the authors discuss the possibility of electron doping by excess Fe occupying interstitial sites, which may account for the superconducting transition.

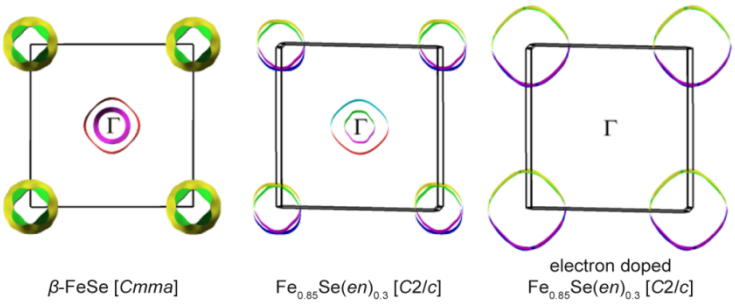

Figure 2-15 Fermi surfaces of β-FeSe [*Cmme*; left], FeSe-layers stacked as in $Fe_{0.85}Se(en)_{0.3}$ [middle] and hypothetically electron-doped FeSe layers [right]. *en* molecules were omitted in the calculation.

Conclusions

In conclusion, we have shown that the intercalation of a remarkably small amount of *en* molecules between FeSe layers increases the layer spacing to 10.87 Å in $Fe_{0.85}Se(en)_{0.3}$. Thus, we have realized very weakly interacting and charge neutral FeSe layers with a structure almost identical to those of superconducting FeSe. We consider $Fe_{0.85}Se(en)_{0.3}$ as a bulk analogue to the monolayer materials grown on $SrTiO_3$, albeit without the proximity of the rigid oxide surface. Our results support recent findings that monolayers require electron doping to become superconducting at high T_c and we show evidence that this is also the case for *en*-intercalated bulk materials. The latter have so far reached critical temperatures of 45 K which is well below 65-100 K of the monolayers. One possible reason may be the additional increase of the electron-phonon coupling in the monolayers on the rigid oxide substrate in contrast to the rather soft bearing of the FeSe layers between *en*-molecules.[45]

2.2 Pressure and dilution dependency in the phase diagram of the Fe-Se-*en* system

Abstract

In solvothermal synthesis chemical control over the tetrahedra connectivity in compounds of the Fe-Se-*en* system by dilution is attributed to the varied ligand-to-metal ratio. By changing the diluent of the solvent *en* from *glycerol* to methanol, the reaction pressure is excluded as decisive parameter. The phase space diagram with methanol confirms the reduced dimensionality upon dilution, even though the pressure shows the opposing trend. With it, the new compound $Fe_{20}Se_{24}(en)_{13}(MeOH)$ is obtained, which is structurally similar to $Fe_{10}Se_{12}(en)_7$, but also contains novel motifs.

Introduction

Solvothermal synthesis is generally defined as a chemical reaction in a solvent under autogeneous pressure, whereby the pressure is induced by heating to a temperature above the boiling point of the solvent in a pressure-tight vessel.[66,67] If water is used as solvent, the method is referred to as hydrothermal synthesis, which was first mentioned in the literature already in the 19th century.[68,69] Since then, the method became widespread, as metastable compounds, unusual oxidation states or low-temperature phases can be obtained under comparatively mild conditions.[69] Today, it is an established method for the preparation of new materials in addition to the synthesis of nanostructured particles or compounds with uncommon morphology.[66] In contrast to conventional solid state synthesis, a great number of parameters play a decisive role in solvothermal synthesis. In addition, these parameters largely influence each

other. The chemical parameters, like oxidation and reduction potential, pH value and solubility or complexing properties, are mainly determined by the nature of the solvent. They can be varied by admixture of further solvents or additives to gain control of the mechanism or the type and shape of the obtained products.[66] However, the choice of the composition and concentration of the solid precursors is also important for targeted synthesis. In addition to the chemical parameters, thermodynamic parameters affect the reaction. Temperature and reaction time can easily be controlled, whereas the reaction pressure depends on many factors, like the physical properties of the solvent, dissolved salts, temperature and percentage fill.[66,67] Effects of the individual parameters in solvothermal synthesis should therefore be carefully examined to achieve the desired results.

In chapter 2.1 [Figure 2-6] the phase space diagram of the Fe-Se-*en* system is shown in dependence of the dilution of the solvent *en* with *glycerol* and the synthesis temperature.[39] The degree of condensation of the $FeSe_4$ tetrahedra in the products turns out to increase with the amount of *glycerol*. This is attributed to the reduced availability of *en* during synthesis, as the ligand-to-metal ratio is lowered upon dilution. The dilution dependency of the reaction pressure should be taken into account, though, as the pressure might also affect the obtained products. Since the vapor pressure of *glycerol* [0.06 bar at 200 °C] is much lower compared to *en* [7.85 bar at 200 °C], dilution will reduce the reaction pressure.[70,71] In this chapter, we examine the dependence of the Fe-Se-*en* system on the pressure. This is done by replacing the diluent *glycerol* by methanol, which exhibits a similar chemical behavior but a much higher vapor pressure [40.4 bar at 200 °C].[72] It turns out, that methanol can be incorporated into the product structure, resulting in the compound $Fe_{20}Se_{24}(en)_{13}(MeOH)$. It contains double chains of $FeSe_4$ tetrahedra, like

$Fe_{10}Se_{12}(en)_7$, therefore still allowing a discussion of the dimensional reduction in dependency of the dilution. We create a similar phase diagram to compare both diluents and measure the synthesis pressure to give an insight on the behavior upon dilution.

Experimental

The pressure dependence in the Fe-Se-*en* phase diagram was analyzed using a stainless steel high pressure reactor with 150 mL Teflon liner, which allows measurement of pressure and temperature within the reaction zone. 62.1 mg Fe powder [Chempur, 99.9%], 87.9 mg Se powder [Chempur, 99.999%] and 300 mg NH_4Cl [Kraft, purissimum] were weighed to correspond the solvent-to-metal ratio used for syntheses described in chapter 2.1. Ethane-1,2-diamine [*en*, Merck, ≥99%] diluted with 0%, 20%, 40%, and 60% either propane-1,2,3-triol [*glycerol*, Grüssing, 99%] or methanol [MeOH, Fisher Scientific, HPLC grade] with total amount of 105 mL [70% filling fraction] was added. For each mixture, temperatures between 150 °C and 190 °C were approached with steps of 5 °C and held for about 1 d. The pressure was measured before the next step. After cooling, the products were washed with water, ethanol and acetone and dried under vacuum at room temperature. The obtained products corresponded to the expected ones according to the phase diagrams.

The Fe-Se-*en* phase diagram in dependence of the dilution of *en* and the reaction temperature [180-220 °C] with methanol as diluent was created using the same procedure as described in chapter 2.1.

Analysis of the crystal structure of $Fe_{20}Se_{24}(en)_{13}(MeOH)$ at 110 K was done *via* X-ray diffraction on a Bruker D8-Venture diffractometer

[Mo-K_α radiation]. For solution and refinement of the structure Jana2006 program package was used.[11] A Stoe Stadi P diffractometer [Mo-$K_{\alpha1}$ radiation; Ge-111 monochromator] with capillary sample holder and a Huber G670 diffractometer [Cu-$K_{\alpha1}$ radiation; Ge-111 monochromator] with flat specimen holder were used to record the powder X-ray diffraction patterns. Rietveld refinements were performed with TOPAS package.[10] The elemental composition of $Fe_{20}Se_{24}(en)_{13}(MeOH)$ was confirmed by energy-dispersive spectroscopy measurements on a Zeiss Evo-Ma10 microscope with Bruker X-Flash 410-M detector and CHNS elemental analysis.

Results and Discussion

Crystal structure. The crystal structure of $Fe_{20}Se_{24}(en)_{13}(MeOH)$ was solved from single crystal X-ray diffraction data [Mo-K_α radiation; for further details see Table A-15 to Table A-17]. During the measurement the crystal was cooled to 110 K, since the *en* and MeOH molecules showed large thermal displacement at room temperature. Nevertheless, the atomic displacement parameters had to be kept equal for bonded C and N atoms and set to isotropic for non-coordinated *en* molecules. Determination of the hydrogen positions was not possible from the obtained data, so these atoms were added with constrained bond lengths [d(C-H) = 1.09 Å or 1.10 Å, d(N-H) = 1.04 Å, d(O-H) = 0.96 Å], tetrahedral angles and isotropic ADPs [extension factor 1.2].[12,73] A triclinic cell with a = 9.23(2) Å, b = 22.23(5) Å, c = 24.35(6) Å, α = 102.18(7)°, β = 99.22(7)°, γ = 93.62(6)° and $P\bar{1}$ symmetry is found at 110 K. The basic structural motifs are parallel Fe_2Se_3 double chains consisting of irregular FeSe tetrahedra linked *via* three edges [see Figure 2-16].

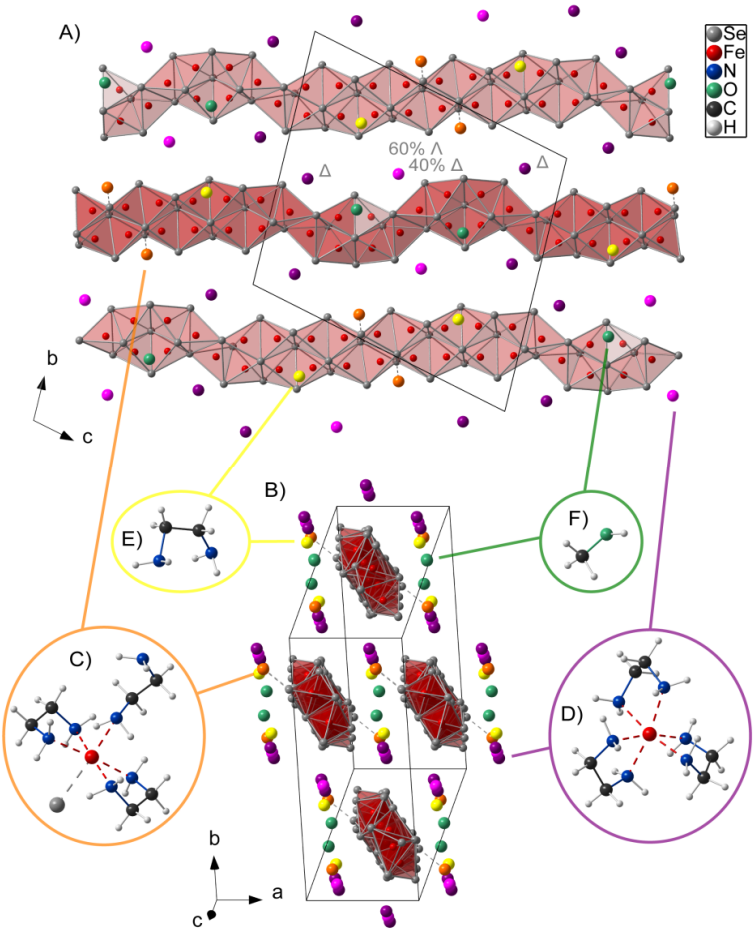

Figure 2-16 Schematic view of the $Fe_{20}Se_{24}(en)_{13}(MeOH)$ structure along [100] (A) and along the Fe_2Se_3 chains (B): orange spheres represent $Fe(en)_3Se$ complexes (C), purple and pink spheres $Fe(en)_3$ complexes (D), yellow spheres *en* molecules (E) and green spheres MeOH molecules (F).

These chains are distorted resulting in μ^4, μ^3 and μ^2 bridging Se atoms. The ratio $\mu^4 : \mu^3 : \mu^2 = 3 : 3 : 6$ compared to the compounds $BaFe_2Se_3$

[4 : 0 : 8], with regular Fe_2Se_3 chains, and $Fe_{10}Se_{12}(en)_7$ [2 : 4 : 6; see Figure 2-2] shows, that the chains in $Fe_{20}Se_{24}(en)_{13}(MeOH)$ are less distorted than in $Fe_{10}Se_{12}(en)_7$, since the ratio approaches the result for $BaFe_2Se_3$.[14] Comparable to $Fe_{10}Se_{12}(en)_7$ the Fe-Se distances slightly differ for μ^3 and μ^4 Se atoms building the backbone [2.380(6)-2.492(6) Å] and μ^2 Se atoms at the edges of the chains [2.331(6)-2.416(7) Å]. The distortion of the tetrahedra itself is also similar to $Fe_{10}Se_{12}(en)_7$ giving angles ∢Se-Fe-Se of 101.9(2)-122.5(3)°.

The Fe_2Se_3 chains are enclosed by two types of $Fe(en)_3$ complexes and non-coordinated *en* and MeOH molecules. The first type of complexes consists of Fe atoms octahedrally coordinated by three *en* molecules, like in $Fe_3Se_4(en)_3$ and $Fe_{10}Se_{12}(en)_7$. These complexes are present at three independent crystallographic sites [Figure 2-16 D]. They exhibit axial chirality, whereby due to the inversion symmetry Δ- and Λ-enantiomers occur in equal numbers, resulting in a racemic structure. For the Fe19 site both enantiomers exist at one position concurrently [pink spheres in Figure 2-16], leading to $Fe(en)_3$ and $Fe(en')_3$ at these positions. These share the Fe and C sites and differ in the N and H or N' and H' sites, respectively. While the Fe and C sites are fully occupied, the positions and occupations of the N and N' atoms can be refined freely, constraining the total occupation to one. H and H' atoms were added as described above with occupations according to the corresponding N atoms. The refinement gives a ratio of $Fe(en)_3 : Fe(en')_3 = 0.58(3) : 0.42(3)$. Figure 2-17 shows the complex at the Fe19 site separated into $Fe(en)_3$ and $Fe(en')_3$ together with site occupation factors of the N atoms. $Fe(en)_3$ is shown in Λ-form and $Fe(en')_3$ in Δ-form [position for this case is labeled grey in Figure 2-16], but it should be noted that both are also present in the opposite form within the structure due to inversion. The occurrence of both enantiomers at the Fe19 site might be explained by the environ-

ment of the complexes. However, there are no significant differences for the shortest Se···H-N distances between the three crystallographic independent Fe(*en*)$_3$ positions. For all complexes, the distances are ranging between 2.160(5) Å and 3.453(7) Å with coordination to both μ^2 and μ^3 bridging Se atoms. Overall, the Se···H-N distances span over a larger range than for the compounds containing Fe(*en*)$_3$ complexes discussed previously, $Fe_3Se_4(en)_3$ and $Fe_{10}Se_{12}(en)_7$. The coordinate bonds at the Fe19 position also hardly differ with d_{avg}(Fe-N) = 2.24(4) Å and d_{avg}(Fe-N') = 2.27(4) Å. The slightly larger value for Fe(*en*')$_3$ may, however, be responsible for the increased Fe(*en*)$_3$: Fe(*en*')$_3$ ratio. The average Fe-N distances of the other two Fe(*en*)$_3$ complexes are 2.24(3) Å and 2.23(3) Å, respectively, so no differences to the Fe19 site are recognizable here, too. Overall, the distances are comparable to those of $Fe_{10}Se_{12}(en)_7$ [d_{avg}(Fe-N) = 2.22(1) Å] and $Fe_3Se_4(en)_3$ [d_{avg}(Fe-N) = 2.22(2) Å] and indicate high spin Fe^{2+} ions in the complexes.[25]

A second type of Fe(*en*)$_3$ complexes is found in $Fe_{20}Se_{24}(en)_{13}$(MeOH) in which the central atom is square-planar coordinated by two *en* molecules. The octahedral coordination is completed by one amine group of an additional *en* and a μ^2 Se atom of the Fe_2Se_3 chains [Figure 2-16 C]. These complexes are referred to as Fe(*en*)$_3$Se in the following. Complexes binding to tetrahedral chains *via* Fe-Se bonds are already known in the literature. For example, $Fe_3Se_4(en)_2$ contains Fe(*en*)$_2$ complexes coordinated square-planar by *en* and connecting two parallel $FeSe_2$ single chains by Fe-Se bonds.[4] In Fe_3Se_4(*tren*) [*tren* = *N*,*N*-Bis(2-aminoethyl)-1,2-ethanediamine] the Fe(*tren*) complexes exhibit four Fe-N bonds to the tetradendate *tren* ligand and two Fe-Se bonds to one $FeSe_2$ chain.[5] Looking at $Fe_{20}Se_{24}(en)_{13}$(MeOH) the Fe-Se bond length of the complex is 2.72(1) Å which is comparable to $Fe_3Se_4(en)_2$ with 2.70 Å and slightly

larger than for Fe_3Se_4(*tren*) with 2.56 Å and 2.67 Å.[4,5] The average Fe-N distance is 2.21(2) Å to the two double coordinated and 2.31(1) Å to the single coordinated ligands, so high spin Fe^{2+} is assumed for the Fe(*en*)$_3$Se complexes, too.[25] The *en* linked only through one amine group is in *gauche* conformation with a dihedral angle of 64(3)°. The Se···H-N distances of the Fe(*en*)$_3$Se complexes range between 2.624(6) and 3.236(7) Å. The shortest and longest distances are for the coordinated and non-coordinated amine group of the single coordinated *en* molecule, respectively.

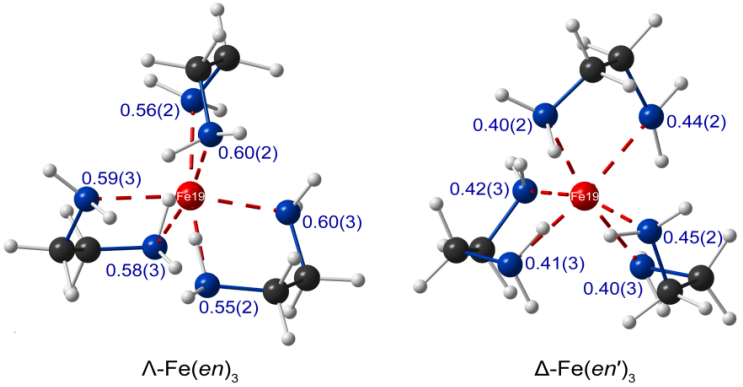

Figure 2-17 Fe(*en*)$_3$ complex of the Fe19 site separated into Λ-Fe(*en*)$_3$ and Δ-Fe(*en*')$_3$ for illustration. Refined site occupation factors of the N and N' atoms are given in blue.

Beside the two complex types, non-coordinating *en* and methanol molecules are located between the Fe_2Se_3 chains [Figure 2-16 E and F]. These are weakly bound to the chains by Se···H-N and Se···H-O hydrogen bonds of 2.535(5)-2.744(6) Å and 2.634(6) Å, respectively. Interestingly, the non-coordinating *en* is also in *gauche* conformation [dihedral angle = 61(4)°], which does not coincide with the *anti* conformation of the non-

coordinating *en* found in $Fe_{10}Se_{12}(en)_7$. Altogether, under consideration of Fe^{2+} oxidation state for all complexes, the formula $[Fe^{2+}{}_8Fe^{3+}{}_8Se^{2-}{}_{24}][Fe^{2+}(en)_3]_4(en)(MeOH)$ is determined for the compound. Therefore, Fe^{2+} and Fe^{3+} in a 1 : 1 ratio are assumed for the Fe_2Se_3 double chains, like for $Fe_{10}Se_{12}(en)_7$.

Figure 2-18 shows the refined powder X-ray diffraction pattern [Mo-$K_{\alpha 1}$ radiation] of a sample of $Fe_{20}Se_{24}(en)_{13}(MeOH)$ synthesized at 200 °C with 20% methanol dilution. The sample contains 41 mol% $Fe_3Se_4(en)_2$, which, under consideration of the significantly different number of atoms per formula unit, corresponds to only 10 wt%. Phase pure synthesis of $Fe_{20}Se_{24}(en)_{13}(MeOH)$ could not be achieved. EDS and elemental analysis, after subtraction of the impurity phase, confirm the stoichiometry obtained by single crystal X-ray diffraction [see appendix A.3].

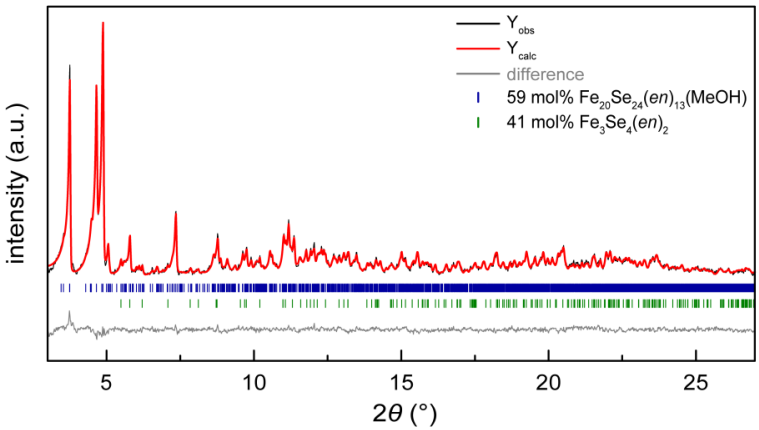

Figure 2-18 Rietveld refinement of the powder X-ray diffraction pattern [Mo-$K_{\alpha 1}$] of a sample of $Fe_{20}Se_{24}(en)_{13}(MeOH)$ [blue positions] containing $Fe_3Se_4(en)_2$ as side phase [green positions].

Phase diagram. As in chapter 2.1 a phase diagram was generated in dependence of the dilution [0-50% MeOH] and the synthesis temperature [180-220 °C]. Figure 2-19 shows the phase ranges based on the main phases of the products obtained from Rietveld refinement of powder X-ray diffraction data [see Table A-19]. Similar to the syntheses with *glycerol* dilution, at high ligand-to-metal ratios [0-10% MeOH] the formation of structures with low degree of condensation, $Fe_3Se_4(en)_3$ and $Fe_3Se_4(en)_2$, is preferred. $Fe_3Se_4(en)_3$ is stable at low temperatures and occurs in both polymorphs with α-$Fe_3Se_4(en)_3$ as majority phase. At 20% and 50% MeOH dilution and low temperatures $Fe_{20}Se_{24}(en)_{13}$(MeOH) is the main product. Since the compound is built up by double chains, an increase in the connectivity of the tetrahedra is observed upon dilution, which is also the case for *glycerol*. In comparison with the phase diagram in Figure 2-6, this phase containing tetrahedra linked *via* three edges is extended over a larger range. $Fe_{0.85}Se(en)_{0.3}$ is obtained at 50% of dilution and for temperatures above 200 °C. Thus, this layered phase is limited to a smaller range for methanol dilution. Overall, despite the different phase ranges, dimensional reduction is observed with increasing ligand-to-metal ratio for both diluents.

In contrast to *glycerol* dilution, phase pure syntheses are hardly achieved by methanol dilution. Beside $Fe_3Se_4(en)_2$ without dilution, a phase pure product is only received for $Fe_{0.85}Se(en)_{0.3}$ at 220 °C and 50% MeOH, whereas $Fe_{20}Se_{24}(en)$(MeOH) could not be obtained without impurity. Significant amounts of side phases [> 15 wt%] are found for almost all samples [indicated in Figure 2-19 as striped areas], which is not the case for *glycerol* dilution. Further, the products do not exclusively contain side phases of adjacent phase ranges. In some samples $Fe_{20}Se_{24}(en)_{13}$(MeOH) and $Fe_{10}Se_{12}(en)_7$ are present simultaneously, which both contain double chains.

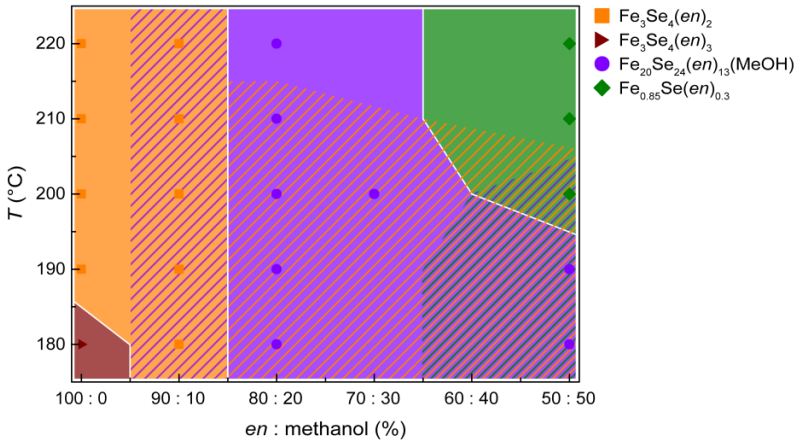

Figure 2-19 Synthetic phase space diagram of the Fe-Se-*en* system in dependence of the dilution of the solvent *en* with methanol and the reaction temperature. Markings show main phases of the obtained products, filled areas indicate phase ranges according to the main product, striped areas indicate ranges with significant side phase.

In summary, the generated phase diagram with methanol shows the equivalent trend for the degree of condensation upon dilution as with *glycerol*. However, chemical control over the products is inferior, which may be attributed to the increased pressure or the changed stability ranges due to the occurrence of the additional phase $Fe_{20}Se_{24}(en)_{13}(MeOH)$.

Pressure measurement. The pressure of mixtures with different degrees of dilution was measured in dependence of the temperature in a high pressure reactor. It must be noted that for this measurements the reaction temperature is determined within the reaction zone, whereas for syntheses in autoclaves used for the phase diagrams, the given values correspond to the set temperatures at the heat block. Since here mainly relative rather than absolute values should be studied, this is sufficient.

Moreover, the pressure measurement is subject to major errors up to $\pm p$ = 1 bar at low pressures, which however should not prevent the comparability of the results. Data was recorded for mixtures with 0%, 20%, 40% and 60% dilution and for temperatures between 150 °C and 190 °C every 5 °C [see Table A-20 and Table A-21]. By linear fitting, the experimental values were extrapolated to higher temperatures and subsequently interpolated to further degrees of dilution.

Figure 2-20 shows the estimated reaction pressure based on the measurements as contour plots for both diluents. As expected, the pressure increases with temperature and decreases with *glycerol* dilution or increases with methanol dilution, respectively. Considering the phase ranges of the different compounds in the Fe-Se-*en* system [given in grey in Figure 2-20], the degree of condensation of the $FeSe_4$ tetrahedra shows no dependence on the pressure. This confirms the dependence of the connectivity on the ligand-to-metal ratio. This is also supported by the fact, that $Fe_{1.04}Se(en)_{0.3}$, with similar layered structure to $Fe_{0.85}Se(en)_{0.3}$, can be solvothermally synthesized without dilution. For this, the ligand-to-metal ratio is decreased by increasing the amount of FeSe and reducing the amount of solvent used.[65] However, the degree of dilution yielding the layered structure still leads to an approximately ten times higher ratio than the approach used in the literature. In the pressure plot with *glycerol* dilution, areas with negligible increase of pressure compared to ambient conditions are observed. These are consistent with the range of amorphous or less crystalline products. Thus, a certain pressure seems to be necessary to stabilize the compounds during solvothermal synthesis.

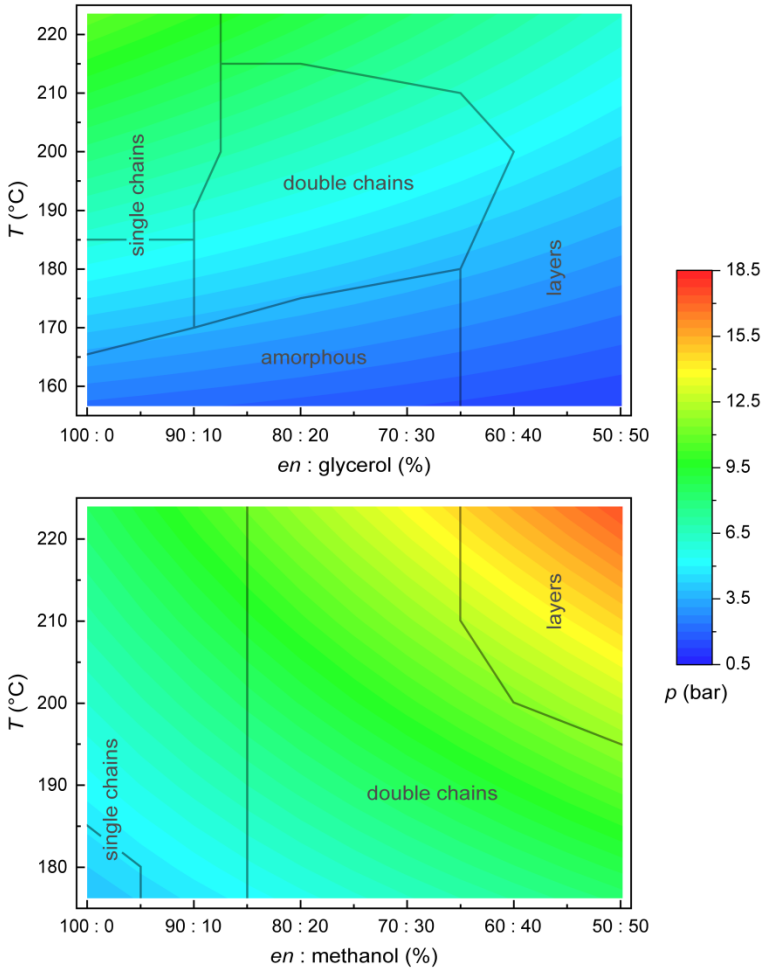

Figure 2-20 Contour plots of the reaction pressure in dependence of temperature and degree of dilution with *glycerol* [top] or methanol [bottom], respectively. Estimated phase ranges for the different connectivity of the $FeSe_4$ tetrahedra are indicated in grey.

Conclusion

Dimensional reduction of the β-FeSe layered structure is possible by solvothermal synthesis by means of dilution with *glycerol* as well as methanol. The effect can be attributed to the reduced ligand-to-metal ratio, as both diluents change the reaction pressure in different ways. Comparison of the phase diagrams in dependence of the temperature of both diluents shows the same trend but different stabilities for the phase ranges of the different terminated fragments. Targeted synthesis of phase pure products is much more difficult for methanol dilution. The cause for this could be the increased pressure along with the potential incorporation of this additional solvent into the structure. The crystal structure of the double chain compound $Fe_{20}Se_{24}(en)_{13}(MeOH)$ shows a great similarity to $Fe_{10}Se_{12}(en)_7$, but contains unique $Fe(en)_3Se$ complexes, which were not found in such structures so far. The use of other diluents could therefore further increase the structural diversity of dimensionally reduced β-FeSe-related compounds.

2.3 References

1 T. Li and J. E. Goldberger, *Chem. Mater.* **2015**, *27*, 3549-3559.

2 R. A. L. Morasse, T. Li, Z. J. Baum and J. E. Goldberger, *Chem. Mater.* **2014**, *26*, 4776-4780.

3 E. G. Tulsky and J. R. Long, *Chem. Mater.* **2001**, *13*, 1149-1166.

4 C. Pak, S. Kamali, J. Pham, K. Lee, J. T. Greenfield and K. Kovnir, *J. Am. Chem. Soc.* **2013**, *135*, 19111-19114.

5 J. T. Greenfield, C. Pak, S. Kamali, K. Lee and K. Kovnir, *Chem. Commun.* **2015**, *51*, 5355-5358.

6 X. Huang and J. Li, *J. Am. Chem. Soc.* **2007**, *129*, 3157-3162.

7 H. Boller and H. Blaha, *J. Solid State Chem.* **1982**, *45*, 119-126.

8 Y.-H. Liu, S. H. Porter and J. E. Goldberger, *J. Am. Chem. Soc.* **2012**, *134*, 5044-5047.

9 P. Vaqueiro, *Inorg. Chem.* **2006**, *45*, 4150-4156.

10 TOPAS-Academic, V5, Coelho Software, Brisbane, Australia, **2007**.

11 V. Petříček, M. Dušek and L. Palatinus, *Z. Kristallogr. - Cryst. Mater.* **2014**, *229*, 345-352.

12 M. S. Jhon, U.-L. Cho, L. B. Kier and H. Eyring, *PNAS USA* **1972**, *69*, 121-123.

13 C. Koz, M. Schmidt, H. Borrmann, U. Burkhardt, S. Rößler, W. Carrillo-Cabrera, W. Schnelle, U. Schwarz and Y. Grin, *Z. Anorg. Allg. Chem.* **2014**, *640*, 1600-1606.

14 H. Y. Hong and H. Steinfink, *J. Solid State Chem.* **1972**, *5*, 93-104.

15 T. Hatakeda, T. Noji, S. Hosono, T. Kawamata, M. Kato and Y. Koike, *JPCS* **2014**, *568*, 022032.

16 T. Noji, T. Hatakeda, S. Hosono, T. Kawamata, M. Kato and Y. Koike, *Physica C* **2014**, *504*, 8-11.

17 T. Hatakeda, T. Noji, T. Kawamata, M. Kato and Y. Koike, *J. Phys. Soc. Jpn.* **2013**, *82*, 123705.

18 N. M. Norlidah, G. Venturini and B. Malaman, *J. Alloys Compd.* **1998**, *268*, 193-198.

19 F.-C. Hsu, J.-Y. Luo, K.-W. Yeh, T.-K. Chen, T.-W. Huang, P. M. Wu, Y.-C. Lee, Y.-L. Huang, Y.-Y. Chu, D.-C. Yan and M.-K. Wu, *PNAS USA* **2008**, *105*, 14262-14264.

20 R. J. E. Lees, A. V. Powell and A. M. Chippindale, *Polyhedron* **2005**, *24*, 1941-1948.

21 Z. Chen, R.-J. Wang, X.-Y. Huang and J. Li, *Acta Crystallogr. Sect. C: Cryst. Struct. Commun.* **2000**, *56*, 1100-1103.

22 G. A. Renovitch and W. A. Baker, *J. Am. Chem. Soc.* **1968**, *90*, 3585-3587.

23 W. M. Reiff, *Chem. Phys. Lett.* **1971**, *8*, 297-299.

24 J. Li, Z. Chen, R.-J. Wang and D. M. Proserpio, *Coord. Chem. Rev.* **1999**, *190-192*, 707-735.

25 H. V. Phan, P. Chakraborty, M. Chen, Y. M. Calm, K. Kovnir, L. K. Keniley, J. M. Hoyt, E. S. Knowles, C. Besnard, M. W. Meisel, A. Hauser, C. Achim and M. Shatruk, *Chem. Eur. J.* **2012**, *18*, 15805-15815.

26 Y. Nishida, K. Kino and S. Kida, *J. Chem. Soc., Dalton Trans.* **1987**, 1157-1161.

27 W. Bronger, A. Kyas and P. Müller, *J. Solid State Chem.* **1987**, *70*, 262-270.

28 H. Lei, H. Ryu, A. I. Frenkel and C. Petrovic, *Phys. Rev. B: Condens. Matter* **2011**, *84*, 214511.

29 J. M. Caron, J. R. Neilson, D. C. Miller, A. Llobet and T. M. McQueen, *Phys. Rev. B: Condens. Matter* **2011**, *84*, 180409.

30 J. M. Caron, J. R. Neilson, D. C. Miller, K. Arpino, A. Llobet and T. M. McQueen, *Phys. Rev. B: Condens. Matter* **2012**, *85*, 180405.

31 K. O. Klepp, W. Sparlinek and H. Boller, *J. Alloys Compd.* **1996**, *238*, 1-5.

32 L. F. Bates, *Modern Magnetism*, Cambridge University Press, **1948**.

33 T. M. McQueen, Q. Huang, V. Ksenofontov, C. Felser, Q. Xu, H. Zandbergen, Y. S. Hor, J. Allred, A. J. Williams, D. Qu, J. Checkelsky, N. P. Ong and R. J. Cava, *Phys. Rev. B: Condens. Matter* **2009**, *79*, 014522.

34 F. Hayashi, H. Lei, J. Guo and H. Hosono, *Inorg. Chem.* **2015**, *54*, 3346-3351.

35 S. Jin, X. Fan, X. Wu, R. Sun, H. Wu, Q. Huang, C. Shi, X. Xi, Z. Li and X. Chen, *Chem. Commun.* **2017**, *53*, 9729-9732.

36 J. Rouxel, in *Organic and Inorganic Low-Dimensional Crystalline Materials*, Springer, New York, **1987**, 1-16.

37 Z. Guo, F. Sun and W. Yuan, *Cryst. Growth Des.* **2017**, *17*, 2238-2253.

38 W. Bronger, *Z. Anorg. Allg. Chem.* **1968**, *359*, 225-233.

39 J. Stahl, E. Shlaen, H. Singer and D. Johrendt, *Dalton Trans.* **2018**, *47*, 3264-3271.

40 A. Eichhöfer, G. Buth, F. Dolci, K. Fink, R. A. Mole and P. T. Wood, *Dalton Trans.* **2011**, *40*, 7022-7032.

41 Q.-Y. Wang, Z. Li, W.-H. Zhang, Z.-C. Zhang, J.-S. Zhang, W. Li, H. Ding, Y.-B. Ou, P. Deng, K. Chang, J. Wen, C.-L. Song, K. He, J.-F. Jia, S.-H. Ji, Y.-Y. Wang, L.-L. Wang, X. Chen, X.-C. Ma and Q.-K. Xue, *Chin. Phys. Lett.* **2012**, *29*, 037402.

42 S. He, J. He, W. Zhang, L. Zhao, D. Liu, X. Liu, D. Mou, Y.-B. Ou, Q.-Y. Wang, Z. Li, L. Wang, Y. Peng, Y. Liu, C. Chen, L. Yu, G. Liu, X. Dong, J. Zhang, C. Chen, Z. Xu, X. Chen, X. Ma, Q. Xue and X. J. Zhou, *Nat. Mater.* **2013**, *12*, 605-610.

43 J.-F. Ge, Z.-L. Liu, C. Liu, C.-L. Gao, D. Qian, Q.-K. Xue, Y. Liu and J.-F. Jia, *Nat. Mater.* **2014**, *14*, 285-289.

44 I. I. Mazin, *Nat. Mater.* **2015**, *14*, 755-756.

45 B. Li, Z. W. Xing, G. Q. Huang and D. Y. Xing, *J. Appl. Phys.* **2014**, *115*, 193907.

46 C.-L. Song, Y.-L. Wang, Y.-P. Jiang, Z. Li, L. Wang, K. He, X. Chen, X.-C. Ma and Q.-K. Xue, *Phys. Rev. B: Condens. Matter* **2011**, *84*, 020503.

47 Y. Miyata, K. Nakayama, K. Sugawara, T. Sato and T. Takahashi, *Nat. Mater.* **2015**, *14*, 775-779.

48 J. Guo, S. Jin, G. Wang, S. Wang, K. Zhu, T. Zhou, M. He and X. Chen, *Phys. Rev. B: Condens. Matter* **2010**, *82*, 180520.

49 E. Dagotto, *Rev. Mod. Phys.* **2013**, *85*, 849-867.

50 M. Burrard-Lucas, D. G. Free, S. J. Sedlmaier, J. D. Wright, S. J. Cassidy, Y. Hara, A. J. Corkett, T. Lancaster, P. J. Baker, S. J. Blundell and S. J. Clarke, *Nat. Mater.* **2012**, *12*, 15-19.

51 S. J. Sedlmaier, S. J. Cassidy, R. G. Morris, M. Drakopoulos, C. Reinhard, S. J. Moorhouse, D. O'Hare, P. Manuel, D. Khalyavin and S. J. Clarke, *J. Am. Chem. Soc.* **2014**, *136*, 630-633.

52 A. E. Böhmer, V. Taufour, W. E. Straszheim, T. Wolf and P. C. Canfield, *Phys. Rev. B: Condens. Matter* **2016**, *94*, 024526.

53 SmartSEM, 5.07 Beta, Carl Zeiss Microscopy Ltd., Cambridge, UK, **2014**.

54 QUANTAX 200, 1.9.4.3448, Bruker Nano GmbH, Berlin, Germany, **2013**.

55 P. Terzieff and K. L. Komarek, *Monatsh. Chem.* **1978**, *109*, 1037-1047.

56 S. Li, S. F. Jin, J. Ji, Z. N. Guo and W. X. Yuan, *Powder Diffr.* **2013**, *28*, S32-S36.

57 E. Pomjakushina, K. Conder, V. Pomjakushin, M. Bendele and R. Khasanov, *Phys. Rev. B: Condens. Matter* **2009**, *80*, 024517.

58 A. J. Williams, T. M. McQueen and R. J. Cava, *Solid State Commun.* **2009**, *149*, 1507-1509.

59 T.-K. Chen, C.-C. Chang, H.-H. Chang, A.-H. Fang, C.-H. Wang, W.-H. Chao, C.-M. Tseng, Y.-C. Lee, Y.-R. Wu, M.-H. Wen, H.-Y. Tang, F.-R. Chen, M.-J. Wang, M.-K. Wu and D. Van Dyck, *PNAS USA* **2014**, *111*, 63-68.

60 F. Ye, S. Chi, W. Bao, X. F. Wang, J. J. Ying, X. H. Chen, H. D. Wang, C. H. Dong and M. Fang, *Phys. Rev. Lett.* **2011**, *107*, 137003.

61 Z. Wang, Y. J. Song, H. L. Shi, Z. W. Wang, Z. Chen, H. F. Tian, G. F. Chen, J. G. Guo, H. X. Yang and J. Q. Li, *Phys. Rev. B: Condens. Matter* **2011**, *83*, 140505.

62 S. Hosono, T. Noji, T. Hatakeda, T. Kawamata, M. Kato and Y. Koike, *J. Phys. Soc. Jpn.* **2014**, *83*, 113704.

63 S. Hosono, T. Noji, T. Hatakeda, T. Kawamata, M. Kato and Y. Koike, *J. Phys. Soc. Jpn.* **2015**, *85*, 013702.

64 S. Hosono, T. Noji, T. Hatakeda, T. Kawamata, M. Kato and Y. Koike, *J. Phys. Soc. Jpn.* **2016**, *85*, 104701.

65 Z. Gao, S. Zeng, B. Zhu, B. Li, Q. Hao, Y. Hu, D. Wang and K. Tang, *Sci. China Mater.* **2018**, *61*, 977-984.

66 G. Demazeau, *J. Mater. Sci.* **2008**, *43*, 2104-2114.

67 R. I. Walton, *Chem. Soc. Rev.* **2002**, *31*, 230-238.

68 M. H. de Senarmont, *Ann. de Chim. et de Phys.* **1851**, *32*, 129-175.

69 A. Rabenau, *Angew. Chem. Int. Ed. Engl.* **1985**, *24*, 1026-1040.

70 A. Richardson, *J. Chem. Soc., Trans.* **1886**, *49*, 761-776.

71 W. Hieber and A. Woerner, *Z. Elektrochem. angew. phys. Chem.* **1934**, *40*, 252-256.

72 D. Ambrose and C. H. S. Sprake, *J. Chem. Thermodyn.* **1970**, *2*, 631-645.

73 P. Venkateswarlu and W. Gordy, *J. Chem. Phys.* **1955**, *23*, 1200-1202.

3 β-FeSe by vapor-transport, solvothermal and hydrothermal synthesis – Structural, chemical and superconducting properties and their dependencies

Abstract

Samples of the iron based superconductor β-FeSe are prepared *via* vapor-transport growth, solvothermal and hydrothermal synthesis. Despite equal room temperature structures and similar stoichiometries, all three exhibit different behavior at low temperatures. Identical measurements of the properties are conducted for the three samples to ensure the exclusion of systematic errors. The dependencies between the structural transition, the composition and the occurrence of superconductivity are discussed based on the results.

Introduction

Since the discovery of iron based superconductors in 2008, the nature of the superconducting phase and especially the pairing mechanism have been controversially discussed. The superconducting state may be either induced by phonon interactions or mediated by charge or spin fluctuations.[1] At early stages a magnetically driven transition was postulated, since most iron based superconductors exhibit an antiferromagnetic order upon cooling.[1,2] If this order is suppressed by electron- or hole-doping or external pressure, the superconducting state emerges.[3] However, β-FeSe can only be mentioned as one example where such ordering does not occur.[4] With a nematic phase yet another ordered state is found

for iron based superconductors, which is also present in β-FeSe.[5,6] This ordering lowers the rotational symmetry as well, and can occur isolated, simultaneously or prior to the antiferromagnetic transition, depending on the material.[1] The tetragonal-to-orthorhombic phase transition, common to most iron based superconductors, is associated with the nematic ordering.[1,7,8] β-FeSe, as the simplest compound in structural terms, has been extensively studied to observe relations between the different ordering phenomena.[8] Still, the understanding of the driving force of the structural and superconducting transition and the interplay of phonon, charge and spin fluctuations is lacking.

β-FeSe represents an exceptional case among iron based superconductors, not only due to its structural simplicity, but also due to the emergence of superconductivity below 8 K without additional doping.[4] External or chemical pressure enhances T_c without changing the layered structure of the superconducting phase. Thus, transition temperatures of 37 K at a hydrostatic pressure of 7 GPa or 15 K for $FeSe_{0.75}Te_{0.25}$ and $FeSe_{0.8}S_{0.2}$ can be achieved.[9,10] It is therefore conceivable that intrinsic electronic doping also causes the superconductivity in stoichiometric β-FeSe through iron atoms occupying interstitial positions between the layers. Interstitial iron and selenium vacancies have both been observed for the layered structure.[11-13] Hence, so far several studies addressed the precise investigation of the superconducting transition in dependency on the stoichiometry.[12-14] Such experiments are however impeded due to the narrow stability range of β-FeSe in the binary phase diagram.[15] This largely prevents phase pure samples through solid state synthesis, which mostly contain elemental Fe, hexagonal δ-FeSe or Fe_3O_4 impurities.[12,13] Magnetic ordering of these side phases can interfere with the nematic and superconducting fluctuations in β-FeSe and hinder corresponding measurements. Multiple alternative synthesis methods have therefore

been developed to overcome these difficulties, including flux and transport growth or solution-based syntheses, either from precursors or under solvothermal conditions.[16-25] Especially the products from solution-based routes often lack the transition to a superconducting state, which mostly is attributed to oxygen contamination.[24,25] Accordingly, for the determination of the interdependencies of structural, chemical and physical parameters of *β*-FeSe, samples must be thoroughly characterized with respect to the overall properties.

In this chapter, samples of *β*-FeSe are produced *via* three different routes, by vapor-transport growth, by solvothermal synthesis in a mixture of *1,3-dap* and *glycerol* and by hydrothermal synthesis.[18,23] The samples are referred to as $FeSe_{trans}$, $FeSe_{solvo}$ and $FeSe_{hydro}$ in the following. The compounds are investigated with regard to their room temperature crystal structure and stoichiometry, whereby despite the different synthesis methods only minor differences emerge. Measurements at low temperatures, however, show distinctly different behavior of the samples, with respect to the structural phase transition and the magnetic properties. Thereby, $FeSe_{solvo}$ partially exhibits superconductivity while no tetragonal-to-orthorhombic phase transition is detected.

Experimental

For synthesis of $FeSe_{trans}$ 437.6 mg Fe powder [Chempur, 99.9%] and 562.4 mg Se powder [Chempur, 99.999%] in 1.1 : 1 molar ratio were weighed together with 7.75 g $AlCl_3$ [Alfa Aesar, 99.985%] and 2.25 g KCl [Grüssing, 99.5%, dried].[18] The transport was carried out under vacuum in a glass ampoule [height 4 cm, diameter 5 cm] with 390 °C at the bottom and about 280 °C at the top. After 12 days, the crystals grown at the

top were washed with water, ethanol and acetone and dried under vacuum at room temperature.

$FeSe_{solvo}$ was synthesized in a Teflon-lined steel autoclave with total volume of 50 mL. 20.7 mg Fe powder [Chempur, 99.9%] and 29.3 mg Se powder [Chempur, 99.999%] in 1 : 1 molar ratio were used as starting material. To improve the crystallinity of the product 100 mg of NH_4Cl [Kraft, purissimum] were added. The solvent was a mixture of 28 mL propane-1,3-diamine [*1,3-dap*, Merck, ≥ 99%] and 7 mL propane-1,2,3-triol [*glycerol*, Grüssing, 99%], which corresponds to a ratio of 80% : 20% and a filling fraction of the autoclave of 70%. The synthesis was carried out at 200 °C for 12 days. The product was washed with water, ethanol and acetone and dried under vacuum at room temperature.

Based on hydrothermal synthesis described in the literature, $FeSe_{hydro}$ was produced in a Teflon-lined steel autoclave [50 mL total volume].[23] 55.9 mg Fe powder [Chempur, 99.9%] and 94.8 mg Se powder [Chempur, 99.999%] corresponding a molar ratio of 1 : 1.2, together with 500 mg KOH [ApliChem] as mineralizer and 300 mg $NaBH_4$ [Acros, 98%] as reducing agent, were mixed with 20 mL water. The reaction was conducted at 155 °C for 32 days. The product was washed with water and ethanol. After drying under vacuum at room temperature, magnetic impurities were removed with a magnet.

Characterization of the samples was done *via* powder X-ray diffraction on a Stoe Stadi P diffractometer [Mo $K_{\alpha1}$ radiation; Ge 111 monochromator]. Low temperature powder patterns were recorded on a Huber G670 diffractometer [Co-$K_{\alpha1}$ radiation; Ge-111 monochromator; Low Temperature Device 670.4; closed cycle He cryostat] between 20 K and

300 K. Rietveld refinements were done using TOPAS package.[26] The Fe : Se ratio was determined *via* EDS measurements on a Zeiss Evo-Ma10 microscope with Bruker X-Flash 410-M detector and *via* ICP-OES analysis on a Varian Vista RL spectrometer. Magnetic measurements were carried out on a PPMS with a VSM option.

Results and Discussion

Crystal structure and phase transition. The Rietveld refinements of powder X-ray diffraction data [Mo-$K_{\alpha 1}$ radiation] at room temperature are shown in Figure 3-1 for $FeSe_{trans}$, $FeSe_{solvo}$ and $FeSe_{hydro}$. The refinements are in good agreement with the measured data and no impurity phases are observed within the limits of the method [≈ 1 wt%]. The powder pattern of $FeSe_{trans}$ shows a slightly increased noise pattern and a few deviating intensity ratios compared to the other two samples. This is attributed to the strong preferred orientation of the crystals, which exhibit a pronounced plate-like shape due to the crystal growth by vapor-transport. The resulting lattice parameters from Rietveld refinement are given in Table 3-1. The differences between the samples are very small, with $\Delta_{max}a = 0.19\%$ and $\Delta_{max}c = 0.15\%$. The lattice parameters of $FeSe_{trans}$ are comparable to those found in the literature for similarly prepared samples with $a_{lit} = 3.7707$ Å and $c_{lit} = 5.521$ Å [Δa, $\Delta c \leq 0.05\%$].[17] The synthesis of $FeSe_{hydro}$ was slightly modified, but the lattice parameters nevertheless hardly differ from the literature values $a_{lit} = 3.7711$ Å and $c_{lit} = 5.5214$ Å [Δa, $\Delta c = 0.1\%$].[23] Moreover, compared to FeSe produced by conventional solid state synthesis [$a_{lit} = 3.7734$ Å, $c_{lit} = 5.5258$ Å], the lattice parameters of all three samples show almost no deviation with $\Delta_{max}a = 0.14\%$ and $\Delta_{max}c = 0.18\%$.[12]

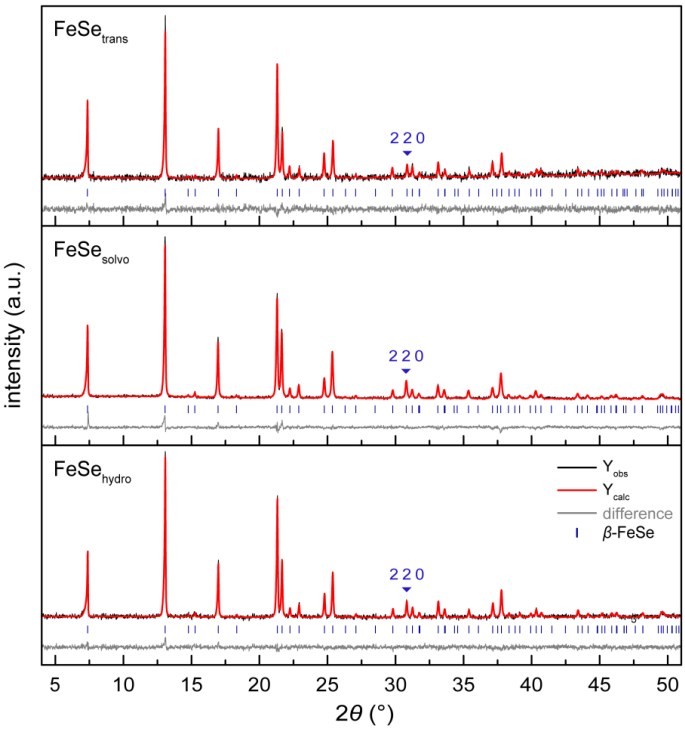

Figure 3-1 Rietveld refinement of powder X-ray diffraction patterns [Mo-$K_{\alpha1}$] of $FeSe_{trans}$ [top], $FeSe_{solvo}$ [middle] and $FeSe_{hydro}$ [bottom]. The 220 reflection is marked in blue.

The z coordinates of the Se atom are also determined from the Rietveld refinements and are given in Table 3-1. The maximum deviation within the samples is 1.2% with the largest value for $FeSe_{trans}$ and smallest value for $FeSe_{solvo}$. Compared to the literature $\Delta_{max}z$ is 1.0% with z_{lit} = 0.2667 for transport grown samples and z_{lit} = 0.2672 for samples from hydrothermal and solid state synthesis, respectively.[12,17,23] Refinement of the occupation of the Fe site yielded comparable results for all three samples as well [Fe : Se ratios given in Table 3-1], indicating 1 : 1 stoichiometry.

Overall, no significant differences in the room temperature structures of $FeSe_{trans}$, $FeSe_{solvo}$ and $FeSe_{hydro}$ are evident from powder X-ray diffraction analyses, even in comparison with the literature.

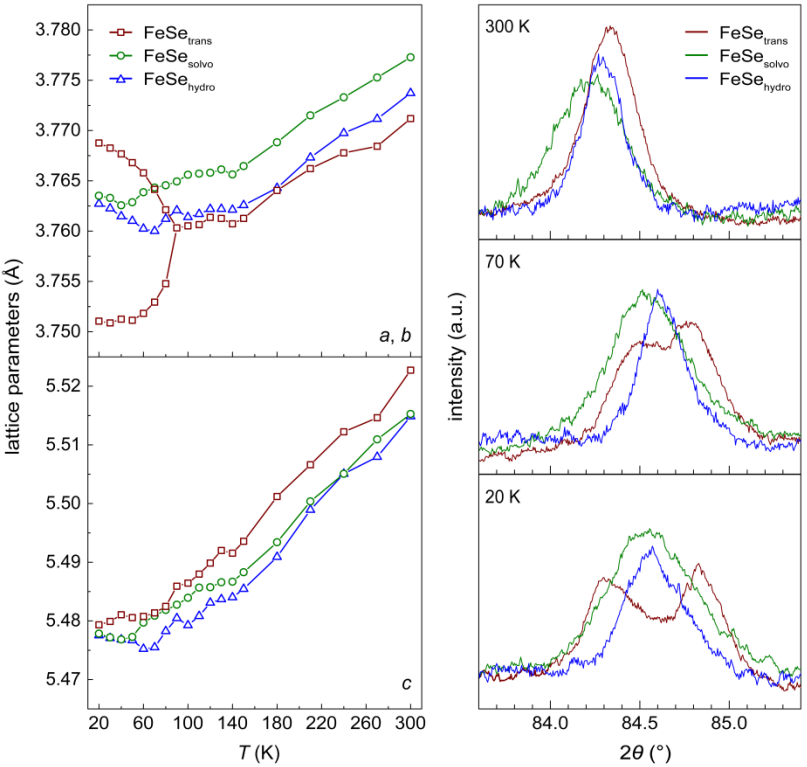

Figure 3-2 Lattice parameters between 20 K and 300 [left] and 220 reflection at 300 K, 70 K and 20 K [right] for $FeSe_{trans}$ [red], $FeSe_{solvo}$ [green] and $FeSe_{hydro}$ [blue]. *a* and *b* parameters of $FeSe_{trans}$ are divided by √2 below the phase transition.

The structural changes upon cooling are investigated by powder X-ray diffraction [Co-$K_{\alpha 1}$ radiation] and subsequent Rietveld refinement. The

resulting lattice parameters are displayed in Figure 3-2 [left] between 20 K and 300 K. $FeSe_{trans}$ exhibits a phase transition from tetragonal [space group *P*4/*nmm*] to orthorhombic symmetry [space group *Cmme*] below 90 K, which is in line with samples produced by vapor-transport or solid state synthesis in the literature.[17,27] The transition can best be observed in the X-ray diffraction data based on the splitting of the 220 reflection of the tetragonal structure [marked in Figure 3-1]. Figure 3-2 [right] shows the corresponding excerpts of the powder patterns for all three samples at different temperatures. Since $FeSe_{solvo}$ and $FeSe_{hydro}$ indicate no splitting, the compounds are considered tetragonal down to 20 K. Similar findings exist for some FeSe samples from solid state synthesis.[28] For these, the absence of the transition is ascribed to an increased iron content and the emergence of a structural modulation. For hydrothermally produced samples, a tetragonal-to-triclinic transition was observed based on the asymmetric splitting of the 220 reflection below 60 K.[23] The synthesis conditions of the $FeSe_{hydro}$ sample presented here only slightly differ in the Fe : Se molar ratio and the amount of mineralizer compared to the literature. However, the synthesis temperature is increased from 150 °C to 155 °C and the reaction time is almost tripled, which is considered more decisive for the deviant behavior. Overall, the differences show that even small changes in the hydrothermal synthesis can strongly influence the physical properties of the samples. $FeSe_{hydro}$ additionally shows an anomaly at low temperatures, since the lattice parameters increase below 60 K. However, the variation is below 0.1%. It should also be noted, that samples without structural phase transition are non-superconducting according to the literature.[28] This does not apply to $FeSe_{solvo}$ presented here, which exhibits no structural transition, but is superconducting below 8 K [see below].

Composition. There is disagreement in the literature in which way the exact stoichiometry affects the superconductivity of β-FeSe.[12,13,18] For samples from solid state synthesis a decrease of T_c was observed from 8.5 K in $Fe_{1.01}Se$ to 5 K in $Fe_{1.02}Se$, while in $Fe_{1.03}Se$ no superconducting transition was detected.[12] Transport grown samples, however, exhibited identical stoichiometry of $Fe_{1.03}Se$, but different transition temperatures of 8.7-8.8 K or < 5 K, depending on the synthesis conditions.[18] In this case, the superconductivity was assumed to be strongly dependent on structural disorder. The compositions of the three samples $FeSe_{trans}$, $FeSe_{solvo}$ and $FeSe_{hydro}$ were determined by ICP-OES and EDS analyses. The Fe : Se ratios are given in Table 3-1. Both methods reveal the same trend with lowest ratio for $FeSe_{trans}$ and highest ratio for $FeSe_{hydro}$. Since EDS measurements exhibit a larger systematic error, the results from ICP analysis are considered more accurate. Therefore, $FeSe_{trans}$ and $FeSe_{solvo}$ are almost stoichiometric and barely distinguishable, while $FeSe_{hydro}$ shows enhanced iron content. This coincides with the former being superconducting and $FeSe_{hydro}$ being non-superconducting [see below]. It should be noted, that the analyses give no indication whether excess Fe on interstitial positions or Se vacancies are present. In the literature, the c/a ratio was therefore postulated as an indirect estimate of the stoichiometry.[12] For samples from solid state reactions it is has been demonstrated that the ratio initially increases slightly with increasing Fe content [$c/a \approx 1.464$-1.466], followed by a sharp drop [$c/a \approx 1.461$]. This is associated with decreasing Se vacancies and increasing Fe interstitials, respectively. The ratio is also considered to be closely linked to T_c with highest temperatures at $c/a = 1.464$ and reduced temperatures at larger ratios. For $c/a \approx 1.461$ and a high iron content, no superconductivity was detected. The c/a ratios of $FeSe_{trans}$, $FeSe_{solvo}$ and $FeSe_{hydro}$ are given in Table 3-1. The value for $FeSe_{trans}$ is in the range of a low Fe : Se ratio and

a high T_c. This is in line with the results from magnetic measurements [see below]. $FeSe_{solvo}$ and $FeSe_{hydro}$ both exhibit very small c/a ratios, which would indicate an increased amount of interstitial Fe and a non-superconducting behavior. This is consistent with the chemical analysis and magnetic measurements for $FeSe_{hydro}$, but contradicts the findings for $FeSe_{solvo}$.

Table 3-1 Lattice parameters, c/a ratios and Se positions from Rietveld refinement of powder X-ray diffraction data [Mo-$K_{\alpha1}$] at room temperature, composition from EDS and ICP analyses and superconducting transition temperatures for the $FeSe_{trans}$, $FeSe_{solvo}$ and $FeSe_{hydro}$ samples.

	$FeSe_{trans}$	**$FeSe_{solvo}$**	**$FeSe_{hydro}$**
a (Å)	3.7717(2)	3.7788(1)	3.7750(2)
c (Å)	5.5239(5)	5.5182(3)	5.5156(3)
c/a ratio	1.4646(1)	1.4603(1)	1.4611(1)
z(Se)	0.2677(7)	0.2661(4)	0.2645(5)
Fe : Se from PXRD	0.97(1) : 1	0.98(1) : 1	0.97(1) : 1
Fe : Se from ICP	0.99(1) : 1	1.00(1) : 1	1.07(1) : 1
Fe : Se from EDS	1.12(12) : 1	1.14(13) : 1	1.16(8) : 1
T_c (K)	8.9	6.9	-

Magnetic measurements. Figure 3-3 shows the isothermal magnetization curves at 1.8 K and the zfc/fc susceptibilities at 50 Oe for $FeSe_{trans}$, $FeSe_{solvo}$ and $FeSe_{hydro}$. $FeSe_{trans}$ exhibits a superconducting transition at 8.9 K. The increased superconducting volume fraction of about 160% at

1.8 K is ascribed to the distinct plate-like crystal shape [demagnetization effect]. Overall, the results are in accordance with vapor-grown samples in the literature.[17]

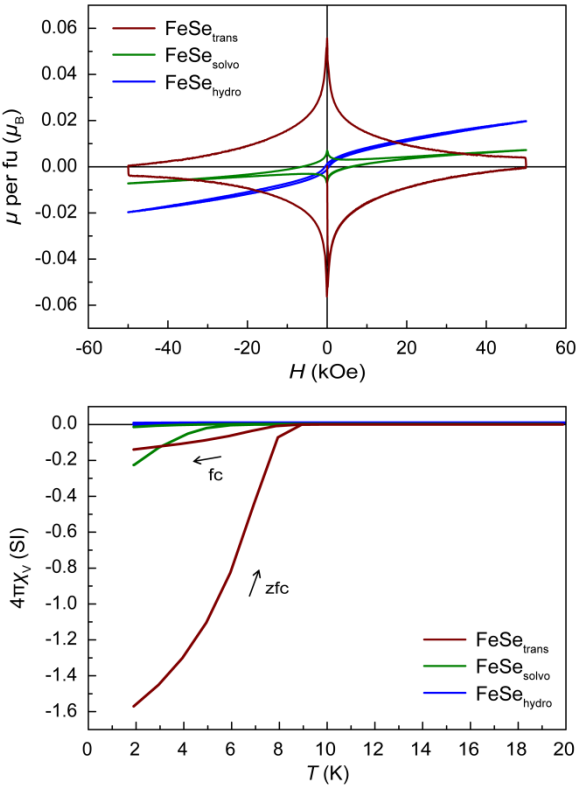

Figure 3-3 Isothermal magnetizations per formula unit at 1.8 K [top] and zero-field-cooled (zfc)/field-cooled (fc) measurements at 50 Oe [bottom] for $FeSe_{trans}$ [red], $FeSe_{solvo}$ [green] and $FeSe_{hydro}$ [blue].

$FeSe_{solvo}$ is also superconducting, but with lowered T_c of 6.9 K and volume fraction of about 23% [see Figure 3-3 bottom]. Since the sample

contains only β-FeSe according to the X-ray diffraction data, the small volume fraction might suggest a separation into a superconducting and a non-superconducting phase. The shape of the isothermal magnetization curve also indicates a presumably paramagnetic impurity [Figure 3-3 top]. Taking into account the low-temperature X-ray diffraction data, the lack of the tetragonal-to-orthorhombic phase transition may apply only for the non-superconducting phase, which would be in accordance with the literature.[28] The smaller, superconducting phase [≈ 25% considering the superconducting volume fraction] could still exhibit a structural phase transition, with the splitting of the reflections concealed by the larger tetragonal phase. This is conceivable, since the reflections of the $FeSe_{solvo}$ sample are broadened due to the small crystal size [see Figure 3-2 right]. A Rietveld refinement of the low-temperature data [10 K] with both phases, however, was not possible. An electronic phase separation with coexistence of magnetism and superconductivity could therefore be considered as well. Both scenarios are discussed for alkali metal intercalated FeSe, for example.[29]

$FeSe_{hydro}$ exhibits no magnetic ordering, but the small hysteresis of the isothermal magnetization curve indicates a ferromagnetic impurity. FeSe samples produced from precursors by solution-based reactions show similar results and a possible antiferromagnetic ordering of FeSe itself is discussed [T_N = 50-60 K].[20,21,24] Solvothermally synthesized samples in ethane-1,2-diol [*ethylene glycol*] with elemental Fe and Se used as starting materials reveal comparable features when exposed to air and water during synthesis or postsynthetic.[25] Exclusion of the exposition yields superconducting samples with T_c = 8 K. The suppression of the superconducting transition in solution-produced FeSe is therefore attributed to oxygen incorporated into the structure. A similar explanation may also apply for the lack of superconductivity in the hydrothermally produced

samples. However, the sample $FeSe_{hydro}$ presented here and the comparable sample in the literature deviate from the oxygen-containing samples in their lattice parameters. Moreover, no oxygen was detected by chemical analyses above the error limit.

Conclusions

In this chapter three β-FeSe samples were successfully synthesized using different alternatives to the conventional solid state method. Beside the literature known transport-growth technique [$FeSe_{trans}$] and hydrothermal method [$FeSe_{hydro}$], a novel solvothermal approach with a mixture of *1,3-dap* and *glycerol* reliably yielded phase pure samples [$FeSe_{solvo}$]. Determination of dependencies on various properties were therefore possible by using exactly the same analyses for all three samples. Comparison of the room temperature crystal structures showed only slight differences, while only for $FeSe_{trans}$ the tetragonal-to-orthorhombic phase transition was observed at low temperatures. The transition is assumed to indicate a nematic order, so it seems remarkable that $FeSe_{solvo}$ nevertheless exhibits superconductivity. Further investigations should also address a possible phase separation in this sample. Measurements of the composition do not contradict the previous findings that 1 : 1 stoichiometry is decisive for superconductivity. The absence of superconductivity in $FeSe_{hydro}$ may be attributed to oxygen incorporation. Compared to the literature, this sample especially demonstrates that minor changes of the synthesis route can develop great impact on individual properties of β-FeSe.

3.1 References

1 R. M. Fernandes, A. V. Chubukov and J. Schmalian, *Nat. Phys.* **2014**, *10*, 97-104.

2 J. Paglione and R. L. Greene, *Nat. Phys.* **2010**, *6*, 645-658.

3 D. Johrendt, *J. Mater. Chem.* **2011**, *21*, 13726-13736.

4 F.-C. Hsu, J.-Y. Luo, K.-W. Yeh, T.-K. Chen, T.-W. Huang, P. M. Wu, Y.-C. Lee, Y.-L. Huang, Y.-Y. Chu, D.-C. Yan and M.-K. Wu, *PNAS USA* **2008**, *105*, 14262-14264.

5 M. A. Tanatar, A. E. Böhmer, E. I. Timmons, M. Schütt, G. Drachuck, V. Taufour, K. Kothapalli, A. Kreyssig, S. L. Bud'ko, P. C. Canfield, R. M. Fernandes and R. Prozorov, *Phys. Rev. Lett.* **2016**, *117*, 127001.

6 S. H. Baek, D. V. Efremov, J. M. Ok, J. S. Kim, J. van den Brink and B. Büchner, *Nat. Mater.* **2014**, *14*, 210-214.

7 J. Li, P. J. Pereira, J. Yuan, Y.-Y. Lv, M.-P. Jiang, D. Lu, Z.-Q. Lin, Y.-J. Liu, J.-F. Wang, L. Li, X. Ke, G. Van Tendeloo, M.-Y. Li, H.-L. Feng, T. Hatano, H.-B. Wang, P.-H. Wu, K. Yamaura, E. Takayama-Muromachi, J. Vanacken, L. F. Chibotaru and V. V. Moshchalkov, *Nat. Commun.* **2017**, *8*, 1880.

8 A. E. Böhmer and A. Kreisel, *J. Phys.: Condens. Matter* **2018**, *30*, 023001.

9 S. Margadonna, Y. Takabayashi, Y. Ohishi, Y. Mizuguchi, Y. Takano, T. Kagayama, T. Nakagawa, M. Takata and K. Prassides, *Phys. Rev. B: Condens. Matter* **2009**, *80*, 064506.

10 Y. Mizuguchi, F. Tomioka, S. Tsuda, T. Yamaguchi and Y. Takano, *J. Phys. Soc. Jpn.* **2009**, *78*, 074712.

11 T. Tsuji, A. T. Howe and N. N. Greenwood, *J. Solid State Chem.* **1976**, *17*, 157-163.

12 T. M. McQueen, Q. Huang, V. Ksenofontov, C. Felser, Q. Xu, H. Zandbergen, Y. S. Hor, J. Allred, A. J. Williams, D. Qu, J. Checkelsky, N. P. Ong and R. J. Cava, *Phys. Rev. B: Condens. Matter* **2009**, *79*, 014522.

13 A. J. Williams, T. M. McQueen and R. J. Cava, *Solid State Commun.* **2009**, *149*, 1507-1509.

14 E. Pomjakushina, K. Conder, V. Pomjakushin, M. Bendele and R. Khasanov, *Phys. Rev. B: Condens. Matter* **2009**, *80*, 024517.

15 W. Schuster, H. Mikler and K. L. Komarek, *Monatsh. Chem.* **1979**, *110*, 1153-1170.

16 D. Chareev, E. Osadchii, T. Kuzmicheva, J.-Y. Lin, S. Kuzmichev, O. Volkova and A. Vasiliev, *CrystEngComm* **2013**, *15*, 1989-1993.

17 A. E. Böhmer, F. Hardy, F. Eilers, D. Ernst, P. Adelmann, P. Schweiss, T. Wolf and C. Meingast, *Phys. Rev. B: Condens. Matter* **2013**, *87*, 180505.

18 A. E. Böhmer, V. Taufour, W. E. Straszheim, T. Wolf and P. C. Canfield, *Phys. Rev. B: Condens. Matter* **2016**, *94*, 024526.

19 M. Ma, D. Yuan, Y. Wu, H. Zhou, X. Dong and F. Zhou, *Supercond. Sci. Technol.* **2014**, *27*, 122001.

20 K. D. Oyler, X. Ke, I. T. Sines, P. Schiffer and R. E. Schaak, *Chem. Mater.* **2009**, *21*, 3655-3661.

21 S. J. Li, D. Li, J. J. Jiang, G. B. Liu, S. Ma, W. Liu and Z. D. Zhang, *J. Appl. Phys.* **2014**, *115*, 17B502.

22 D. Li, D. Pan, W. Liu, X. Li, M. Chen, S. Li, Y. Li, J. Tan, D. Sun, Z. Wang, Z. Han and Z. Zhang, *Chem. Mater.* **2017**, *29*, 842-848.

23 U. Pachmayr, N. Fehn and D. Johrendt, *Chem. Commun.* **2016**, *52*, 194-197.

24 F. Nitsche, T. Goltz, H. H. Klauss, A. Isaeva, U. Müller, W. Schnelle, P. Simon, T. Doert and M. Ruck, *Inorg. Chem.* **2012**, *51*, 7370-7376.

25 J. T. Greenfield, S. Kamali, K. Lee and K. Kovnir, *Chem. Mater.* **2015**, *27*, 588-596.

26 TOPAS-Academic, V5, Coelho Software, Brisbane, Australia, **2007**.

27 S. Margadonna, Y. Takabayashi, M. T. McDonald, K. Kasperkiewicz, Y. Mizuguchi, Y. Takano, A. N. Fitch, E. Suard and K. Prassides, *Chem. Commun.* **2008**, 5607-5609.

28 T. M. McQueen, A. J. Williams, P. W. Stephens, J. Tao, Y. Zhu, V. Ksenofontov, F. Casper, C. Felser and R. J. Cava, *Phys. Rev. Lett.* **2009**, *103*, 057002.

29 E. Dagotto, *Rev. Mod. Phys.* **2013**, *85*, 849-867.

4 Fe_3GeTe_2-related structures

4.1 $Fe_{2.3}GeTe$ – a new layered ferromagnetic telluride

Juliane Stahl, Lukas Neudert, Oliver Oeckler and Dirk Johrendt

Parts published in: *Zeitschrift für Anorganische und Allgemeine Chemie* **2016**, *642*, 989–996.

Abstract

$Fe_{2.3}GeTe$ was obtained by solid state synthesis and the crystal structure was determined by single crystal X-ray diffraction. The telluride exhibits a new structure type [$P\bar{3}m1$, a = 3.9891(6) Å and c = 10.766(3) Å] composed of layers stacked along c. FeGe hexagons sandwiched by additional iron atoms are separated by Te double layers building a van der Waals gap. Similar structural motifs are found in $Fe_{2-\delta}Ge$ and Fe_3GeTe_2.[1,2] The Fe3 site in the FeGe hexagons has Fe vacancies [occ(Fe3) = 0.79], while additional electron density between the Te layers indicates iron in the van der Waals gap [occ(Fe4) = 0.13]. The total iron content of the structure is in accordance with EDS measurements. Diffuse intensity along [001]* was observed with electron diffraction indicating a non-periodic stacking of the $Fe_{2.3}GeTe$ layers. SAED patterns correspond to reciprocal lattice sections based on X-ray data. Magnetic susceptibility measurements indicate ferromagnetic ordering below T_C = 241 K. The Curie-Weiss fit gives an effective moment of μ_{eff} = 4.55 μ_B per iron atom and the

ferromagnetic Weiss temperature Θ = 238 K. Isothermal magnetization at 1.8 K shows a saturation moment μ_{sat} = 1.37 μ_B at 5 T. The magnetic properties are similar to those of Fe_3GeTe_2.[2]

Introduction

Despite the great variety of materials that show high temperature superconductivity, the underlying pairing mechanism is yet not definitely clarified.[3] Whether the suggestion of a common mechanism for unconventional superconductivity is correct or not, indications for the search of new materials can be deduced. It is most likely that the exchange of spin fluctuations play an important role, suggesting a strong coupling of the magnetic and superconducting states.[3,4] Therefore, synthesis of compounds containing magnetic 3*d* ions in quasi two-dimensional substructures is believed to be a promising attempt in the search for new unconventional superconductors.[3,5,6] For example, a pronounced layered character is inherent in transition metal dichalcogenides, due to the van der Waals gap between the chalcogenide atoms.[7] Beside numerous examples of semiconducting dichalcogenides, metallic compounds MCh_2 [*M* = Ti, Zr, Hf, V, Nb, Ta, Mo, W, Ir, Pd, Pt; *Ch* = S, Se, Te] with a variety of physical and chemical properties are known. However, when it comes to magnetically ordered layered dichalcogenides, the experimentally confirmed compounds shrink to VCh_2 [*Ch* = S, Se].[7-9] This is credible since the Mermin-Wagner theorem predicts long-range order in 2D materials to be unstable.[10] Extending the field of transition metal chalcogenides containing a van der Waals gap on ternary compounds gives the possibility of greater structural diversity and possibly magnetic properties. Recently discovered Fe_3GeTe_2 and Ni_3GeTe_2 are examples for quasi two-dimensional compounds containing magnetic 3*d* ions.[2] The layered character is also ascribed to the van der Waals gap between two Te layers.

Between these square nets of the transition metal and hexagonal rings composed of Fe/Ni and Ge ions are stacked alternately [see Figure 4-1 bottom left]. While the Ni compound exhibits no ordering the Fe compound is ferromagnetic below 230 K. This desired combination of 2D character and magnetic ordering has led to intensive research in the past few years to carefully characterize the properties of Fe_3GeTe_2.[11-16] In contrast, no further compound has been found in the Fe-Ge-Te system, besides the orthorhombic Fe_2GeTe_4 with 3D structure.[17,18]

Here, the synthesis and crystal structure determination of $Fe_{2.3}GeTe$ is presented. The compound exhibits similar structural motifs to Fe_3GeTe_2 and is also ferromagnetically ordered below 241 K. Together with the pronounced layered character on the microscopic and macroscopic scale, these properties make $Fe_{2.3}GeTe$ a candidate for further investigation, including potential unconventional superconductivity.

Experimental

For preparation of polycrystalline samples of $Fe_{2.3}GeTe$ the elements Fe [Chempur, 99.9%], Ge [Aldrich, 99.999%], and Te [Aldrich, 99.999%] in molar ratio 2.3 : 1 : 1 were used. The mixtures were filled in alumina crucibles, sealed in silica ampoules under argon atmosphere and heated in two annealing steps, first at 973 K for 60 h and after cooling to room temperature to 1073 K for 60 h. All heating and cooling rates were 100 K h^{-1}. The metallic grey products consist of plate-like crystals and are stable at air. According to powder X-ray diffraction data the products contain small amounts of $Fe_{1.67}Ge$ and Fe_3GeTe_2 as impurity phases.

Single crystal X-ray diffraction data was collected with APEX2 software on a Bruker D8-Quest diffractometer [Mo-K_α radiation; graphite mo-

nochromator] and structure solution and refinement was carried out using Jana2006 program package. [19,20] Powder X-ray diffraction patterns were recorded on a Stoe Stadi P diffractometer [Mo-$K_{\alpha 1}$ radiation; Ge-111 monochromator; capillary sample holder] and Rietveld refinement was done using TOPAS package.[21] Energy-dispersive spectra were collected on a Carl Zeiss Evo-Ma10 microscope [SmartSEM software] with a Bruker Nano EDS X-Flash detector 410-M [QUANTAX 200 software].[22 23] Magnetic measurements were conducted with a Quantum Design SQUID Magnetometer MPMS XL-5. For transition electron microscopy of selected drop-casted or matrix embedded, thinned crystals a FEI Tecnai G20 microscope [Selected area electron diffraction SAED and EDS mapping] and a Titan Themis 300 microscope [scanning transmission electron microscope high-angle annular dark-field imaging STEM-HAADF] were used. The data was evaluated using Digital Micrograph, ProcessDiffraction7 and ES Vision software. SAED patterns were simulated using JEMS software.

Results and Discussion

Crystal structure. The crystal structure of $Fe_{2.3}GeTe$ was determined by single crystal X-ray diffraction. The compound exhibits a new structure type in the trigonal crystal system with the space group $P\bar{3}m1$ and the lattice parameters a = 3.9891(6) Å and c = 10.766(3) Å [Figure 4-1 middle; Table A-22 to Table A-24]. The structure shows similar motifs as $Fe_{2-\delta}Ge$, which is build up by planar hexagonal FeGe layers alternating with pure Fe layers [Figure 4-1 right]. In $Fe_{2.3}GeTe$, the structure is cut by a van der Waals gap along the c axis resulting in separated blocks of two FeGe layers and three Fe layers. The van der Waals gap is composed of double layers of Te shifted to each other by the vector (1/3 2/3) in the *ab* plane. This structural motif is also known from Fe_3GeTe_2 which

contains blocks of one hexagonal FeGe layer sandwiched by two pure Fe layers separated by the van der Waals gap [Figure 4-1 left]. The FeGe layers are slightly corrugated in $Fe_{2.3}GeTe$ with hexagons in chair conformation and dihedral angles of ±15.9(1)°, while they are planar in the structures known in the literature.

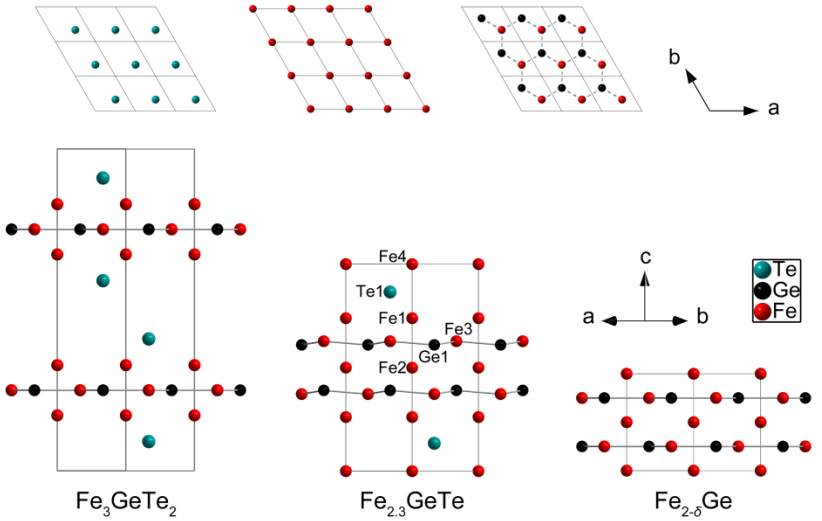

Figure 4-1 Bottom: Crystal structure of $Fe_{2.3}GeTe$ along [110] [middle; Ge split position omitted for clarity] in comparison to Fe_3GeTe_2 [left] and $Fe_{2-\delta}Ge$ [right].Top: Te [left], Fe [middle] and FeGe [right] atom layers of $Fe_{2.3}GeTe$ projected to the *ab* plane.

Both, $Fe_{2-\delta}Ge$ [*occ*(Fe2) = 0.55-0.95] and Fe_3GeTe_2 [*occ*(Fe2) = 0.71-0.92], exhibit an iron deficiency of the Fe site within the FeGe hexagons.[1,24] Similar results are observed for $Fe_{2.3}GeTe$ from single crystal X-ray diffraction with *occ*(Fe3) = 0.79(1) [0.76(1) from powder X-ray diffraction]. In addition, the data shows significant electron density in the van der Waals gap which indicates an Fe4 site between the Te layers with

an occupation refined to *occ*(Fe4) = 0.13(1) [0.18(2) from powder X-ray diffraction]. A similar partially occupied site is found for the Fe_3GeTe_2 isotypic compound Ni_3GeTe_2 with *occ*(Ni3) = 0.25.[2] Altogether for the new compound a resulting stoichiometry of $Fe_{2.36}Ge_{0.99}Te$ is refined from single crystal data, and $Fe_{2.44}Ge_{0.96}Te$ from powder X-ray diffraction data. This is in accordance with the ratio of Fe : Ge : Te = 2.21(11) : 0.87(5) : 1 obtained from EDS measurements. The deviation of the Ge content is observed for all compounds containing Fe, Ge and Te and is considered as an error of the method, with regard to the results of the X-ray diffraction data.

Since the *a* axes of the three compounds shown in Figure 4-1 are nearly identical with *a*($Fe_{2-\delta}Ge$) = 4.008 Å [δ = 0.33], *a*(Fe_3GeTe_2) = 3.991 Å and *a*($Fe_{2.3}GeTe$) = 3.989 Å they exhibit comparable atomic distances.[1,2] The Te-Te distances across the van der Waals gap are 3.70(1) Å in $Fe_{2.3}GeTe$ and 3.74 Å in Fe_3GeTe_2. This results in distances of the Te layers in *c* direction of 2.89 Å and 3.06 Å, respectively. The shorter layer distance in $Fe_{2.3}GeTe$ can be attributed to the presence of the additional Fe4 site in the van der Waals gap and therefore the weak ionic interactions. In contrast, the distances of the pure Fe layers *d*(Fe1Fe2) = 2.67(1) Å are slightly elongated compared to Fe_3GeTe_2 [*d*(Fe1Fe1) = 2.55 Å] and $Fe_{2-\delta}Ge$ [*d*(Fe1Fe1) = 2.50 Å; δ = 0.33]. However, even with this distance Fe-Fe bonding interactions across the FeGe rings can be assumed. Figure 4-2 shows the Rietveld refinement of powder X-ray diffraction data of one polycrystalline sample of $Fe_{2.3}GeTe$. All samples contain small amounts of the impurity phases $Fe_{2-\delta}Ge$ and Fe_3GeTe_2 [< 5 mol%], probably due to the structural similarity of the compounds. Overall, the calculated pattern is in good agreement with the measured data, so the structure model is assumed to be reasonable.

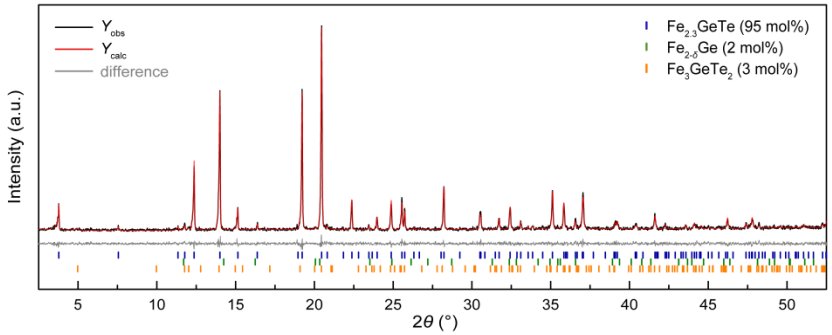

Figure 4-2 Rietveld refinement of a powder X-ray diffraction pattern [Mo-$K_{\alpha 1}$] of $Fe_{2.3}GeTe$ [blue positions], with impurity phases $Fe_{2-\delta}Ge$ [green positions] and Fe_3GeTe_2 [orange positions].

Structural disorder. Refinement of the single crystal X-ray diffraction data with the structure model described above yielded poor *R*-values [R_1 = 0.056, $wR(F^2)$ = 0.135] and significant residual electron density at the Ge site. A distinctly improved refinement was achieved by splitting the Ge position into three positions. Thereby the *R*-values drop to R_1 = 0.030 and $wR(F^2)$ = 0.067, so the model with Ge split position is considered to describe the data more accurate. This observation is attributed to the occurrence of structural disorder in the crystals as it is determined for Ni_3GeTe_2.[2] TEM investigations revealed two different scattering phenomena for this compound displaying deviations from the average structure. Diffuse intensities along the stacking direction suggest in-plane ordering of the vacancies in the NiGe hexagonal layers and a non-periodic stacking. Additionally, double diffraction is caused by moiré effects due to the plate-like crystals.

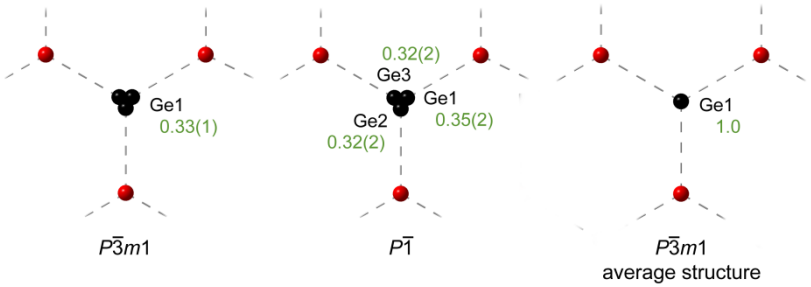

Figure 4-3 Excerpts of the hexagonal FeGe layer projected to the *ab* plane with Ge split position from Rietveld refinement of single crystal X-ray diffraction data in different space groups, *P*3*m*1 [left] and *P*1 [middle], compared to the average structure with Ge on special position [right]. Refined occupations are given in green.

Splitting of the Ge position in $Fe_{2.3}GeTe$ [$P\bar{3}m1$] is achieved by shifting the atom from the special Wyckoff position 2*d* [1/3 2/3 0.609(1)] [Figure 4-3 right] to the general position 6*i* [Figure 4-3 left]. The fractional coordinates refine to $x = 0.3599(7)$, $y = 0.6401(7)$ and $z = 0.6103(1)$ with the Ge atoms shifting towards the Fe3 atoms. Free refinement of the occupation yields 0.33(1) which coincides with full occupation of the Ge site. In order to verify that the splitting occurs statistically the occupations of the three resulting positions have to be refined independently. For this, the symmetry was reduced to space group $P\bar{1}$ and fractional coordinates and occupations were refined freely, keeping the distances of the Ge positions equal [Figure 4-3 middle]. Again a shift of the Ge atoms towards the Fe3 atoms is observed with occupations of almost 0.33 which indicates a statistical splitting as expected. Taking into account the occupational deficiency on the Fe3 site, the splitting may be caused by a tendency of the Ge atoms towards neighboring vacancies. An indication for this is the shortening of the Fe3-Ge1 distance upon splitting to 2.13(1) Å which is noticeably shorter than distances found in

Fe_3GeTe_2 [d(GeFe2) = 2.30 Å] and $Fe_{2-\delta}Ge$ [d(GeFe2) = 2.31 Å; δ = 0.33].[1,2] The refined occupation of the Fe3 site is 0.79(1), though, which gives 0.21 vacancies deviating from the occupation of 0.33 for the Ge split positions.

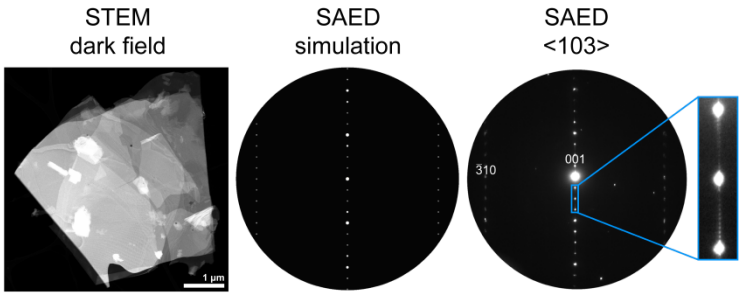

Figure 4-4 STEM dark field image showing superposition of plate-like crystals [left] and SAED pattern along <103> compared with simulation based on structural model from X-ray diffraction data [right]. Diffuse scattering along [001]* is highlighted in the blue box.

A closer analysis of the structural disorder of $Fe_{2.3}GeTe$ was done by transmission electron microscopy. Initially recorded SAED patterns could not be indexed with the structural model since additional reflections occurred. This is explained by the superposition of the plate-like crystals on a microscopic scale as can be seen in STEM images [Figure 4-4 left]. In order to exclude that the additional reflections are attributed to impurity phases grown on the crystals, EDS mappings were conducted, showing identical composition over the whole crystal. For further measurements, the crystals were embedded in a matrix and thinned, to ensure that single domains are measured. SAED patterns of these domains along special projections are in good agreement with corresponding simulations and no superstructure reflections are observed

[see for instance zone axis <103> in Figure 4-4 right; further tilt series are given in Figure A-2]. However, diffuse scattering along [001]* indicates a non-periodic stacking of the layers along *c*. Closer analysis of the streaks leads to an observation of 13 distinct reflections between the main reflections along [001]* [see blue box in Figure 4-4]. It should be noted that the diffuse intensities are very weak and therefore not noticeable in the less sensitive X-ray diffraction. Diffraction images of the crystals along [001]* are shown in Figure 4-5 [top] from X-ray and electron diffraction. Both can be indexed with the structural model, but both also show weak additional reflections. This states that even in thin crystals superposition of different domains occurs. Same is observed in HRTEM images [Figure 4-5 bottom], which leads to Moiré patterns and additional reflections in associated Fourier transforms.

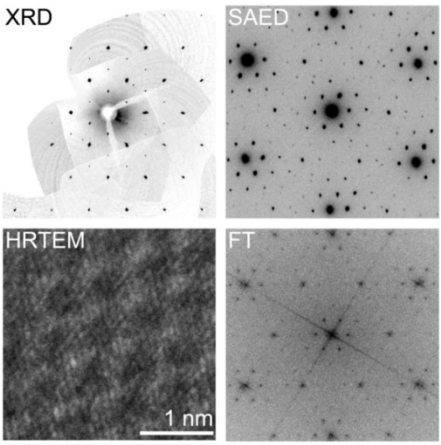

Figure 4-5 Top: Reciprocal lattice section along [001]* from single crystal X-ray diffraction [left] and selected area electron diffraction [right]. Bottom: High resolution TEM image [left] and associated Fourier transform [right] along [001]*.

TEM investigations of Ni_3GeTe_2 give similar results and are explained by in-plane ordering of the vacancies in the hexagonal NiGe layers with non-periodic stacking leading to diffuse intensities.[2] Taking into account the Ge split position observed in single crystal X-ray diffraction the same is probable for $Fe_{2.3}GeTe$.

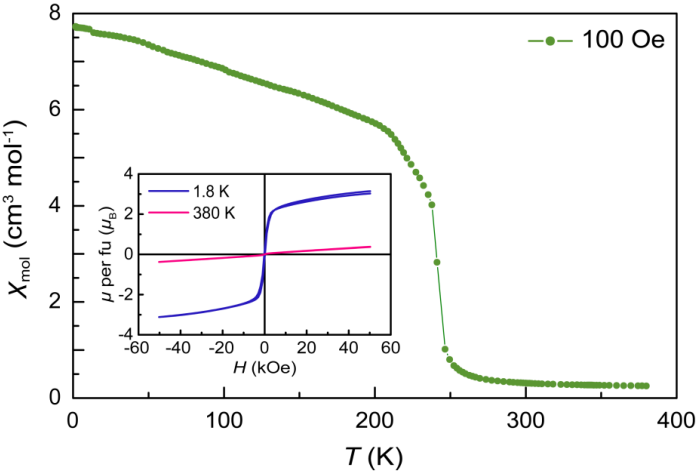

Figure 4-6 Magnetic susceptibility of $Fe_{2.3}GeTe$ measured at 100 Oe between 1.8 and 380 K [green]. Insert: isothermal magnetization per formula unit at 1.8 K [blue] and 380 K [pink].

Magnetic properties. Magnetic susceptibility measurements were conducted at 100 Oe and 20 kOe for a sample of $Fe_{2.3}GeTe$ containing 2 mol% $Fe_{2-\delta}Ge$ and 3 mol% Fe_3GeTe_2 [Figure 4-6]. Ferromagnetic ordering is observed with a Curie-temperature of 241(1) K taken from zero point of the second derivative of the measurement at 100 Oe. Curie-Weiss fitting of the paramagnetic region above the ordering temperature for the measurement at 20 kOe gives $\chi_0 = 0.0001(3)$ cm^3 mol^{-1}, $\Theta = 238.3(3)$ K and $C = 5.96(5)$ cm^3 mol^{-1} K, yielding an effective paramag-

netic moment of μ_{eff} = 4.55(2) μ_B per Fe atom. Isothermal magnetizations measured above and below T_C are shown in the insert in Figure 4-6. While at 380 K paramagnetic behavior is observed, the measurement at 1.8 K reveals a ferromagnetic hysteresis with small coercive field of about 260 Oe and saturation moment of 1.37(1) μ_B per Fe atom at 50 kOe. These values are comparable to those of Fe_3GeTe_2 [H_c = 300 Oe, μ_{sat} =1.58 μ_B per Fe at 5 K].[11] The additional inflection point in the 100 Oe measurement at about 225 K [see Figure 4-6] is ascribed to the impurity phase Fe_3GeTe_2 since for this compound Curie-temperatures of 143-229 K depending on the Fe content are reported.[24,25]

Conclusions

$Fe_{2.3}GeTe$ was synthesized by solid state reaction and the trigonal crystal structure was determined by single crystal X-ray diffraction. The compound exhibits similar structural motifs as $Fe_{2-\delta}Ge$ and Fe_3GeTe_2 and is besides the latter and orthorhombic Fe_2GeTe_4 the third known compound in the Fe-Ge-Te-system. The structure of $Fe_{2.3}GeTe$ is quasi two-dimensional on the microscopic scale due to double layers of Te building a van der Waals gap. The layered character can easily be recognized on the macroscopic scale by intergrowth of the plate-like crystals. This superposition is apparent by inexplicable reflections in electron diffraction patterns which are not observed when the sample is embedded and thinned. Additionally, structural disorder occurs in $Fe_{2.3}GeTe$ crystals, presumably due to in-plane ordering of Fe vacancies and Ge atoms in the hexagonal layers and non-periodic stacking. The magnetic properties of the new compound are comparable to Fe_3GeTe_2 with ferromagnetic ordering below 241 K.

4.2 The van der Waals Ferromagnets $Fe_{5-\delta}GeTe_2$ and $Fe_{5-\delta-x}Ni_xGeTe_2$ – Crystal Structure, Stacking Faults, and Magnetic Properties

Juliane Stahl, Evgeniya Shlaen and Dirk Johrendt

Published in: *Zeitschrift für Anorganische und Allgemeine Chemie* **2018**, *644*, 1923-1929.[b]

Abstract

$Fe_{5-\delta}GeTe_2$ was synthesized by heating the elements at 1050 K and characterized by single crystal and powder X-ray analysis. The structure [*R*3*m*, a = 4.0376(4) Å, c = 29.194(6) Å] consists of $Fe_{5-\delta}Ge$ layers separated by tellurium double layers forming a van der Waals gap. The pronounced two-dimensional character of $Fe_{5-\delta}GeTe_2$ causes stacking faults along the c direction. Simulations of different stacking variants using the DIFFaX software reveal disorder occurring in domains. Magnetic measurements of $Fe_{5-\delta}GeTe_2$ show ferromagnetism below 279 K with a saturation moment of 1.80 μ_B at 1.8 K. Nickel substitution of the iron sites has little influence on the structure but changes the saturation moment, which passes through a maximum of 2.11 μ_B in $Fe_{4.11}Ni_{0.50}GeTe_2$. This indicates that structural influences as well as the dilution of the magnetic iron atoms play a decisive role.

[b] Supplementary information in appendix A.5

Introduction

The interest in van der Waals materials has been rising for many years as the methods of producing and investigating 2D materials are steadily improving.[26-28] These materials are candidates for applications in spintronic and other technologies. Considering ternary van der Waals compounds, one expects an even wider range of properties.[26] However, magnetic phenomena in 2D materials are difficult to obtain since long-range order cannot persist according to the Mermin-Wagner theorem.[10,29] Nevertheless, thin films of $Cr_2Ge_2Te_6$, Fe_3GeTe_2, and $FePS_3$ for example show intrinsic ferromagnetism or antiferromagnetism, which leads to good prospects in spintronic device applications.[29-31] The high Curie temperature of 220 K and strong anisotropy of the magnetic state favors Fe_3GeTe_2 over other ferromagnetic van der Waals materials.[32,33] The hexagonal structure of Fe_3GeTe_2 contains metal atom substructures sandwiched by tellurium layers building the van der Waals gap.[2] The magnetic and structural properties of the bulk phase have been intensively studied over the last few years, characterizing the material as quasi-2D itinerant ferromagnet with easy axis parallel to *c*.[11-16,34] Theoretical calculations support these findings.[35,36] A decisive advantage is the possibility of tuning the magnetic parameters through chemical modification. On the one hand, this is due to the dependence of the magnetic ordering on the iron content. The content can be reduced by introducing vacancies, but also by substitution of the iron atoms with nickel, since the isotypic compound Ni_3GeTe_2 exhibits no ordering.[24,25] Thereby, the substitution corresponds to a dilution of the magnetic centers. Additionally, a structural influence is possible by substitution of the non-magnetic Ge atoms. Thus, suppression of the magnetic ordering was achieved in the solid solution $Fe_{3-\delta}Ge_{1-x}As_xTe_2$ and attributed to the elongation of the Fe-Fe distances of the pure Fe layers.[37] Since the other isotypic com-

pounds Ni_3ETe_2 [E = Ga, In, Sn] and Ni_2SbTe_2 exist, beside Ni_3GeTe_2 and Fe_3AsTe_2, there is room for further investigations in this field.[2,38-43] $Fe_{2.3}GeTe$ is a further compound in the Fe-Ge-Te system showing comparable structure motifs to Fe_3GeTe_2 and is ferromagnetic below 239 K.[44] Stacking disorder in $Fe_{2.3}GeTe$ was resolved by TEM investigations and suggests a similar anisotropic character as in Fe_3GeTe_2. Another compound in the Fe-Ge-Te system is mentioned in the literature as side phase, but so far only the composition Fe_5GeTe_2 has been determined.[45] Both compounds, $Fe_{2.3}GeTe$ and Fe_5GeTe_2, should be given a closer look, as they show similar characteristics to Fe_3GeTe_2 and therefore may be promising van der Waals ferromagnets.

In this work we report on the compound $Fe_{5-\delta}GeTe_2$, which has already been mentioned in the past, but not characterized.[45] We show the crystal structure solved from single crystal diffraction data and find that the solution has been impeded so far by stacking disorder. By examining this disorder more precisely using DIFFaX simulations, it turns out that faultless and faulted domains occur concurrently. $Fe_{5-\delta}GeTe_2$ shows ferromagnetic order below 279 K with a low coercive field and saturation moment comparable to Fe_3GeTe_2. This, together with the layered structure, suggests a strongly anisotropic magnetic character. We managed to adjust the magnetic properties by substitution of the iron sites by nickel, showing that both structural influences and dilution of magnetic centers affect the ordering.

Experimental

Polycrystalline samples of $Fe_{5-\delta}GeTe_2$ and $Fe_{5-\delta-x}Ni_xGeTe_2$ were prepared *via* solid state reaction from pure elements. Therefore Fe [Chempur, 99.9%], Ni [Chempur, 99.99%], Ge [Aldrich, 99.999%] and Te [Aldrich,

99.999%] powder were mixed in molar ratio 4.5-x : x : 1 : 2 with x = 0, 0.1, 0.25, 0.5, 0.75, 1.0, 1.1, 1.25, 1.5. The mixtures were filled in alumina crucibles and sealed in silica ampoules in an argon atmosphere. The samples were heated to 1023 K for 100 to 120 h [heating and cooling rate: 100 K h^{-1}]. The products are metallic grey and stable at air. Single crystals show a hexagonal plate-like shape and a pronounced layer character. All samples contain $Fe_{3-x}Ni_xGeTe_2$ as a side phase with 9-18 mol%.

Single crystal X-ray diffraction analysis was done with a Bruker D8-Quest diffractometer [Mo-K_α radiation; graphite monochromator]. Data was collected and processed using APEX2 software and structure solution and refinement was done using Jana2006 program package.[19,20] Powder X-ray diffraction analysis of the polycrystalline samples was conducted with a Stoe Stadi P diffractometer [Mo-$K_{\alpha1}$ radiation: Ge-111 monochromator] with capillary sample holder. Rietveld refinement of the recorded patterns was done using TOPAS package.[21] Simulations of powder patterns based on structure models with varying proportions of stacking faults were realized using DIFFaX program.[46] Instrumental broadening was described by pseudo-Voigt functions. Analysis of the composition was carried out *via* energy-dispersive spectroscopy with a Carl Zeiss Evo-Ma10 controlled by SmartSEM software.[23] Data was collected with a Bruker Nano EDS X-Flash detector 410-M and the QUANTAX 200 software.[22] Magnetic measurements were conducted either with a Quantum Design SQUID Magnetometer MPMS XL-5 or a PPMS with VSM option.

Results and Discussion

Crystal structure. The crystal structure of $Fe_{5-\delta}GeTe_2$ was solved from single crystal X-ray data [Mo-K_α radiation] in the non-centrosymmetric space group *R*3*m* with $a = 4.0376(4)$ Å and $c = 29.194(6)$ Å [Figure 4-7; for further detail see Table A-25 to Table A-27].

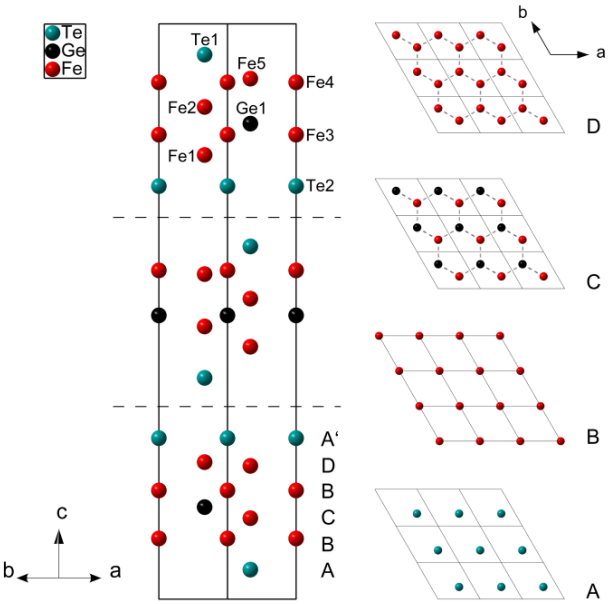

Figure 4-7 Crystal structure of $Fe_{5-\delta}GeTe_2$ projected along [110] [Ge1' position is omitted for clarity]. The structure consists of building blocks stacked along [001] direction, which are composed of atomic layers A-D and A' [projection of the individual layers along [001] on the right].

The structure is composed of repetitive building blocks stacked along *c* direction and shifted to each other according to the *R*-centered space group. The blocks consist of atomic layers A-D and A' [see Figure 4-7]. The outer layers [A and A'] are build from Te atoms, which results in van

der Waals gaps between the blocks. In the *ac* plane layer A' [Te1 atoms] is shifted to layer A [Te2 atoms] by the vector (1/3 2/3). Neighboring Te atoms show a distance of *d*(Te1Te2) = 3.85(3) Å which gives a distance of the Te layers of *d*(A-A') = 3.06 Å. This is consistent with values found for the structurally similar compounds Fe_3GeTe_2 [*d*(TeTe) = 3.74 Å] and $Fe_{2.3}GeTe$ [*d*(TeTe) = 3.69 Å].[2,44] The sections between the Te layers within the building blocks consist of Fe layers (B) stacked alternately with layers built up by FeGe (C) and FeFe hexagons (D), resulting in a stacking sequence of ABCBDA' for each block. Since the Ge atom showed a strongly elongated anisotropic displacement parameter along *c*, the Ge site was refined with a split position, which resulted in significantly lower *R* factors. Free refinement of the occupations resulted in *occ* = 0.5 for both positions. FeGe hexagons (C) sandwiched by Fe atoms (B) also occur in Fe_3GeTe_2, $Fe_{2.3}GeTe$ and binary $Fe_{2-\delta}Ge$ with 3D instead of layer character.[1,2,44] While the FeGe layers in Fe_3GeTe_2 and $Fe_{2-\delta}Ge$ are planar [dihedral angles = 0°], they are corrugated in $Fe_{2.3}GeTe$ [dihedral angles = ±17.2°] and $Fe_{5-\delta}GeTe_2$ [dihedral angles = ±24.5°, ±40.1°, ±51.9°, ±65.3°] in chair conformation. In $Fe_{5-\delta}GeTe_2$ the distance between the B layers of *d*(Fe1Fe2) = 2.52(1) Å is comparable with the shortest distance in α-Fe [*d*(FeFe) = 2.47 Å], which suggests Fe-Fe bonds.[47] In addition, FeFe hexagons (D) with even shorter Fe-Fe distances [*d*(Fe4Fe5) = 2.34(1) Å] occur in the new compound, which have not been observed in the Fe-Ge-Te-system so far. These layers are also slightly corrugated with dihedral angles of ±20.3°. Honeycomb layers built up solely of Fe atoms are known from the structurally related compounds Gd_2XFe_2 [*X* = Br, I] and $Y_2Br_2Fe_{2+x}$, for example, which show comparable short Fe-Fe distances [*d*(FeFe) = 2.33 Å, 2.27 Å].[48,49] The splitting of the Ge position in $Fe_{5-\delta}GeTe_2$ causes one very short Fe-Ge distance *d*(Fe5Ge1') = 1.88(1) Å. Given the *occ*(Fe5) of 0.73, this

indicates that the *sof* of the Ge split position should deviate from 0.5, which is however not supported by the data. We suggest that this is a consequence of the inaccuracy caused by the stacking disorder.

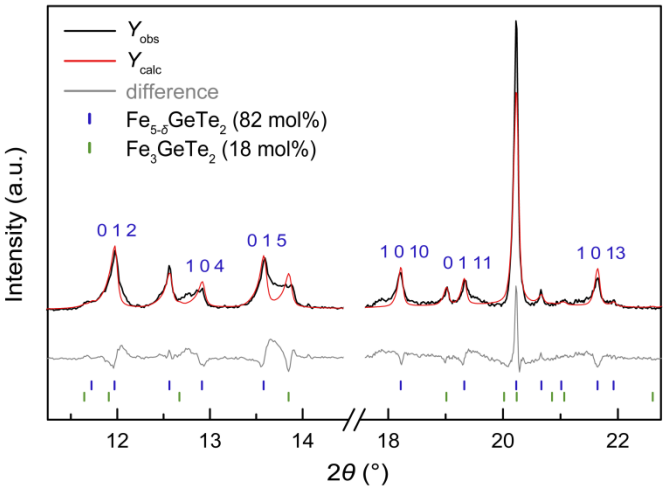

Figure 4-8 Excerpts of the Rietveld refinement of a powder diffraction pattern [Mo-$K_{\alpha 1}$ radiation] of $Fe_{5-\delta}GeTe_2$ [blue positions], with Fe_3GeTe_2 [green positions] as side phase. Indices of selected reflections showing broadening due to stacking disorder are given in blue.

Additionally, the Fe3 site in the FeGe hexagons is iron deficient with *occ*(Fe3) = 0.89. Rietveld refinements of X-ray powder diffraction data reveal similar occupations. Overall, for various samples, δ is approximately 0.4, which is confirmed by EDS analyses. Iron deficiency of the Fe site within the FeGe rings is also found for $Fe_{2-\delta}Ge$ [*occ*(Fe2) = 0.55-0.95], Fe_3GeTe_2 [*occ*(Fe2) = 0.71-0.92] and $Fe_{2.3}GeTe$ [*occ*(Fe3) = 0.79].[1,24,44] An additional site within the van der Waals gap is partially occupied with iron [*occ*(Fe4) = 0.13] in $Fe_{2.3}GeTe$ and with nickel in Ni_3GeTe_2 verified by TEM investigations.[2,44] In contrast to this,

significant residual electron density is smeared along [001] in $Fe_{5-\delta}GeTe_2$. Diffuse streaks along 00*l* in the single crystal diffraction patterns indicate stacking disorder of the layers [see Figure A-3]. The powder diffraction patterns even more display disorder by significant shoulders of corresponding peaks. Figure 4-8 shows excerpts of the Rietveld refinement containing 82 mol% $Fe_{5-\delta}GeTe_2$ and 18 mol% Fe_3GeTe_2 as impurity phase [for complete Rietveld refinement see Figure A-4]. Pronounced intensity misfits due to broadening of the 10*l* and 01*l* reflections are visible, which confirms the presumed disorder along the [001] direction. Other reflections, for example the main reflection 110 [at $2\theta = 20.23°$ in Figure 4-8], show no good agreement of the intensity as well. This is because the total Rietveld refinement is impeded by the broadening and thus lowered intensity of the 10*l* and 01*l* reflections.

Stacking faults. To further investigate the disorder, powder patterns of different stacking models were simulated using the DIFFaX software and compared with experimental data.[46] Taking the strong bonds within the building blocks of $Fe_{5-\delta}GeTe_2$ into account, a shift of the layers is more likely to occur at the van der Waals gap, as interactions there are weak. Therefore, one block [ABCBDA', 1/3 of the original unit cell, see Figure 4-7] of the structure was used as a base layer for the generation of different stacking variants [Table A-29]. In order to obtain the ordered structure solved from single crystal refinement, this base layer has to be stacked two times with the vector S1 = (2/3 1/3 1), referred to as *original stacking* in the following [Figure 4-9, left]. For further variants it was assumed that the distances of the Te atoms forming the van der Waals gap are maintained upon shifting of the layers. This leads to only one other probable stacking with the vector S2 = (0 0 1) [Figure 4-9, right], referred to as *stacking fault*.

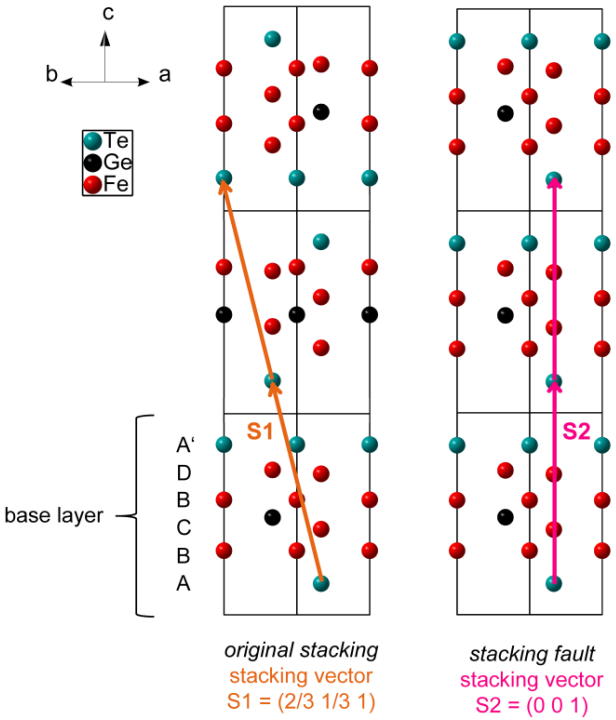

Figure 4-9 Probable stacking patterns of one building block [base layer] of $Fe_{5-\delta}GeTe_2$ depicted for three layers, respectively [Ge split position omitted for clarity]. Vector S1 describes the stacking of the original structure [left] solved from single crystal data. Vector S2 describes the only other probable stacking variant preserving the Te-Te distances [right].

We used the DIFFaX routine to simulate a statistical ensemble of crystallites with infinite number of unit cells in all directions. Figure 4-10 shows a measured powder pattern of $Fe_{5-\delta}GeTe_2$ [impurity phase Fe_3GeTe_2 highlighted in orange] in comparison with the simulated patterns. The blue line depicts the simulated pattern of the ordered structure without stacking faults. Distinct differences to the experimental data are visible in

the intensity ratios and the peak width of specific reflections. As already observed in the Rietveld refinement, the 10*l* and 01*l* reflections exhibit too small intensities and pronounced shoulders in the measured pattern. An increasing broadening of these reflections occurs with more stacking faults, which is exemplified by a simulated pattern with a probability of 20% S2 stacking in Figure 4-10 [green line; for further simulations with other probabilities see Figure A-7]. However, this type of stacking does not adequately describe the experimental data, since the measured diffractogram contains peaks with shoulders. This indicates the presence of domains with different probabilities for faults within the crystals. In case of $Fe_{5-\delta}GeTe_2$, a mixture of faultless domains [blue line in Figure 4-10] and domains with 20% stacking faults [green line in Figure 4-10] gives a good description of the peak shape.

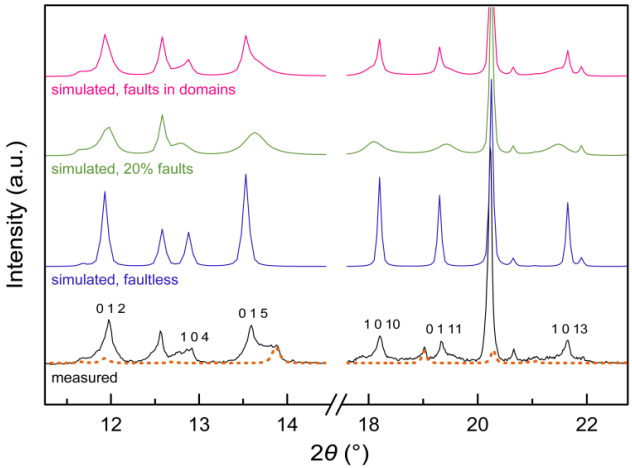

Figure 4-10 Excerpts of a powder diffraction pattern [Mo-$K_{\alpha 1}$ radiation] of $Fe_{5-\delta}GeTe_2$ [black line], with impurity phase Fe_3GeTe_2 [orange dashed line] and indices of selected reflections. Simulated patterns without stacking faults [blue line], with 20% stacking faults [green line] and with 20% faults in domains [pink line].

To determine the ratios of the domains, powder patterns with different probabilities of occurrence of the domains were simulated [Figure A-7]. The best fitting of the experimental data is obtained at a ratio of faultless domains : 20% faulted domains = 1 : 2, shown as pink line in Figure 4-10. We note that the DIFFaX simulation only allows an estimation of disorder. In addition, idealized vectors were used for the generation of stacking models, assuming that the Te-Te distances are preserved. Nevertheless, the resulting model is in good agreement with the experimental data, such as the residual electron density smeared along [001] observed in single crystal diffraction, and the peak profiles observed in powder diffraction. We therefore suggest that the S2 stacking is the main fault in $Fe_{5-\delta}GeTe_2$ and that both, faultless and faulted domains, arise in the samples.

Magnetic properties. Magnetic susceptibility measurements of a $Fe_{5-\delta}GeTe_2$ sample with $\delta = 0.37(14)$ reveal ferromagnetic ordering below T_C = 279(1) K, with T_C taken from zero point of the second derivative of a measurement at 100 Oe [Figure A-8]. Figure 4-11 shows the inverse magnetic susceptibility between 1.8 K and 380 K at 20 kOe. A Curie Weiss fit of the paramagnetic region was not possible since too few data were measured above the ordering temperature. The isothermal magnetization curve of $Fe_{5-\delta}GeTe_2$ at 1.8 K [insert Figure 4-11] gives a saturation moment μ_{sat} = 1.80 μ_B at 50 kOe and a coercive field of H_c = 325 Oe. The small H_c corresponds to the one of Fe_3GeTe_2 [H_c = 300 Oe] and indicates a soft magnetic material.[11] The small μ_{sat} is in the range of values for ferromagnetic Fe_3GeTe_2 [μ_{sat} = 1.0-1.6 μ_B].[15,24] The saturation moment as well as the Curie temperature of Fe_3GeTe_2 strongly depends on the Fe content.[24,25] The observed suppression of the magnetic ordering was ascribed to a dilution of the central magnetic iron

atoms by vacancies, which is further confirmed by the solid solution $Fe_{3-x}Ni_xGeTe_2$, where the iron atoms are additionally diluted by non magnetic nickel atoms.[24] However, a structural influence is also possible, since it has recently been shown that substitution of the germanium site by arsenic also triggers the suppression of the magnetic ordering without changing the iron content.[37] This is attributed to the increase of the Fe-Fe distances of the Fe atoms sandwiching the FeGe hexagons.

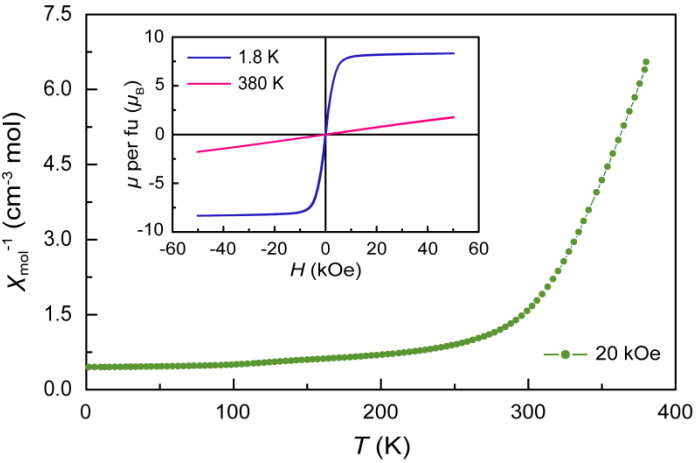

Figure 4-11 Inverse magnetic susceptibility of $Fe_{5-\delta}GeTe_2$ measured at 20 kOe between 1.9 and 380 K [green]. Insert: isothermal magnetization per formula unit at 1.8 K [blue] and 300 K [pink].

The possible suppression of the magnetic ordering in $Fe_{5-\delta}GeTe_2$ with decreasing iron content was examined by substitution with nickel, as targeted syntheses of samples with varying iron deficiency were unsuccessful. $Fe_{5-\delta-x}Ni_xGeTe_2$ samples are stable up to $x = 1.3$, beyond which the proportion of $Fe_{3-x}Ni_xGeTe_2$ increases significantly and binary phases occur in the samples.

Table 4-1 Compositions, lattice parameters, cell volume, ordering temperatures and saturation moments per Fe atom for samples of $Fe_{5-\delta-x}Ni_xGeTe_2$.

x [c]	δ [c]	a (Å)[d]	c (Å)[d]	V (Å^3)	T_C (K)[e]	μ_{sat} (μ_B)[f]
0	0.37(14)	4.0388(3)	29.171(3)	412.08(8)	279(1)	1.80(5)
0.08(1)	0.38(17)	4.0385(1)	29.163(2)	411.91(4)	278(1)	1.90(6)
0.21(2)	0.49(15)	4.0360(1)	29.135(1)	411.00(3)	281(1)	1.97(6)
0.50(4)	0.39(17)	4.0333(1)	29.133(1)	410.43(3)	282(1)	2.11(7)
0.70(5)	0.50(25)	4.0320(1)	29.154(1)	410.45(3)	287(1)	1.73(7)
0.95(5)	0.39(18)	4.0322(2)	29.177(2)	410.81(5)	286(1)	1.58(11)
1.09(13)	0.32(25)	4.0307(1)	29.187(1)	410.65(2)	282(1)	1.53(10)
1.10(9)	0.59(30)	4.0308(1)	29.207(1)	410.96(2)	> 400	1.42(8)
1.29(9)	0.75(29)	4.0294(1)	29.232(2)	411.03(4)	> 400	1.09(12)

Table 4-1 shows the compositions of $Fe_{5-\delta-x}Ni_xGeTe_2$ samples from EDS measurements and lattice parameters from Rietveld refinements [further details are given in Figure A-4 to Figure A-6 and Table A-28]. It is par-

[c] Composition taken from EDS measurement.

[d] Lattice parameters taken from Rietveld refinement of powder diffraction data.

[e] T_C taken from zero points of second derivative of susceptibility measurement at 100 Oe.

[f] μ_{sat} at 50 kOe taken from isothermal magnetization curve at 1.8 K.

ticularly noticeable that no stacking disorder is observed in the powder patterns already above a nickel substitution of $x = 0.2$. It can be argued that this is a consequence of the occupation of an additional nickel site within the van der Waals gap, as in Ni_3GeTe_2.[2] This may affect the crystal growth and direct the stacking of the layers. However, no significant electron density is observed at this position in single crystal measurements of $Fe_{5-\delta-x}Ni_xGeTe_2$. Overall, there is little impact of the substitution on the structure. While the *a* axis decreases continuously with *x*, the *c* axis exhibits a minimum at $x = 0.50$ [Table 4-1]. The maximum difference in the whole range of *x* is small with $\Delta a = 0.2\%$ and $\Delta c = 0.3\%$, and an order of magnitude smaller than the changes found for $Fe_{3-x}Ni_xGeTe_2$.[24] In addition, *c* shows an increase with $x > 0.5$, while for $Fe_{3-x}Ni_xGeTe_2$ the *c* axis decreases with *x*. Here the differences of the structures seem to become evident, since the structure motifs are mainly equal, but Fe_3GeTe_2 does not possess FeFe hexagons. Moreover, no information about the iron sites affected by nickel substitution is obtainable from X-ray diffraction data and therefore a discussion of the influence on the structure is prevented. The trend of the lattice parameters with substitution cannot be compared with structure data of the pure Ni compound as well, since syntheses with corresponding stoichiometry lead to the tetragonal compound $Ni_{5+\delta}GeTe_2$.[50,51] Regarding the composition, it is noticeable, that δ is about 0.4 up to $x = 1.1$ as for the unsubstituted compound. Above that, the number of vacancies increases rapidly. This might be a reason why the structure is not stable for a higher degree of substitution.

Figure 4-12 shows isothermal magnetization curves of the solid solutions $Fe_{5-\delta-x}Ni_xGeTe_2$ at 1.8 K. The saturation moments per Fe atom at 50 kOe are given in Table 4-1 together with T_C from susceptibility measurement at 100 Oe [Figure A-8]. All samples contain $Fe_{3-x}Ni_xGeTe_2$ as

impurity phase, which also contributes to the magnetization. This is included in the error of μ_{sat} in Table 4-1.

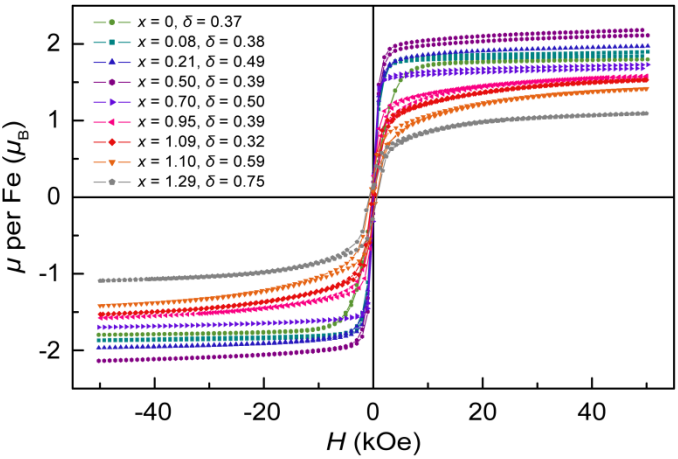

Figure 4-12 Isothermal magnetization per Fe atom at 1.8 K of $Fe_{5-\delta-x}Ni_xGeTe_2$.

In contrast to $Fe_{3-x}Ni_xGeTe_2$ T_C is not reduced with x but remains almost constant up to $x = 1.1$. Samples with $x > 1.1$ and increased δ show no ordering in the measured range, but are already magnetically ordered above 400 K, which is evident from isothermal magnetization curves at this temperature [Figure A-8]. The saturation moments at 1.8 K do not decrease with the Fe content and therefore the dilution of the magnetic centers, but show a maximum at $x = 0.5$ with $\mu_{sat} = 2.11\ \mu_B$. This coincides with the minimum of the c parameter, as can be seen from Figure 4-13.The initial increase of μ_{sat} with x and the dependency of c could be explained by the shortening of the Fe1-Fe2 bonds across the hexagonal FeGe rings with decreasing c. As found for the solid solution $Fe_{3-\delta}Ge_{1-x}As_xTe_2$ this bond length is crucial for the magnetic properties and elongation leads to suppression of the ordering.[37] Thus, for the

magnetic state of $Fe_{5-\delta-x}Ni_xGeTe_2$, the decrease of c and the associated reduction of the Fe1-Fe2 distance dominate up to $x = 0.5$, before the incipient increase of c and the dilution of the magnetic centers prevail.

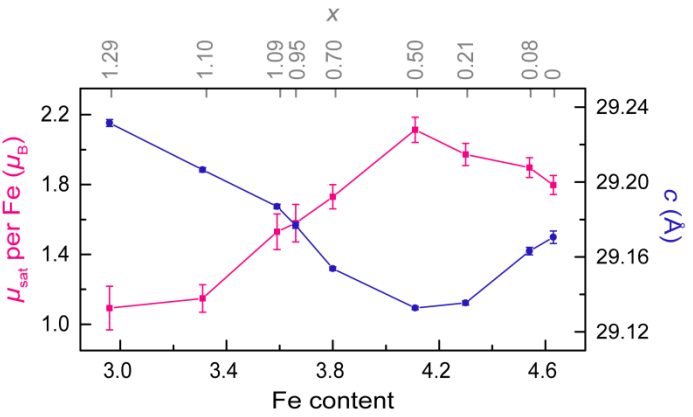

Figure 4-13 Saturation moment μ_{sat} per Fe atom [1.8 K, 50 kOe] and c axis length in dependence of the Fe content for the solid solution $Fe_{5-\delta-x}Ni_xGeTe_2$ [x for each data point is given in grey].

Conclusions

$Fe_{5-\delta}GeTe_2$ is a new van der Waals ferromagnet with a highly anisotropic crystal structure, which is similar to Fe_3GeTe_2 but contains an additional honeycomb layer of iron atoms. Earlier structure determinations were inconclusive because the layer structure tends to form stacking faults. DIFFaX simulations of the disorder are in good agreement with powder diffraction data and suggest the occurrence of both faultless and faulted domains in the crystals. The solid solution $Fe_{5-\delta-x}Ni_xGeTe_2$ was successfully synthesized up to $x = 1.3$, which showed that nickel substitution has little influence on the structure. Ferromagnetic ordering of $Fe_{5-\delta}GeTe_2$ with $T_C = 279$ K and $\mu_{sat} = 1.80\,\mu_B$ changes with x in

$Fe_{5-\delta-x}Ni_xGeTe_2$. While the Curie temperature is hardly affected, the saturation moment exhibits a maximum at 2.11 μ_B in $Fe_{4.11}Ni_{0.50}GeTe_2$. This reflects the interplay of structural effects and dilution of the magnetic centers. Overall, $Fe_{5-\delta}GeTe_2$ exhibits similar promising properties as Fe_3GeTe_2 in terms of application in spintronic devices. The adjustment of μ_{sat} without lowering of T_C through nickel substitution may prove to be an advantage over Fe_3GeTe_2.

4.3 References

1 P. J. Schurer, N. J. G. Hall and A. H. Morrish, *Phys. Rev. B: Condens. Matter* **1978**, *18*, 4860-4874.

2 H.-J. Deiseroth, K. Aleksandrov, C. Reiner, L. Kienle and R. K. Kremer, *Eur. J. Inorg. Chem.* **2006**, *2006*, 1561-1567.

3 D. J. Scalapino, *Rev. Mod. Phys.* **2012**, *84*, 1383-1417.

4 D. J. Scalapino and S. R. White, *Phys. Rev. B: Condens. Matter* **1998**, *58*, 8222-8224.

5 P. Monthoux and G. G. Lonzarich, *Phys. Rev. B: Condens. Matter* **2001**, *63*, 054529.

6 E. Berg, D. Orgad and S. A. Kivelson, *Phys. Rev. B: Condens. Matter* **2008**, *78*, 094509.

7 G. H. Han, D. L. Duong, D. H. Keum, S. J. Yun and Y. H. Lee, *Chem. Rev.* **2018**, *118*, 6297-6336.

8 D. Gao, Q. Xue, X. Mao, W. Wang, Q. Xu and D. Xue, *J. Mater. Chem. C* **2013**, *1*, 5909-5916.

9 M. Bonilla, S. Kolekar, Y. Ma, H. C. Diaz, V. Kalappattil, R. Das, T. Eggers, H. R. Gutierrez, M.-H. Phan and M. Batzill, *Nat. Nanotechnol.* **2018**, *13*, 289-293.

10 N. D. Mermin and H. Wagner, *Phys. Rev. Lett.* **1966**, *17*, 1133-1136.

11 N. León-Brito, E. D. Bauer, F. Ronning, J. D. Thompson and R. Movshovich, *J. Appl. Phys.* **2016**, *120*, 083903.

12 B. Chen, J. Yang, H. Wang, M. Imai, H. Ohta, C. Michioka, K. Yoshimura and M. Fang, *J. Phys. Soc. Jpn.* **2013**, *82*, 124711.

13 Y. Wang, C. Xian, J. Wang, B. Liu, L. Ling, L. Zhang, L. Cao, Z. Qu and Y. Xiong, *Phys. Rev. B: Condens. Matter* **2017**, *96*, 134428.

14 G. D. Nguyen, J. Lee, T. Berlijn, Q. Zou, S. M. Hus, J. Park, Z. Gai, C. Lee and A.-P. Li, *Phys. Rev. B: Condens. Matter* **2018**, *97*, 014425.

15 V. Y. Verchenko, A. A. Tsirlin, A. V. Sobolev, I. A. Presniakov and A. V. Shevelkov, *Inorg. Chem.* **2015**, *54*, 8598-8607.

16 Q. Mao, B. Chen, J. Yang, Y. Zhang, H. Wang and M. Fang, *J. Phys.: Condens. Matter* **2018**, *30*, 345802.

17 M. Quintero, D. Ferrer, D. Caldera, E. Moreno, E. Quintero, M. Morocoima, P. Grima, P. Bocaranda, G. E. Delgado and J. A. Henao, *J. Alloys Compd.* **2009**, *469*, 4-8.

18 G. Delgado, L. Betancourt, A. J. Mora, J. E. Contreras, P. Gallardo and M. Quintero, *Chalcogenide Lett.* **2010**, *7*, 133-138.

19 APEX2, v2014.11-0, Bruker AXS Inc., Madison, Wisconsin, USA, **2014**.

20 V. Petříček, M. Dušek and L. Palatinus, *Z. Kristallogr. - Cryst. Mater.* **2014**, *229*, 345-352.

21 TOPAS-Academic, V5, Coelho Software, Brisbane, Australia, **2007**.

22 QUANTAX 200, 1.9.4.3448, Bruker Nano GmbH, Berlin, Germany, **2013**.

23 SmartSEM, 5.07 Beta, Carl Zeiss Microscopy Ltd., Cambridge, UK, **2014**.

24 J. Stahl, V. Pomjakushin and D. Johrendt, *Z. Naturforsch., B: Chem. Sci.* **2016**, *71*, 273.

25 A. F. May, S. Calder, C. Cantoni, H. Cao and M. A. McGuire, *Phys. Rev. B: Condens. Matter* **2016**, *93*, 014411.

26 D. L. Duong, S. J. Yun and Y. H. Lee, *ACS Nano* **2017**, *11*, 11803-11830.

27 K. S. Novoselov, D. Jiang, F. Schedin, T. J. Booth, V. V. Khotkevich, S. V. Morozov and A. K. Geim, *PNAS USA* **2005**, *102*, 10451-10453.

28 W. Hu and J. Yang, *J. Mater. Chem. C* **2017**, *5*, 12289-12297.

29 C. Gong, L. Li, Z. Li, H. Ji, A. Stern, Y. Xia, T. Cao, W. Bao, C. Wang, Y. Wang, Z. Q. Qiu, R. J. Cava, S. G. Louie, J. Xia and X. Zhang, *Nature* **2017**, *546*, 265-269.

30 C. Tan, J. Lee, S.-G. Jung, T. Park, S. Albarakati, J. Partridge, M. R. Field, D. G. McCulloch, L. Wang and C. Lee, *Nat. Commun.* **2018**, *9*, 1554.

31 J.-U. Lee, S. Lee, J. H. Ryoo, S. Kang, T. Y. Kim, P. Kim, C.-H. Park, J.-G. Park and H. Cheong, *Nano Lett.* **2016**, *16*, 7433-7438.

32 Y. Liu, E. Stavitski, K. Attenkofer and C. Petrovic, *Phys. Rev. B: Condens. Matter* **2018**, *97*, 165415.

33 Q. Li, M. Yang, C. Gong, R. V. Chopdekar, A. T. N'Diaye, J. Turner, G. Chen, A. Scholl, P. Shafer, E. Arenholz, A. K. Schmid, S. Wang, K. Liu, N. Gao, A. S. Admasu, S.-W. Cheong, C. Hwang, J. Li, F. Wang, X. Zhang and Z. Qiu, *Nano Lett.* **2018**, *18*, 5974-5980.

34 J. Yi, H. Zhuang, Q. Zou, Z. Wu, G. Cao, S. Tang, S. A. Calder, P. R. C. Kent, D. Mandrus and Z. Gai, *2D Mater.* **2017**, *4*, 011005.

35 H. L. Zhuang, P. R. C. Kent and R. G. Hennig, *Phys. Rev. B: Condens. Matter* **2016**, *93*, 134407.

36 J.-X. Zhu, M. Janoschek, D. S. Chaves, J. C. Cezar, T. Durakiewicz, F. Ronning, Y. Sassa, M. Mansson, B. L. Scott, N. Wakeham, E. D. Bauer and J. D. Thompson, *Phys. Rev. B: Condens. Matter* **2016**, *93*, 144404.

37 D. Yuan, S. Jin, N. Liu, S. Shen, Z. Lin, K. Li and X. Chen, *Mater. Res. Express* **2017**, *4*, 036103.

38 V. Y. Verchenko, S. S. Sokolov, A. A. Tsirlin, A. V. Sobolev, I. A. Presniakov, M. A. Bykov, M. A. Kirsanova and A. V. Shevelkov, *Dalton Trans.* **2016**, *45*, 16938-16947.

39 A. A. Isaeva, O. N. Makarevich, A. N. Kuznetsov, T. Doert, A. M. Abakumov and G. Van Tendeloo, *Eur. J. Inorg. Chem.* **2010**, *2010*, 1395-1404.

40 A. K. Larsson, L. Noren, R. L. Withers and H. Rundlöf, *J. Solid State Chem.* **2007**, *180*, 2723-2733.

41 H.-J. Deiseroth, F. Spirovski, C. Reiner and M. Schlosser, *Z. Kristallogr. - New Cryst. Struct.* **2007**, *222*, 169-170.

42 T. K. Reynolds, R. F. Kelley and F. J. DiSalvo, *J. Alloys Compd.* **2004**, *366*, 136-144.

43 O. N. Litvinenko, A. N. Kuznetsov, A. V. Olenev and B. A. Popovkin, *Russ. Chem. Bull.* **2007**, *56*, 1945-1947.

44 J. Stahl, L. Neudert, O. Oeckler and D. Johrendt, *Z. Anorg. Allg. Chem.* **2016**, *642*, 989-996.

45 F. Spirovski, C. Reiner, H.-J. Deiseroth, L. Kienle and H. Mikus, *Z. Anorg. Allg. Chem.* **2006**, *632*, 2103-2103.

46 M. M. J. Treacy, J. M. Newsam and M. W. Deem, *Proc. R. Soc. London, Ser. A* **1991**, *433*, 499-520.

47 A. W. Hull, *Physical Review* **1919**, *14*, 540-541.

48 M. Ruck and A. Simon, *Z. Anorg. Allg. Chem.* **1993**, *619*, 327-336.

49 R. Reisser, R. K. Kremer and A. Simon, *Physica B* **1995**, *204*, 265-273.

50 H.-J. Deiseroth, F. Spirovski, C. Reiner and M. Schlosser, *Z. Kristallogr. - New Cryst. Struct.* **2007**, *222*, 171-172.

51 A. A. Isaeva, A. I. Baranov, T. Doert, M. Ruck, V. A. Kulbachinskii, R. A. Lunin and B. A. Popovkin, *Russ. Chem. Bull.* **2007**, *56*, 1694-1700.

5 Summary

In this thesis two different classes of quasi-two-dimensional transition metal chalcogenides were investigated. In the first part *β*-FeSe and related structures were synthesized *via* a solvothermal method. This method provides on the one hand a unique tool to incorporate organic molecules into the product structures. On the other hand it represents an alternative synthesis method for inorganic compounds difficult to access by solid state reactions. This thesis focused on both, the targeted control of the parameter-rich solvothermal method, as well as the increase in structural range of dimensionally reduced phases. *β*-FeSe represents an intriguing compound, since the nature of the superconducting state is not yet fully understood. In the second part of the thesis Fe_3GeTe_2-related materials were successfully prepared with the main focus on expanding the substance group, since Fe_3GeTe_2 has recently attracted a lot of research interest due to its promising magnetic properties for device application.

_β_-FeSe-related structures

In chapter 2 of this thesis the field of dimensionally reduced *β*-FeSe-related structures was successfully extended by four compounds with differently terminated fragments. Solvothermal synthesis was used for this purpose, with the solvent *en* being incorporated into the product structures. This yields organic-inorganic hybrid compounds, in which the quasi-low-dimensional character is more pronounced since the van der Waals interactions between the FeSe-related structure motifs are weakened. In order to achieve a systematic stepwise dimensional reduction a novel control parameter was established, using an additional sol-

vent as diluent. Thus, depending on the degree of dilution, various one- and two-dimensional products were prepared.

Dilution with *glycerol* yields $Fe_3Se_4(en)_3$ in addition to the previously discovered compound $Fe_3Se_4(en)_2$ with both containing quasi-1D single chains of edge-sharing $FeSe_4$ tetrahedra.[1] The new compound crystallizes in two polymorphs, which mainly differ in the distortion of the $FeSe_2$ chains. In contrast to $Fe_3Se_4(en)_2$ no Fe-Se interactions, but only hydrogen bonds connect the chains resulting in a more pronounced one-dimensional character. $Fe_{10}Se_{12}(en)_7$ is also built up from chains, but the connection of the tetrahedra *via* three edges results in Fe_2Se_3 double chains. $Fe_3Se_4(en)_3$ and $Fe_{10}Se_{12}(en)_7$ both contain $Fe(en)_3$ complexes arranged between the chains. With $Fe_{0.85}Se(en)_{0.3}$ a quasi-two-dimensional compound with neutral spacer layers was synthesized. Despite the small quantity of intercalated *en*, the FeSe layers are widely separated in the new structure. Differences to β-FeSe are mainly evident in the stacking sequence and stoichiometry of the layers.

In addition to determination of the crystallographic structures, the stability ranges of the β-FeSe-related compounds as a function of dilution and synthesis temperature were investigated. The generated phase diagram demonstrates a strong dependence of the product dimensionality on the dilution. Further characterization of the products regarding their thermal stability showed decomposition of $Fe_3Se_4(en)_2$, $Fe_3Se_4(en)_3$ and $Fe_{10}Se_{12}(en)_7$ between 100 °C and 150 °C into elements or various iron selenides. The measurements additionally suggest a phase transition of β-$Fe_3Se_4(en)_3$ to the α-polymorph prior to decomposition. $Fe_{0.85}Se(en)_{0.3}$ also undergoes a phase transition above 180 °C, in which the crystal system changes from monoclinic to orthorhombic. This resembles the tetragonal-to-orthorhombic transition of β-FeSe upon cooling.[2] The

transition in $Fe_{0.85}Se(en)_{0.3}$ is accompanied by deintercalation of *en*, which is completed above 200 °C, resulting in *β*-FeSe. Investigation of the magnetic properties showed paramagnetic behavior for $Fe_3Se_4(en)_3$ and $Fe_{10}Se_{12}(en)_7$ with potential indication of antiferromagnetic ordering. In contrast to similar compounds additionally intercalated by alkali metals, $Fe_{0.85}Se(en)_{0.3}$ is also paramagnetic and non-superconducting.[3-6] More detailed characterization implied that this is due to the lack of electron doping. A similar scenario is assumed for *β*-FeSe monolayers grown on $SrTiO_3$.[7] Thus, with $Fe_{0.85}Se(en)_{0.3}$ a bulk analogue of the monolayer material and a parent compound of the metal co-intercalated structures was successfully prepared.

Since solvothermal synthesis provides multiple additional parameters in comparison to conventional solid state synthesis, careful investigations of their dependencies are mandatory.[8] In order to confirm the capability of the new control parameter to gradually generate dimensionally reduced phases, further syntheses with an alternative diluent were conducted. Methanol was chosen, since the influence on the reaction pressure is reversed compared to *glycerol*. As a consequence, the new compound $Fe_{20}Se_{24}(en)_{13}(MeOH)$ was found, exhibiting an unusual crystal structure with Fe_2Se_3 double chains. Itemized studies of the reaction pressure for both diluents, *glycerol* and methanol, overall corroborated the dependence of the tetrahedra connectivity upon the degree of dilution. Thus, in this chapter, the structural diversity of low-dimensional *β*-FeSe-related structures was expanded and at the same time additional control was gained over the solvothermal method.

β-FeSe

In addition to dimensionally reduced structures, *β*-FeSe itself was produced by a solvothermal method in *1,3-dap* and *glycerol*. This combination of solvent and diluent yields a superconducting product, which is remarkable considering previously discussed problems with solvent-based syntheses of *β*-FeSe.[9-14] Mainly, a differing iron environment and contamination with oxygen atoms are mentioned as possible reasons for the absent transition to the superconducting state in these materials.[12-14] Therefore, the synthesized product was examined in detail in chapter 3 with regard to its chemical and physical properties at ambient and low temperatures. In order to improve the assessment of the correlations, *β*-FeSe was supplementarily prepared by a hydrothermal route as well as vapor-transport, and equally investigated. All samples exhibited almost identical crystal structures and stoichiometries at room temperature. Nevertheless, at low temperatures their behavior differs significantly. While the transport grown sample showed usual superconductivity and a tetragonal-to-orthorhombic phase transition, the hydrothermally produced sample is neither superconducting nor exhibits a structural transition. The product synthesized in *1,3-dap* and *glycerol*, on the other hand, shows no phase transition either, but is superconducting. As both properties are associated with nematic fluctuations, a separate occurrence is astonishing. Even a phase separation on the macroscopic or microscopic scale in the solvothermally synthesized material is conceivable. Overall, the chapter describes a simple synthesis route for superconducting *β*-FeSe by a solvothermal method. The almost contradictory properties of the product furthermore provide a basis for further investigations of the actual nature of the superconducting state.

Fe_3GeTe_2-related structures

The last part of this thesis is concerned with another quasi-two-dimensional transition metal chalcogenide, Fe_3GeTe_2. The compound has been intensively studied since it was first mentioned in 2006 until today.[15] The most important finding was presumably the fabrication of two-dimensional magnets by isolation of monolayers from the ferromagnetic bulk material.[16] Additional gate-tuning raises the transition temperature even above room temperature, making application in magnetoelectronic devices a very promising possibility. Nevertheless, no other quasi-2D compounds in the Fe-Ge-Te system have been found until that point. In chapter 4 of this thesis, the two new materials $Fe_{2.3}GeTe$ and $Fe_{5-\delta}GeTe_2$ were synthesized by solid state reaction. Crystal structure solution revealed similar structural motifs to Fe_3GeTe_2. All three compounds can be described as variants of the Fe_2Ge structure cut by a van der Waals gap built of Te atoms. While in Fe_3GeTe_2 a total of three atomic Fe or FeGe layers are located between the gap, there are four in $Fe_{5-\delta}GeTe_2$ and five in $Fe_{2.3}GeTe$. $Fe_{5-\delta}GeTe_2$ furthermore contains rare layers of FeFe hexagons comprising very short Fe-Fe distances. Both new compounds exhibit stacking disorder due to their pronounced quasi-two-dimensional character. With transmission electron microscopy and X-ray data simulation *via* DIFFaX, two different methods were used in this thesis to investigate the stacking. SAED and HRTEM measurements attributed the disorder in $Fe_{2.3}GeTe$ to in-plane ordering of Fe vacancies and non-periodic stacking of the single crystals. For $Fe_{5-\delta}GeTe_2$ the stacking faults were located in domains through measurement and simulation of powder X-ray diffraction patterns. $Fe_{2.3}GeTe$ and $Fe_{5-\delta}GeTe_2$ are ferromagnetic below 241 K and 279 K, respectively. Due to their highly anisotropic structures they are, like Fe_3GeTe_2, promising materials for exfoliation to 2D magnets and corresponding applica-

tion in electronic devices. This potential has recently been demonstrated for $Fe_{5-\delta}GeTe_2$.[17] It may therefore provide a benefit that the magnetic saturation moment can be tuned by Ni substitution without significant impact on T_C, as additionally presented in chapter 4 for the solid solution $Fe_{5-\delta-x}Ni_xGeTe_2$.

1 C. Pak, S. Kamali, J. Pham, K. Lee, J. T. Greenfield and K. Kovnir, *J. Am. Chem. Soc.* **2013**, *135*, 19111-19114.

2 S. Margadonna, Y. Takabayashi, M. T. McDonald, K. Kasperkiewicz, Y. Mizuguchi, Y. Takano, A. N. Fitch, E. Suard and K. Prassides, *Chem. Commun.* **2008**, 5607-5609.

3 T. Hatakeda, T. Noji, S. Hosono, T. Kawamata, M. Kato and Y. Koike, *JPCS* **2014**, *568*, 022032.

4 T. Hatakeda, T. Noji, T. Kawamata, M. Kato and Y. Koike, *J. Phys. Soc. Jpn.* **2013**, *82*, 123705.

5 T. Noji, T. Hatakeda, S. Hosono, T. Kawamata, M. Kato and Y. Koike, *Physica C* **2014**, *504*, 8-11.

6 S. Jin, X. Fan, X. Wu, R. Sun, H. Wu, Q. Huang, C. Shi, X. Xi, Z. Li and X. Chen, *Chem. Commun.* **2017**, *53*, 9729-9732.

7 Y. Miyata, K. Nakayama, K. Sugawara, T. Sato and T. Takahashi, *Nat. Mater.* **2015**, *14*, 775-779.

8 G. Demazeau, *J. Mater. Sci.* **2008**, *43*, 2104-2114.

9 K. D. Oyler, X. Ke, I. T. Sines, P. Schiffer and R. E. Schaak, *Chem. Mater.* **2009**, *21*, 3655-3661.

10 S. J. Li, D. Li, J. J. Jiang, G. B. Liu, S. Ma, W. Liu and Z. D. Zhang, *J. Appl. Phys.* **2014**, *115*, 17B502.

11 D. Li, D. Pan, W. Liu, X. Li, M. Chen, S. Li, Y. Li, J. Tan, D. Sun, Z. Wang, Z. Han and Z. Zhang, *Chem. Mater.* **2017**, *29*, 842-848.

12 U. Pachmayr, N. Fehn and D. Johrendt, *Chem. Commun.* **2016**, *52*, 194-197.

13 F. Nitsche, T. Goltz, H. H. Klauss, A. Isaeva, U. Müller, W. Schnelle, P. Simon, T. Doert and M. Ruck, *Inorg. Chem.* **2012**, *51*, 7370-7376.

14 J. T. Greenfield, S. Kamali, K. Lee and K. Kovnir, *Chem. Mater.* **2015**, *27*, 588-596.

15 H.-J. Deiseroth, K. Aleksandrov, C. Reiner, L. Kienle and R. K. Kremer, *Eur. J. Inorg. Chem.* **2006**, *2006*, 1561-1567.

16 Y. Deng, Y. Yu, Y. Song, J. Zhang, N. Z. Wang, Z. Sun, Y. Yi, Y. Z. Wu, S. Wu, J. Zhu, J. Wang, X. H. Chen and Y. Zhang, *Nature* **2018**, *563*, 94-99.

17 A. F. May, D. Ovchinnikov, Q. Zheng, R. Hermann, S. Calder, B. Huang, Z. Fei, Y. Liu, X. Xu and M. A. McGuire, *ACS Nano* **2019**, *13*, 4436-4442.

A Appendix

A.1 Systematic dimensional reduction of the layered β-FeSe structure by solvothermal synthesis

Crystal structures

Table A-1 to Table A-5 show the data for the crystal structure solutions of $Fe_{10}Se_{12}(en)_7$ and $Fe_3Se_4(en)_3$.

Table A-1 Crystal data, data collection parameters and refinement parameters for $Fe_{10}Se_{12}(en)_7$ and $Fe_3Se_4(en)_3$.

	$Fe_{10}Se_{12}(en)_7$	$Fe_3Se_4(en)_3$
Crystal data		
Chemical formula	$Fe_{10}Se_{12}C_{14}H_{56}N_{14}$	$Fe_3Se_4C_6H_{24}N_6$
M (g·mol^{-1})	1926.7	663.7
Crystal system, Space group (No.)	Monoclinic, $P2_1/n$ (14)	Triclinic; $P\bar{1}$ (2)
a, b, c (Å)	9.323(2), 12.273(2), 20.821(4)	9.104(4), 10.398(4), 11.675(5)
α, β, γ (°)	90, 90, 90	109.880(13), 96.370(15), 114.093(14)
V (Å^3), ρ_{calc} (g·cm^{-3})	2382.4(8), 2.686	907.8(7), 2.428
T (K), μ (mm^{-1})	120, 12.15	293, 10.38
Z	2	2
Radiation type	Mo-K_α (λ = 0.71073 Å)	Mo-K_α (λ = 0.71073 Å)
θ range (°)	4.8-53.2	4.7-35.5

Table A-1 Continued.

	$Fe_{10}Se_{12}(en)_7$	$Fe_3Se_4(en)_3$
Data collection		
Diffractometer, Monochromator	Bruker CCD diffractometer, graphite	Bruker CCD diffractometer, graphite
Absorption correction	multi-scan *SADABS* 2014/5	multi-scan *SADABS* 2014/5
No. of reflections (measured, independent, with I>3$\sigma(I)$)	42237, 4294, 3334	37683, 3280, 2424
R_{int}	0.058	0.100
Index range	-12 ≤ *h* ≤ 12, -14 ≤ *k* ≤ 16, -27 ≤ *l* ≤ 27	-12 ≤ *h* ≤ 12, -13 ≤ *k* ≤ 13, -15 ≤ *l* ≤ 15
θ range (°)	2.4-28.6	2.3-28.5
Refinement		
Refinement on	F^2	F^2
Data, Restraints, Parameters, Constraints	4294, 0, 226, 119	3280, 0, 172, 102
R_1 (I>2$\sigma(I)$), $wR(F^2)$ (I>2$\sigma(I)$)	0.033, 0.071	0.038, 0.072
Goodness of fit on F^2	1.69	1.56
$\Delta\rho$ (max; min) (e·Å^{-3})	0.98; -1.08	0.84; -0.84

Table A-2 Fractional atomic coordinates and isotropic or equivalent isotropic displacement parameters (Å^2) for $Fe_{10}Se_{12}(en)_7$.

Atom	*x*	*y*	*z*	U_{iso}*/U_{eq}
Se1	0.77140(6)	0.93036(5)	0.12391(3)	0.02419(19)
Se2	0.85492(6)	0.40006(5)	0.03729(3)	0.02412(19)
Se3	0.11796(6)	0.88151(4)	0.03094(3)	0.01944(18)
Se4	0.76490(6)	0.69621(5)	0.99923(3)	0.02219(18)

Table A-2 Continued.

Atom	*x*	*y*	*z*	U_{iso}*/U_{eq}
Se5	0.99674(7)	0.64847(5)	0.14486(3)	0.0288(2)
Se6	0.93985(7)	0.85096(5)	0.86411(3)	0.0260(2)
Fe1	0.90711(9)	0.79092(6)	0.07937(4)	0.0198(3)
Fe2	0.94844(9)	0.58040(6)	0.04005(4)	0.0199(3)
Fe3	0.95131(9)	0.02130(6)	0.06705(4)	0.0197(3)
Fe4	0.99098(9)	0.75666(6)	0.95840(4)	0.0193(3)
Fe5	0.45243(9)	0.42641(7)	0.18158(4)	0.0261(3)
N1	0.4521(6)	0.60599(9)	0.19970(17)	0.043(2)
N2	0.4758(3)	0.4916(2)	0.08256(9)	0.0344(19)
N3	0.3853(2)	0.3987(3)	0.28151(6)	0.0311(18)
N4	0.21578(13)	0.4177(3)	0.16990(10)	0.0306(18)
N5	0.4870(3)	0.24995(11)	0.1676(2)	0.051(2)
N6	0.68602(15)	0.4163(2)	0.20335(19)	0.041(2)
N7	0.4303(6)	0.06143(16)	0.0768(2)	0.069(3)
C1	0.5133(7)	0.6590(5)	0.1416(3)	0.043(3)
C2	0.4422(6)	0.6097(5)	0.08454(19)	0.039(2)
C3	0.2348(8)	0.3792(9)	0.2812(2)	0.150(7)
C4	0.1513(4)	0.4124(6)	0.2330(3)	0.061(3)
C5	0.6462(7)	0.2344(4)	0.1631(3)	0.045(3)
C6	0.7244(5)	0.3022(6)	0.2091(3)	0.050(3)
C7	0.4977(7)	0.0560(5)	0.0156(3)	0.049(3)
H1n1	0.510766	0.629146	0.23993	0.0512*
H2n1	0.345824	0.629951	0.205316	0.0512*
H1n2	0.415562	0.454569	0.046631	0.0413*
H2n2	0.58438	0.481009	0.073014	0.0413*
H1n3	0.436756	0.33644	0.306372	0.0374*
H2n3	0.406264	0.472794	0.30385	0.0374*
H1n4	0.172051	0.482695	0.144506	0.0368*
H2n4	0.195726	0.345503	0.14536	0.0368*
H1n5	0.440502	0.235022	0.123091	0.0612*
H2n5	0.445073	0.196092	0.201339	0.0612*

Table A-2 Continued.

Atom	*x*	*y*	*z*	U_{iso}*/U_{eq}
H1n6	0.702192	0.455067	0.247175	0.049*
H2n6	0.74966	0.452857	0.168435	0.049*
H1n7	0.503517	0.089391	0.110717	0.0833*
H2n7	0.343562	0.114577	0.074623	0.0833*
H1c1	0.628282	0.643295	0.139485	0.0519*
H2c1	0.490702	0.746111	0.143017	0.0519*
H1c2	0.326484	0.620857	0.088239	0.0472*
H2c2	0.482091	0.648682	0.041016	0.0472*
H1c3	0.21437	0.293373	0.290961	0.1795*
H2c3	0.188844	0.405985	0.326726	0.1795*
H1c4	0.104481	0.491252	0.244894	0.0737*
H2c4	0.055269	0.361928	0.231049	0.0737*
H1c5	0.672258	0.148938	0.171287	0.0546*
H2c5	0.681859	0.253446	0.114514	0.0546*
H1c6	0.701903	0.274205	0.257757	0.06*
H2c6	0.839392	0.292721	0.201409	0.06*
H1c7	0.606155	0.088585	0.019117	0.0585*
H2c7	0.44655	0.113715	0.983101	0.0585*

Table A-3 Atomic displacement parameters (Å^2) for $Fe_{10}Se_{12}(en)_7$.

Atom	U_{11}	U_{22}	U_{33}	U_{12}	U_{13}	U_{23}
Se1	0.0283(3)	0.0210(3)	0.0233(3)	0.0008(3)	0.0074(3)	-0.0006(3)
Se2	0.0257(3)	0.0165(3)	0.0301(3)	-0.0007(3)	0.0094(3)	0.0005(3)
Se3	0.0222(3)	0.0180(3)	0.0181(3)	-0.0002(3)	0.0005(2)	0.0004(2)
Se4	0.0236(3)	0.0212(3)	0.0218(3)	-0.0019(3)	0.0022(3)	-0.0015(3)
Se5	0.0463(4)	0.0210(3)	0.0190(3)	0.0041(3)	-0.0014(3)	0.0014(3)
Se6	0.0387(4)	0.0232(3)	0.0160(3)	-0.0045(3)	-0.0016(3)	0.0008(3)
Fe1	0.0259(5)	0.0163(4)	0.0172(4)	0.0006(4)	0.0032(4)	0.0003(3)
Fe2	0.0256(5)	0.0160(4)	0.0181(4)	-0.0003(4)	0.0048(4)	0.0001(3)

Table A-3 Continued.

Atom	U_{11}	U_{22}	U_{33}	U_{12}	U_{13}	U_{23}
Fe3	0.0262(5)	0.0156(4)	0.0174(4)	-0.0003(4)	0.0014(4)	0.0003(3)
Fe4	0.0252(5)	0.0164(4)	0.0164(4)	-0.0015(4)	0.0025(4)	0.0002(3)
Fe5	0.0274(5)	0.0284(5)	0.0226(5)	0.0026(4)	-0.0021(4)	-0.0033(4)
N1	0.070(4)	0.032(3)	0.026(3)	-0.010(3)	0.010(3)	0.000(3)
N2	0.031(3)	0.049(4)	0.023(3)	-0.004(3)	-0.002(2)	-0.007(3)
N3	0.032(3)	0.031(3)	0.030(3)	-0.006(2)	-0.002(2)	0.006(2)
N4	0.029(3)	0.038(3)	0.025(3)	0.002(2)	-0.009(2)	-0.001(2)
N5	0.056(4)	0.039(4)	0.059(4)	0.001(3)	0.016(3)	-0.013(3)
N6	0.030(3)	0.062(4)	0.030(3)	0.007(3)	0.006(3)	0.012(3)
N7	0.043(4)	0.083(5)	0.082(5)	0.003(4)	-0.002(4)	-0.031(4)
C1	0.052(5)	0.043(4)	0.035(4)	-0.006(4)	0.013(3)	0.006(3)
C2	0.029(4)	0.062(5)	0.027(4)	-0.011(4)	-0.002(3)	0.010(3)
C3	0.041(6)	0.37(2)	0.035(5)	-0.069(9)	-0.008(4)	0.051(8)
C4	0.034(4)	0.111(8)	0.040(4)	0.008(5)	0.006(4)	0.027(5)
C5	0.044(4)	0.037(4)	0.056(5)	0.010(4)	0.024(4)	-0.003(4)
C6	0.052(5)	0.055(5)	0.042(4)	0.013(4)	0.004(4)	0.000(4)
C7	0.031(4)	0.066(5)	0.049(5)	0.010(4)	-0.007(3)	-0.018(4)

Table A-4 Fractional atomic coordinates and isotropic or equivalent isotropic displacement parameters (Å^2) for $Fe_3Se_4(en)_3$.

Atom	*x*	*y*	*z*	U_{iso}*/U_{eq}
Se1	0.13526(8)	0.74158(7)	0.33777(6)	0.0249(3)
Se2	0.76829(8)	0.35087(7)	0.18216(6)	0.0284(3)
Se3	0.87130(8)	0.59483(7)	0.98113(6)	0.0257(3)
Se4	0.85343(8)	0.57306(8)	0.54767(6)	0.0282(3)
Fe1	0.98106(10)	0.52543(9)	0.12988(8)	0.0198(4)
Fe2	0.97611(11)	0.52367(9)	0.38322(8)	0.0209(4)
Fe3	0.66239(11)	0.88136(10)	0.24881(8)	0.0267(4)

Table A-4 Continued.

Atom	*x*	*y*	*z*	U_{iso}*/U_{eq}
N1	0.6610(3)	0.10858(14)	0.3256(3)	0.030(3)
N2	0.41219(18)	0.8168(2)	0.1413(3)	0.033(3)
N3	0.5870(5)	0.8456(2)	0.4131(2)	0.030(3)
N4	0.6037(6)	0.63463(13)	0.19656(14)	0.049(4)
N5	0.7703(4)	0.9194(2)	0.09406(15)	0.040(3)
N6	0.93694(14)	0.9979(4)	0.34486(15)	0.038(3)
C1	0.4897(9)	0.0816(5)	0.2853(6)	0.038(4)
C2	0.4062(5)	0.9597(7)	0.1500(6)	0.035(4)
C3	0.6015(8)	0.7120(8)	0.4181(6)	0.043(4)
C4	0.5258(9)	0.5829(5)	0.2884(6)	0.043(4)
C5	0.9439(9)	0.0506(8)	0.1552(5)	0.044(4)
C6	0.0332(5)	0.0185(8)	0.2511(6)	0.043(4)
H1n1	0.711662	0.176956	0.423205	0.0363*
H2n1	0.733733	0.165473	0.278053	0.0363*
H1n2	0.367751	0.736909	0.046421	0.04*
H2n2	0.337443	0.768982	0.192376	0.04*
H1n3	0.655531	0.941941	0.500158	0.036*
H2n3	0.461276	0.819483	0.394196	0.036*
H1n4	0.512961	0.580973	0.109347	0.0593*
H2n4	0.698706	0.604534	0.185081	0.0593*
H1n5	0.69875	0.948888	0.042567	0.0476*
H2n5	0.773238	0.82126	0.033008	0.0476*
H1n6	0.965726	0.933208	0.385647	0.0453*
H2n6	0.96936	0.106329	0.415612	0.0453*
H1c1	0.492512	0.189555	0.291245	0.0451*
H2c1	0.419493	0.041444	0.346932	0.0451*
H1c2	0.275584	0.933932	0.121519	0.0416*
H2c2	0.472478	0.00239	0.08776	0.0416*
H1c3	0.534642	0.674665	0.482229	0.0515*
H2c3	0.73376	0.745087	0.451608	0.0515*

Table A-4 Continued.

Atom	*x*	*y*	*z*	U_{iso}*/U_{eq}
H1c4	0.544052	0.486078	0.289816	0.0512*
H2c4	0.391059	0.542488	0.258467	0.0512*
H1c5	0.939579	0.158306	0.20412	0.053*
H2c5	0.009513	0.058085	0.083134	0.053*
H1c6	0.041162	0.912857	0.201805	0.0522*
H2c6	0.159459	0.116181	0.30098	0.0522*

Table A-5 Atomic displacement parameters (Å^2) for $Fe_3Se_4(en)_3$.

Atom	U_{11}	U_{22}	U_{33}	U_{12}	U_{13}	U_{23}
Se1	0.0269(4)	0.0177(3)	0.0177(3)	0.0017(3)	0.0026(3)	0.0062(3)
Se2	0.0261(4)	0.0251(4)	0.0179(3)	-0.0011(3)	0.0010(3)	0.0098(3)
Se3	0.0318(4)	0.0275(4)	0.0211(3)	0.0172(3)	0.0071(3)	0.0105(3)
Se4	0.0342(4)	0.0347(4)	0.0235(4)	0.0210(3)	0.0113(3)	0.0142(3)
Fe1	0.0207(5)	0.0179(5)	0.0144(4)	0.0049(4)	0.0028(4)	0.0060(4)
Fe2	0.0232(5)	0.0188(5)	0.0154(4)	0.0058(4)	0.0034(4)	0.0072(4)
Fe3	0.0285(5)	0.0260(5)	0.0208(5)	0.0095(4)	0.0062(4)	0.0094(4)
N1	0.034(3)	0.022(3)	0.019(3)	0.003(3)	-0.001(2)	0.006(2)
N2	0.031(3)	0.027(3)	0.021(3)	0.000(3)	-0.002(2)	0.007(2)
N3	0.035(3)	0.033(3)	0.019(3)	0.013(3)	0.008(2)	0.012(2)
N4	0.070(5)	0.043(4)	0.049(4)	0.034(4)	0.028(4)	0.021(3)
N5	0.048(4)	0.044(4)	0.028(3)	0.024(3)	0.013(3)	0.012(3)
N6	0.032(3)	0.040(4)	0.041(4)	0.016(3)	0.008(3)	0.019(3)
C1	0.046(5)	0.035(4)	0.032(4)	0.018(4)	0.018(3)	0.013(3)
C2	0.025(4)	0.043(4)	0.036(4)	0.013(3)	0.010(3)	0.021(3)
C3	0.055(5)	0.046(5)	0.041(4)	0.025(4)	0.020(4)	0.030(4)
C4	0.054(5)	0.030(4)	0.045(5)	0.021(4)	0.013(4)	0.017(4)
C5	0.058(5)	0.044(5)	0.036(4)	0.022(4)	0.033(4)	0.020(4)
C6	0.034(4)	0.038(4)	0.052(5)	0.016(4)	0.013(4)	0.013(4)

Table A-6 and Table A-7 show the data for the Rietveld refinement of the powder diffraction data of FeSe(*en*)$_{0.3}$. Positions of the C, N, and H atoms [*en* molecules] were taken from rigid body refinement, isotropic displacement factors were set to 3 and 5, respectively, and site occupation factors were set to one third in accordance with the chemical analysis.

Table A-6 Crystal data, data collection parameters and refinement parameters for FeSe(*en*)$_{0.3}$.

Crystal data	
Chemical formula	$Fe_{0.85}SeC_{0.6}H_{2.4}N_{0.6}$
M (g·mol^{-1})	144.46
Crystal system, Space group (No.)	Monoclinic, $C2/c$ (15)
a, b, c (Å)	3.9037(5), 21.528(2), 3.8585(6)
α, β, γ (°)	90, 91.34(2), 90
V (Å^3)	324.17(8)
Z	4
Radiation type	Mo-$K_{\alpha1}$ (λ = 0.71073 Å)
Data collection	
Diffractometer, Monochromator	STOE STADI P diffractometer, Ge111
Refinement	
R_p, R_{wp}	3.239, 4.294
Goodness of fit on F^2	1.219

Table A-7 Fractional atomic coordinates, isotropic displacement parameters (Å^2) and site occupation factors for FeSe(*en*)$_{0.3}$.

Atom	*x*	*y*	*z*	B_{iso}	*occ*
Se1	0	0.1832(3)	0.25	0.96(19)	1
Fe1	0	0.2499(6)	0.75	0.96(19)	0.85
C1	0.19533	0.0035	0.0236	3	0.3333333
N1	0.3404	0.02628	0.69974	3	0.3333333
H1	0.25169	0.03627	0.23167	5	0.3333333
H2	0.30791	0.95879	0.0891	5	0.3333333
H5	0.47118	0.06683	0.76133	5	0.3333333
H6	0.52387	0.99422	0.62774	5	0.3333333

Chemical analysis

The chemical composition of the new compounds was verified by CHN elemental analysis [Table A-8] and energy-dispersive spectroscopy measurements EDS [Table A-9]. The small deviation in C : H : N ratio compared to the formula of *en* $C_2H_8N_2$ is attributed to contamination with residues of acetone C_3H_6O from washing process which could not be fully removed.

Table A-8 C : N : H ratio from elemental analysis normalized to N = 2.

	C	H	N
$Fe_3Se_4(en)_3$	2.1	7.9	2
$Fe_{10}Se_{12}(en)_7$	2.1	8.5	2
FeSe(*en*)$_{0.3}$	2.2	8.8	2

Table A-9 Fe : Se ratio from EDS analysis normalized to Se.

	Fe	**Se**
$Fe_3Se_4(en)_3$	3.30(43)	4
$Fe_{10}Se_{12}(en)_7$	10.60(56)	12
$FeSe(en)_{0.3}$	0.95(7)	1

$FeSe(en)_{0.3}$ was further investigated by Thermogravimetric and ICP-OES analysis. The former showed that deintercalation of *en* starts near 200 °C and is completed at 230 °C under recovery of *β*-FeSe. The liquid section of the decomposed product was subsequently investigated by ^{1}H and ^{13}C NMR which showed pure *en*, thus no other molecular species had been intercalated. A molar ratio of FeSe : *en* = 3 : 1 was observed. ICP-OES analysis yielded a Fe : Se ratio of 0.84(5) : 1 and a FeSe : *en* ratio of 3 : 1. Due to the surface sensitivity of the EDS analysis we consider the ICP-OES results as most reliable and assume a total composition $Fe_{0.85(5)}Se(en)_{0.3}$.

Phase diagram

Table A-10 shows the composition of the products from solvothermal synthesis between 160 °C and 220°C and 0% and 50% *glycerol* content calculated from powder diffraction data by Rietveld refinement.

Table A-10 Composition of the products [in wt%] from solvothermal synthesis at different temperatures and different degrees of dilution with glycerol. Weight percentages were determined by Rietveld refinement from powder diffraction data [Cu-$K_{\alpha 1}$ radiation].

Temperature (°C)	% glycerol	$Fe_3Se_4(en)_3$	$Fe_3Se_4(en)_2$	$Fe_{10}Se_{12}(en)_7$	$FeSe(en)_{0.3}$	β-FeSe	$FeSe_2$	Se	Fe
220	0	-	100	-	-	-	-	-	-
220	20	-	-	26	74	-	-	-	-
220	50	-	-	-	99	-	-	1	-
210	0	-	100	-	-	-	-	-	-
210	20	-	-	100	-	-	-	-	-
210	50	-	-	-	89	9	-	2	-
200	0	-	100	-	-	-	-	-	-
200	5	-	57	43	-	-	-	-	-
200	20	-	-	100	-	-	-	-	-
200	30	-	-	100	-	-	-	-	-
200	50	-	-	-	100	-	-	-	-
190	0	14	57	29	-	-	-	-	-
190	20	-	-	97	-	-	-	3	-
190	50	-	-	13	68	-	17	3	-
190	50	-	-	13	68	-	17	3	-

Table A-10 Continued.

Temperature (°C)	% glycerol	$Fe_3Se_4(en)_3$	$Fe_3Se_4(en)_2$	$Fe_{10}Se_{12}(en)_7$	$FeSe(en)_{0.3}$	β-FeSe	$FeSe_2$	Se	Fe
180	0	60 [g]	6 [g]	34 [g]	-	-	-	-	-
180	20	-	-	100	-	-	-	-	-
180	50	-	-	8	83		9	-	-
170	0	99 [g]	-	-	-	-	-	-	1 [g]
170	20	-	-	(100)	-	-	-	-	-
170	50	-	-	-	94	-	-	6	
160	0	(83) [g]	-	-	-	-	-	(6) [g]	(11) [g]
160	20	-	-	(94)	-	-	-	(6)	-
160	50	-	-	-	74	21	-	4	-

[g] These samples contain a so far unknown phase [see chapter 2.1.1].

Properties

Table A-11 shows the lattice parameters of $Fe_3Se_4(en)_3$, $Fe_3Se_4(en)_2$, $Fe_{10}Se_{12}(en)_7$ and $FeSe(en)_{0.3}$ between 10 K and 290 K from temperature dependent powder diffraction data determined by Rietveld refinement.

Table A-11 Lattice parameters of $Fe_3Se_4(en)_3$, $Fe_3Se_4(en)_2$, $Fe_{10}Se_{12}(en)_7$ and $FeSe(en)_{0.3}$ determined by Rietveld refinement from low temperature powder diffraction data [Co-$K_{\alpha1}$ radiation] between 10 K and 290 K.

	$Fe_3Se_4(en)_3$					
T (K)	*a* (Å)	*b* (Å)	*c* (Å)	*α* (°)	*β* (°)	*γ* (°)
290	9.1246(5)	10.3659(8)	11.6972(13)	109.841(8)	96.443(8)	114.025(5)
270	9.1050(5)	10.3611(7)	11.6974(12)	109.908(7)	96.412(7)	113.962(5)
250	9.0772(5)	10.3621(7)	11.7027(12)	110.001(7)	96.344(7)	113.927(5)
230	9.0728(6)	10.3571(8)	11.6927(11)	110.038(7)	96.302(7)	113.897(5)
210	9.0665(6)	10.3455(9)	11.6885(12)	110.073(8)	96.280(8)	113.813(6)
190	9.0488(6)	10.3413(8)	11.6873(12)	110.118(7)	96.265(7)	113.766(5)
170	9.0292(5)	10.3424(7)	11.6867(10)	110.178(6)	96.230(7)	113.735(5)
150	9.0162(5)	10.3368(7)	11.6861(10)	110.246(7)	96.201(7)	113.681(4)
130	9.0011(5)	10.3287(7)	11.6875(11)	110.304(7)	96.182(8)	113.624(5)
110	8.9875(5)	10.3243(7)	11.6875(10)	110.359(7)	96.176(7)	113.577(5)
90	8.9750(5)	10.3187(7)	11.6888(10)	110.405(7)	96.172(7)	113.534(5)
70	8.9637(5)	10.3153(7)	11.6875(10)	110.463(6)	96.145(7)	113.492(5)
50	8.9532(5)	10.3102(7)	11.6881(11)	110.515(7)	96.130(7)	113.450(5)
30	8.9438(5)	10.3087(7)	11.6932(11)	110.581(7)	96.105(7)	113.412(5)
10	8.9429(5)	10.3126(7)	11.6953(10)	110.599(7)	96.085(7)	113.401(5)

Table A-11 Continued.

$Fe_3Se_4(en)_2$						
T (K)	***a* (Å)**	***b* (Å)**	***c* (Å)**	***α* (°)**	***β* (°)**	***γ* (°)**
290	17.2758(4)	7.9768(2)	11.6789(4)	90	120.938(2)	90
270	17.2742(4)	7.9708(3)	11.6743(5)	90	120.959(3)	90
250	17.2695(4)	7.9652(2)	11.6670(5)	90	120.964(2)	90
230	17.2656(4)	7.9586(2)	11.6590(4)	90	120.976(2)	90
210	17.2653(3)	7.9530(2)	11.6549(4)	90	121.001(2)	90
190	17.2606(3)	7.9493(2)	11.6463(3)	90	121.001(2)	90
170	17.2540(3)	7.9417(2)	11.6398(4)	90	121.011(2)	90
150	17.2451(4)	7.9361(2)	11.6348(4)	90	121.034(2)	90
130	17.2361(4)	7.9292(2)	11.6282(4)	90	121.030(2)	90
110	17.2290(4)	7.9245(2)	11.6240(4)	90	121.046(2)	90
90	17.2231(4)	7.9212(2)	11.6212(4)	90	121.053(2)	90
70	17.2167(4)	7.9174(2)	11.6185(4)	90	121.057(2)	90
50	17.2084(4)	7.9136(2)	11.6127(4)	90	121.058(2)	90
30	17.2060(4)	7.9124(2)	11.6106(4)	90	121.053(2)	90
10	17.2084(4)	7.9131(2)	11.6121(4)	90	121.058(2)	90
$Fe_{10}Se_{12}(en)_7$						
T (K)	***a* (Å)**	***b* (Å)**	***c* (Å)**	***α* (°)**	***β* (°)**	***γ* (°)**
290	9.4176(6)	12.3271(20)	20.9802(20)	90	90	90
270	9.4076(6)	12.3207(23)	20.9684(22)	90	90	90
250	9.3968(6)	12.3125(22)	20.9508(21)	90	90	90
230	9.3847(6)	12.3077(22)	20.9356(22)	90	90	90
210	9.3739(6)	12.3055(22)	20.9176(22)	90	90	90
190	9.3661(6)	12.2986(22)	20.9071(22)	90	90	90
170	9.3597(6)	12.2950(23)	20.8892(22)	90	90	90

Table A-11 Continued.

$Fe_{10}Se_{12}(en)_7$						
T (K)	***a* (Å)**	***b* (Å)**	***c* (Å)**	**α (°)**	**β (°)**	**γ (°)**
150	9.3509(7)	12.2902(24)	20.8730(23)	90	90	90
130	9.3456(7)	12.2978(32)	20.8580(24)	90	90	90
110	9.3407(7)	12.3057(38)	20.8506(24)	90	90	90
90	9.3327(7)	12.3124(43)	20.8430(24)	90	90	90
70	9.3248(7)	12.3128(44)	20.8346(24)	90	90	90
50	9.3186(7)	12.3064(43)	20.8291(24)	90	90	90
30	9.3083(7)	12.3062(41)	20.8231(24)	90	90	90
10	9.3131(7)	12.3074(42)	20.8311(23)	90	90	90
$FeSe(en)_{0.3}$						
T (K)	***a* (Å)**	***b* (Å)**	***c* (Å)**	**α (°)**	**β (°)**	**γ (°)**
290	3.9153(3)	21.5280(17)	3.8603(3)	90	91.354(12)	90
270	3.9133(3)	21.4964(17)	3.8630(3)	90	91.644(13)	90
250	3.9123(3)	21.4632(17)	3.8643(3)	90	91.776(12)	90
230	3.9108(3)	21.4396(16)	3.8652(3)	90	91.795(12)	90
210	3.9095(3)	21.4139(16)	3.8639(3)	90	91.826(12)	90
190	3.9082(3)	21.3886(16)	3.8643(3)	90	91.821(12)	90
170	3.9063(3)	21.3764(16)	3.8634(3)	90	91.808(11)	90
150	3.9044(3)	21.3566(17)	3.8625(3)	90	91.816(12)	90
130	3.9035(3)	21.3374(16)	3.8615(3)	90	91.808(11)	90
110	3.9018(3)	21.3244(16)	3.8597(3)	90	91.820(11)	90
90	3.9002(3)	21.3128(16)	3.8595(3)	90	91.820(11)	90
70	3.8991(3)	21.2995(16)	3.8576(3)	90	91.800(10)	90
50	3.8986(3)	21.2889(16)	3.8578(3)	90	91.807(10)	90
30	3.8982(3)	21.2833(16)	3.8564(3)	90	91.806(10)	90
10	3.8985(3)	21.2727(16)	3.8569(3)	90	91.823(11)	90

Figure A-1 shows the isothermal magnetization curves of $Fe_3Se_4(en)_3$, $Fe_{10}Se_{12}(en)_7$ and $FeSe(en)_{0.3}$ at 1.8 K and between 1 and 5 T with μ in μ_B per formula unit.

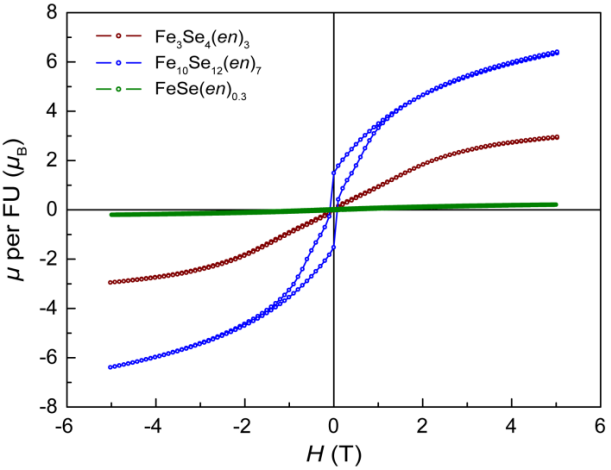

Figure A-1 Isothermal magnetization curves of $Fe_3Se_4(en)_3$, $Fe_{10}Se_{12}(en)_7$ and $FeSe(en)_{0.3}$ at 1.8 K.

A.2 Polymorphism of $Fe_3Se_4(en)_3$

Table A-12 to Table A-14 show the data for the crystal structure solution of β-$Fe_3Se_4(en)_3$.

Table A-12 Crystal data, data collection parameters and refinement parameters for β-$Fe_3Se_4(en)_3$.

Crystal data	
Chemical formula	$Fe_3Se_4C_6H_{24}N_6$
M (g·mol^{-1})	663.7
Crystal system, Space group (No.)	Monoclinic, $P2_1$ (4)
a, b, c (Å)	9.8109(16), 11.4174(14), 16.639(3)
α, β, γ (°)	90, 92.177(8), 90
V (Å^3), ρ_{calc} (g·cm^{-3})	1862.5(5), 2.367
T (K), μ (mm^{-1})	293, 10.12
Z	4
Radiation type	Mo-K_α (λ = 0.71073 Å)
θ range (°)	4.9–29.3
Data collection	
Diffractometer, Monochromator	Bruker CCD diffractometer, graphite
Absorption correction	multi-scan *SADABS* 2014/5
No. of reflections (measured, independent, with I>3σ(I))	53100, 5205, 4400
R_{int}	0.134
Index range	-12 ≤ h ≤ 12, -14 ≤ k ≤ 14, 20 ≤ l ≤ 20
θ range (°)	2.4-26.4

Table A-12 Continued.

Refinement	
Refinement on	F^2
Data, Restraints, Parameters, Constraints	5205, 0, 343, 205
R_1 ($I>2\sigma(I)$), $wR(F^2)$ ($I>2\sigma(I)$)	0.052, 0.095
Goodness of fit on F^2	1.54
$\Delta\rho$ (max; min) ($e\cdot Å^{-3}$)	1.02; -0.82

Table A-13 Fractional atomic coordinates and isotropic or equivalent isotropic displacement parameters ($Å^2$) for β-$Fe_3Se_4(en)_3$.

Atom	***x***	***y***	***z***	U_{iso}*/U_{eq}
Se1	0.41912(16)	0.96520(12)	0.40207(9)	0.0270(5)
Se2	0.32152(15)	0.71503(12)	0.54960(9)	0.0256(5)
Se3	0.65030(15)	0.92638(12)	0.58369(9)	0.0242(5)
Se4	0.62974(16)	0.68050(12)	0.42196(10)	0.0306(5)
Se5	0.17564(16)	0.86940(13)	0.05274(10)	0.0283(5)
Se6	0.98770(16)	0.57591(15)	0.12108(8)	0.0343(5)
Se7	0.15021(16)	0.57744(15)	0.92492(9)	0.0360(5)
Se8	0.8398(2)	0.78833(15)	0.95325(14)	0.0536(7)
Fe1	0.53314(19)	0.0710(2)	0.50582(11)	0.0219(6)
Fe2	0.5045(2)	0.82139(19)	0.49147(13)	0.0210(7)
Fe3	0.9724(2)	0.95137(19)	0.99036(12)	0.0242(7)
Fe4	0.0389(2)	0.70518(19)	0.01407(12)	0.0237(7)
Fe5	0.5725(2)	0.37162(18)	0.18599(12)	0.0261(7)
Fe6	0.9965(2)	0.90505(18)	0.32072(13)	0.0303(8)
N1	0.5165(8)	0.2517(3)	0.0853(3)	0.033(5)
N2	0.4910(6)	0.2185(5)	0.2521(4)	0.032(5)
N3	0.6487(4)	0.4413(8)	0.3013(2)	0.033(5)
N4	0.7943(4)	0.3281(5)	0.1830(5)	0.025(4)
N5	0.6118(4)	0.5261(9)	0.1061(3)	0.047(5)

Table A-13 Continued.

Atom	*x*	*y*	*z*	U_{iso}*/U_{eq}
N6	0.3742(4)	0.4676(4)	0.1908(6)	0.043(5)
N7	0.0531(8)	0.0773(3)	0.2614(3)	0.041(5)
N8	0.0725(10)	0.0126(4)	0.4268(2)	0.058(7)
N9	0.7801(6)	0.9462(3)	0.3453(5)	0.037(5)
N10	0.8869(6)	0.8416(8)	0.21021(16)	0.032(5)
N11	0.0009(10)	0.7375(4)	0.3944(2)	0.042(5)
N12	0.1828(4)	0.8179(2)	0.2770(5)	0.033(5)
C1	0.4784(15)	0.1371(12)	0.1167(7)	0.039(6)
C2	0.4049(14)	0.1484(9)	0.1933(7)	0.033(6)
C3	0.7994(13)	0.4528(15)	0.3012(5)	0.036(6)
C4	0.8565(9)	0.3519(13)	0.2617(9)	0.040(6)
C5	0.4901(17)	0.5916(16)	0.0979(9)	0.103(11)
C6	0.4025(14)	0.5836(18)	0.1591(12)	0.095(10)
C7	0.1342(13)	0.1470(9)	0.3196(9)	0.033(6)
C8	0.0716(15)	0.1369(13)	0.4008(8)	0.042(7)
C9	0.7007(15)	0.9496(8)	0.2665(9)	0.047(7)
C10	0.7417(16)	0.8387(13)	0.2198(7)	0.047(7)
C11	0.0777(17)	0.6528(10)	0.3497(8)	0.046(7)
C12	0.2088(13)	0.7044(10)	0.3199(8)	0.038(6)
H1n1	0.585212	0.240704	0.039839	0.0396*
H2n1	0.429843	0.294412	0.062421	0.0396*
H1n2	0.434397	0.238778	0.301847	0.0379*
H2n2	0.576276	0.169914	0.270431	0.0379*
H1n3	0.606035	0.521035	0.317121	0.0399*
H2n3	0.62254	0.377543	0.342564	0.0399*
H1n4	0.780635	0.238328	0.176092	0.03*
H2n4	0.857353	0.359032	0.138892	0.03*
H1n5	0.588316	0.437615	0.111215	0.0566*
H2n5	0.6698	0.539024	0.055849	0.0566*
H1n6	0.317707	0.475598	0.242152	0.0515*
H2n6	0.31904	0.419354	0.147695	0.0515*

Table A-13 Continued.

Atom	*x*	*y*	*z*	U_{iso}*/U_{eq}
H1n7	0.055824	0.116041	0.204964	0.0487*
H2n7	0.952668	0.073167	0.279193	0.0487*
H1n8	0.986492	0.995902	0.459671	0.0699*
H2n8	0.159713	0.996395	0.462548	0.0699*
H1n9	0.737117	0.884647	0.382792	0.0445*
H2n9	0.880698	0.923338	0.335449	0.0445*
H1n10	0.92252	0.756968	0.201436	0.0378*
H2n10	0.908487	0.893006	0.160675	0.0378*
H1n11	0.926957	0.694443	0.426382	0.0505*
H2n11	0.066583	0.782222	0.434183	0.0505*
H1n12	0.188856	0.805042	0.215343	0.0393*
H2n12	0.086032	0.848299	0.289633	0.0393*
H1c1	0.569717	0.084088	0.127	0.047*
H2c1	0.413438	0.091785	0.072091	0.047*
H1c2	0.387184	0.061552	0.218082	0.039*
H2c2	0.307945	0.192988	0.181621	0.039*
H1c3	0.826285	0.532171	0.268988	0.0436*
H2c3	0.840178	0.457636	0.362965	0.0436*
H1c4	0.965935	0.364175	0.256432	0.0484*
H2c4	0.846959	0.275012	0.299917	0.0484*
H1c5	0.436758	0.56877	0.041406	0.1231*
H2c5	0.514649	0.683332	0.087497	0.1231*
H1c6	0.306803	0.626793	0.141668	0.1139*
H2c6	0.43692	0.641014	0.208095	0.1139*
H1c7	0.133541	0.238465	0.300718	0.0401*
H2c7	0.238313	0.11372	0.323444	0.0401*
H1c8	0.130182	0.189404	0.444535	0.0506*
H2c8	0.966819	0.168861	0.396693	0.0506*
H1c9	0.72921	1.027291	0.232956	0.0561*
H2c9	0.591915	0.946675	0.277331	0.0561*

Table A-13 Continued.

Atom	*x*	*y*	*z*	U_{iso}*/U_{eq}
H1c10	0.715178	0.76102	0.253962	0.0564*
H2c10	0.689431	0.838286	0.160848	0.0564*
H1c11	0.015147	0.621129	0.298658	0.0547*
H2c11	0.101312	0.577246	0.387774	0.0547*
H1c12	0.280282	0.718661	0.370668	0.0459*
H2c12	0.255512	0.642564	0.279262	0.0459*

Table A-14 Atomic displacement parameters (Å^2) for β-$Fe_3Se_4(en)_3$.

Atom	U_{11}	U_{22}	U_{33}	U_{12}	U_{13}	U_{23}
Se1	0.0323(9)	0.0185(9)	0.0301(9)	0.0019(7)	-0.0035(7)	0.0025(7)
Se2	0.0300(9)	0.0174(9)	0.0301(9)	-0.0015(7)	0.0111(7)	-0.0033(7)
Se3	0.0285(9)	0.0159(9)	0.0279(9)	-0.0009(7)	-0.0044(7)	0.0012(7)
Se4	0.0379(10)	0.0146(8)	0.0410(10)	-0.0032(7)	0.0235(8)	-0.0050(7)
Se5	0.0268(9)	0.0256(9)	0.0322(9)	-0.0026(8)	-0.0031(7)	0.0001(8)
Se6	0.0571(10)	0.0225(8)	0.0245(8)	-0.0084(9)	0.0175(7)	-0.0026(8)
Se7	0.0517(10)	0.0236(8)	0.0341(9)	-0.0069(10)	0.0212(8)	-0.0033(9)
Se8	0.0433(12)	0.0231(10)	0.0914(16)	-0.0057(9)	-0.0345(11)	-0.0004(11)
Fe1	0.0276(11)	0.0133(11)	0.0251(11)	-0.0007(11)	0.0053(9)	-0.0007(11)
Fe2	0.0263(12)	0.0138(11)	0.0233(12)	-0.0008(8)	0.0065(9)	-0.0016(9)
Fe3	0.0330(13)	0.0165(13)	0.0232(13)	-0.0002(10)	0.0045(10)	0.0015(10)
Fe4	0.0306(14)	0.0173(12)	0.0237(11)	-0.0007(10)	0.0056(10)	-0.0009(10)
Fe5	0.0325(13)	0.0220(13)	0.0241(12)	-0.0009(11)	0.0047(10)	-0.0019(10)
Fe6	0.0324(14)	0.0267(14)	0.0324(13)	0.0051(10)	0.0082(10)	0.0021(10)
N1	0.024(8)	0.037(9)	0.038(8)	-0.012(6)	0.000(6)	-0.013(6)
N2	0.036(8)	0.025(8)	0.033(8)	0.008(6)	-0.004(6)	-0.013(6)
N3	0.039(8)	0.034(9)	0.029(7)	-0.009(7)	0.020(6)	-0.018(7)
N4	0.029(7)	0.010(7)	0.036(8)	0.006(5)	0.000(6)	-0.008(6)
N5	0.022(8)	0.043(9)	0.077(11)	0.006(6)	0.007(7)	0.040(8)
N6	0.038(9)	0.053(10)	0.038(8)	0.008(7)	0.003(7)	-0.013(8)

Table A-14 Continued.

Atom	U_{11}	U_{22}	U_{33}	U_{12}	U_{13}	U_{23}
N7	0.052(9)	0.030(8)	0.040(8)	-0.012(8)	0.005(7)	0.015(8)
N8	0.029(9)	0.107(15)	0.038(9)	-0.003(9)	-0.004(7)	0.009(9)
N9	0.026(8)	0.051(9)	0.035(8)	0.009(7)	0.016(6)	0.015(7)
N10	0.049(9)	0.027(8)	0.018(7)	0.006(7)	-0.001(6)	-0.001(6)
N11	0.042(9)	0.038(9)	0.046(9)	0.010(7)	0.008(7)	0.024(7)
N12	0.043(8)	0.024(7)	0.032(8)	0.019(6)	0.012(7)	0.000(6)
C1	0.032(10)	0.031(10)	0.054(11)	-0.007(8)	-0.012(8)	-0.023(9)
C2	0.039(10)	0.026(10)	0.034(9)	-0.022(8)	0.013(8)	-0.013(8)
C3	0.036(10)	0.057(12)	0.017(9)	-0.014(9)	0.008(7)	-0.019(9)
C4	0.038(10)	0.038(11)	0.045(11)	0.004(8)	-0.003(8)	-0.006(9)
C5	0.103(19)	0.076(18)	0.13(2)	0.035(17)	0.054(17)	0.068(17)
C6	0.097(18)	0.063(16)	0.13(2)	0.067(15)	0.048(16)	0.047(17)
C7	0.020(9)	0.023(9)	0.055(11)	-0.006(7)	-0.015(8)	0.008(8)
C8	0.031(11)	0.046(12)	0.048(12)	0.011(9)	-0.012(9)	-0.020(9)
C9	0.033(10)	0.066(14)	0.042(11)	-0.020(10)	0.012(8)	0.011(10)
C10	0.045(11)	0.043(12)	0.052(12)	-0.030(9)	-0.005(9)	0.011(9)
C11	0.075(14)	0.007(9)	0.053(12)	0.000(9)	-0.013(10)	0.000(8)
C12	0.038(11)	0.031(10)	0.045(10)	0.009(8)	-0.009(8)	0.002(9)

A.3 Pressure and dilution dependency in the phase diagram of the Fe-Se-*en* system

$Fe_{20}Se_{24}(en)_{13}(MeOH)$

Table A-15 to Table A-17 show the data for the crystal structure solution of $Fe_{20}Se_{24}(en)_{13}(MeOH)$.

Table A-15 Crystal data, data collection parameters and refinement parameters for $Fe_{20}Se_{24}(en)_{13}(MeOH)$.

Crystal data	
Chemical formula	$Fe_{20}Se_{24}C_{27}H_{108}N_{26}O$
M (g·mol^{-1})	3825.3
Crystal system, Space group (No.)	Triclinic; $P\bar{1}$ (2)
a, b, c (Å)	9.23(2), 22.23(5), 24.35(6)
α, β, γ (°)	102.18(7), 99.22(7), 93.62(6)
V (Å^3), ρ_{calc} (g·cm^{-3})	4795(19), 2.650
T (K), μ (mm^{-1})	110, 12.07
Z	2
Radiation type	Mo-K_α (λ = 0.71073 Å)
θ range (°)	4.7–20.3
Data collection	
Diffractometer, Monochromator	Bruker CCD diffractometer, graphite
Absorption correction	multi-scan *SADABS* 2014/5
No. of reflections (measured, independent, with I>3σ(I))	77337, 9861, 6287
R_{int}	0.151
Index range	$-9 \le h \le 9$, $-22 \le k \le 22$, $24 \le l \le 24$
θ range (°)	2.3-20.7

Table A-15 Continued.

Refinement	
Refinement on	F^2
Data, Restraints, Parameters, Constraints	9861, 0, 743, 756
R_1 (I>2σ(I)), $wR(F^2)$ (I>2σ(I))	0.078, 0.151
Goodness of fit on F^2	1.91
$\Delta\rho$ (max; min) (e·Å^{-3})	2.46; -1.90

Table A-16 Fractional atomic coordinates and isotropic or equivalent isotropic displacement parameters for $Fe_{20}Se_{24}(en)_{13}$(MeOH).

Atom	***x***	***y***	***z***	U_{eq}	***occ***
Se1	0.8362(3)	0.49504(12)	0.43439(11)	0.0301(11)	
Se2	0.9799(3)	0.33878(12)	0.47980(11)	0.0324(11)	
Se3	0.2022(3)	0.43589(12)	0.40773(11)	0.0293(10)	
Se4	0.9647(3)	0.49353(12)	0.28206(11)	0.0326(11)	
Se5	0.8229(3)	0.34452(11)	0.32002(11)	0.0268(10)	
Se6	0.1543(3)	0.25419(12)	0.34644(12)	0.0328(11)	
Se7	0.7114(3)	0.35537(12)	0.16416(11)	0.0302(11)	
Se8	0.1201(3)	0.33806(11)	0.21595(11)	0.0274(10)	
Se9	0.8630(3)	0.19504(12)	0.20091(11)	0.0331(11)	
Se10	0.7594(3)	0.40187(12)	0.01739(11)	0.0303(11)	
Se11	0.5275(3)	0.25438(12)	0.01774(11)	0.0294(10)	
Se12	0.9440(3)	0.25204(12)	0.06194(11)	0.0334(11)	
Se13	0.4417(3)	0.32030(12)	0.88021(11)	0.0345(11)	
Se14	0.8162(3)	0.25657(11)	0.90619(11)	0.0309(11)	
Se15	0.6792(3)	0.10550(12)	0.94513(12)	0.0413(12)	
Se16	0.6464(4)	0.28997(12)	0.75479(12)	0.0427(12)	
Se17	0.4993(3)	0.14243(12)	0.79636(11)	0.0336(11)	
Se18	0.8941(3)	0.09799(13)	0.81655(12)	0.0399(12)	
Se19	0.3251(3)	0.16902(15)	0.64965(13)	0.0532(13)	

Table A-16 Continued.

Atom	*x*	*y*	*z*	U_{eq}	*occ*
Se20	0.7299(3)	0.13473(12)	0.66662(11)	0.0305(11)	
Se21	0.6057(3)	0.98288(12)	0.70827(11)	0.0404(12)	
Se22	0.5104(4)	0.15147(12)	0.51029(12)	0.0456(13)	
Se23	0.4080(3)	0.01035(12)	0.56934(11)	0.0295(11)	
Se24	0.8183(3)	0.98339(12)	0.57433(11)	0.0324(11)	
Fe1	0.0409(4)	0.44323(16)	0.47580(15)	0.0257(14)	
Fe2	0.9583(4)	0.44766(16)	0.35974(15)	0.0259(14)	
Fe3	0.0429(4)	0.33925(16)	0.38998(15)	0.0271(15)	
Fe4	0.9066(4)	0.38669(15)	0.24405(15)	0.0264(14)	
Fe5	0.9921(4)	0.27875(16)	0.27127(15)	0.0279(15)	
Fe6	0.9007(4)	0.28060(16)	0.15790(15)	0.0282(15)	
Fe7	0.7451(4)	0.31982(16)	0.06803(15)	0.0270(15)	
Fe8	0.6276(4)	0.31085(16)	0.95453(15)	0.0302(15)	
Fe9	0.7404(4)	0.21202(16)	0.98383(15)	0.0299(15)	
Fe10	0.5964(4)	0.25321(16)	0.83378(15)	0.0311(15)	
Fe11	0.7250(4)	0.14781(16)	0.86706(15)	0.0331(15)	
Fe12	0.5457(4)	0.18651(16)	0.71598(16)	0.0327(16)	
Fe13	0.6831(4)	0.08845(16)	0.74695(15)	0.0328(15)	
Fe14	0.4945(4)	0.12030(17)	0.59789(16)	0.0324(15)	
Fe15	0.6476(4)	0.02537(16)	0.63092(15)	0.0283(15)	
Fe16	0.5803(4)	0.95426(16)	0.51699(15)	0.0283(15)	
Fe17	0.3647(4)	0.11031(16)	0.13866(16)	0.0302(15)	
Fe18	0.2812(4)	0.46870(17)	0.10167(16)	0.0319(15)	
Fe19	0.4271(4)	0.64680(16)	0.41904(16)	0.0335(15)	
Fe20	0.9515(5)	0.08274(19)	0.40133(17)	0.0510(19)	
N1	0.2147(8)	0.0525(8)	0.0634(5)	0.083(11)	
N2	0.1723(8)	0.0913(7)	0.1815(3)	0.048(9)	
N3	0.4775(12)	0.0297(5)	0.1584(4)	0.029(6)	
N4	0.5519(9)	0.1135(5)	0.0891(6)	0.037(7)	
N5	0.4864(14)	0.1733(2)	0.2161(5)	0.040(7)	
N6	0.2909(8)	0.2004(8)	0.12118(18)	0.045(8)	

Table A-16 Continued.

Atom	*x*	*y*	*z*	U_{eq}	*occ*
N7	0.2355(8)	0.56682(8)	0.1266(7)	0.030(7)	
N8	0.0763(6)	0.4542(3)	0.1352(6)	0.030(7)	
N9	0.1526(10)	0.4564(6)	0.01312(8)	0.035(7)	
N10	0.2913(11)	0.36754(9)	0.0654(5)	0.042(8)	
N11	0.4950(11)	0.5059(5)	0.0796(2)	0.028(7)	
N12	0.4384(3)	0.4727(7)	0.1805(5)	0.039(8)	
N13	0.1925(12)	0.6019(3)	0.3920(6)	0.036(5)	0.60(2)
N13'	0.2408(9)	0.6164(6)	0.3426(6)	0.036(5)	0.40(2)
N14	0.3146(8)	0.7227(2)	0.3888(9)	0.033(5)	0.56(2)
N14'	0.2710(7)	0.72083(18)	0.44220(16)	0.033(5)	0.44(2)
N15	0.5907(15)	0.3123(10)	0.49356(10)	0.048(6)	0.60(3)
N15'	0.4178(5)	0.31330(10)	0.49429(6)	0.048(6)	0.40(3)
N16	0.5010(5)	0.4314(7)	0.5399(6)	0.042(6)	0.55(2)
N16'	0.664(2)	0.4169(4)	0.5303(4)	0.042(6)	0.45(2)
N17	0.6601(19)	0.6940(15)	0.4303(7)	0.067(8)	0.58(3)
N17'	0.5779(8)	0.7078(13)	0.38704(7)	0.067(8)	0.42(3)
N18	0.4944(15)	0.60277(18)	0.3367(12)	0.072(7)	0.59(3)
N18'	0.574(6)	0.5774(9)	0.3857(12)	0.072(7)	0.41(3)
N19	0.8952(8)	0.0851(7)	0.4856(3)	0.036(7)	
N20	0.0928(10)	0.1673(4)	0.4539(5)	0.051(8)	
N21	0.0236(17)	0.0876(4)	0.3202(3)	0.047(8)	
N22	0.8358(18)	0.9950(2)	0.3462(2)	0.047(8)	
N23	0.7280(7)	0.1231(8)	0.3847(5)	0.073(11)	
N24	0.4618(5)	0.1762(6)	0.3372(8)	0.070(11)	
N25	0.854(3)	0.6717(5)	0.2330(4)	0.133(13)*	
N26	0.896(2)	0.7624(4)	0.1675(8)	0.169(16)*	
O1	0.3682(5)	0.46861(14)	0.29634(9)	0.067(10)	
C1	0.076(2)	0.0432(14)	0.0832(10)	0.083(11)	
C2	0.0542(19)	0.0617(10)	0.1369(11)	0.048(9)	
C3	0.624(2)	0.0304(7)	0.1418(9)	0.029(6)	

Table A-16 Continued.

Atom	*x*	*y*	*z*	U_{eq}	*occ*
C4	0.6113(17)	0.0508(11)	0.0856(10)	0.037(7)	
C5	0.437(2)	0.2353(11)	0.2169(7)	0.040(7)	
C6	0.401(3)	0.2467(12)	0.1589(7)	0.045(8)	
C7	0.119(2)	0.5696(6)	0.1631(10)	0.030(7)	
C8	0.0083(17)	0.5124(10)	0.1395(9)	0.030(7)	
C9	0.207(2)	0.4025(10)	0.9781(6)	0.035(7)	
C10	0.203(3)	0.3475(7)	0.0072(11)	0.042(8)	
C11	0.614(2)	0.5138(8)	0.1273(9)	0.028(7)	
C12	0.5578(18)	0.5215(11)	0.1843(10)	0.039(8)	
C13	0.116(2)	0.6430(10)	0.3587(10)	0.036(5)	
C14	0.160(2)	0.7131(9)	0.3887(10)	0.033(5)	
C15	0.516(3)	0.3492(11)	0.4542(8)	0.048(6)	
C16	0.550(2)	0.4184(10)	0.4848(11)	0.042(6)	
C17	0.713(3)	0.6710(12)	0.3786(10)	0.067(8)	
C18	0.654(3)	0.6101(12)	0.3469(12)	0.072(7)	
C19	0.012(2)	0.1263(10)	0.5301(7)	0.036(7)	
C20	0.048(3)	0.1831(8)	0.5103(10)	0.051(8)	
C21	0.927(3)	0.0438(11)	0.2739(8)	0.047(8)	
C22	0.899(2)	0.9853(9)	0.2942(9)	0.047(8)	
C23	0.7402(19)	0.1717(12)	0.3581(13)	0.073(11)	
C24	0.610(3)	0.2106(12)	0.3657(13)	0.070(11)	
C25	0.932(6)	0.732(2)	0.254(2)	0.19(2)*	
C26	0.883(4)	0.7860(11)	0.2331(15)	0.104(14)*	
C27	0.472(3)	0.4250(6)	0.3075(5)	0.076(17)	
H1n1	0.218997	0.017533	0.027991	0.0999*	
H2n1	0.221995	0.095126	0.052232	0.0999*	
H1n2	0.149681	0.084432	0.220353	0.0577*	
H2n2	0.183823	0.138416	0.182784	0.0577*	
H1n3	0.489514	0.038035	0.20262	0.0351*	
H2n3	0.418736	0.986677	0.1404	0.0351*	

Table A-16 Continued.

Atom	*x*	*y*	*z*	U_{eq}	*occ*
H1n4	0.527755	0.121813	0.048279	0.0443*	
H2n4	0.63073	0.147796	0.11452	0.0443*	
H1n5	0.394976	0.140652	0.206479	0.048*	
H2n5	0.546476	0.1728	0.255885	0.048*	
H1n6	0.187564	0.20763	0.131792	0.0544*	
H2n6	0.316605	0.156585	0.125524	0.0544*	
H1n7	0.332071	0.592379	0.150262	0.0365*	
H2n7	0.199798	0.585071	0.091431	0.0365*	
H1n8	0.016738	0.421154	0.100946	0.0359*	
H2n8	0.075886	0.438814	0.172727	0.0359*	
H1n9	0.191463	0.496762	0.002691	0.0423*	
H2n9	0.03786	0.451811	0.005137	0.0423*	
H1n10	0.231065	0.355354	0.094742	0.0499*	
H2n10	0.38834	0.346086	0.06731	0.0499*	
H1n11	0.535172	0.492145	0.041848	0.0334*	
H2n11	0.449356	0.547584	0.079992	0.0334*	
H1n12	0.421069	0.470953	0.221293	0.0471*	
H2n12	0.467981	0.430235	0.16054	0.0471*	
H1n13	0.116216	0.576494	0.406777	0.0427*	0.60(2)
H2n13	0.248283	0.572432	0.36623	0.0427*	0.60(2)
H1n13'	0.226789	0.603902	0.29825	0.0427*	0.4023
H2n13'	0.255053	0.577288	0.359173	0.0427*	0.4023
H1n14	0.331212	0.730813	0.349666	0.0395*	0.56(2)
H2n14	0.361016	0.760592	0.421199	0.0395*	0.56(2)
H1n14'	0.213943	0.758789	0.454748	0.0395*	0.4412
H2n14'	0.364237	0.722045	0.47289	0.0395*	0.4412
H1n15	0.545269	0.266502	0.4808	0.0579*	0.60(3)
H2n15	0.702858	0.314574	0.492048	0.0579*	0.60(3)
H1n15'	0.370373	0.268492	0.490052	0.0579*	0.4032
H2n15'	0.368466	0.33127	0.460593	0.0579*	0.4032

Table A-16 Continued.

Atom	*x*	*y*	*z*	U_{eq}	*occ*
H1n16	0.520404	0.478548	0.557889	0.0509*	0.55(2)
H2n16	0.558902	0.40721	0.566961	0.0509*	0.55(2)
H1n16'	0.765434	0.419789	0.516897	0.0509*	0.4458
H2n16'	0.662147	0.454	0.56416	0.0509*	0.4458
H1n17	0.569574	0.718323	0.42166	0.0807*	0.58(3)
H2n17	0.62878	0.657216	0.447503	0.0807*	0.58(3)
H1n17'	0.589547	0.748124	0.372271	0.0807*	0.423
H2n17'	0.482196	0.680855	0.364284	0.0807*	0.423
H1n18	0.457963	0.567922	0.355279	0.0864*	0.59(3)
H2n18	0.454683	0.591064	0.292963	0.0864*	0.59(3)
H1n18'	0.646916	0.577569	0.423029	0.0864*	0.4126
H2n18'	0.484252	0.600796	0.395716	0.0864*	0.4126
H1n19	0.919174	0.039471	0.481187	0.0429*	
H2n19	0.792844	0.089438	0.497986	0.0429*	
H1n20	0.072974	0.202917	0.43285	0.0609*	
H2n20	0.204608	0.161289	0.459147	0.0609*	
H1n21	0.130642	0.074881	0.323304	0.0564*	
H2n21	0.022423	0.131649	0.311939	0.0564*	
H1n22	0.866642	0.961589	0.368736	0.0565*	
H2n22	0.721366	0.991552	0.335601	0.0565*	
H1n23	0.798589	0.090681	0.371001	0.0882*	
H2n23	0.756237	0.139402	0.42866	0.0882*	
H1n24	0.476929	0.135753	0.30915	0.0844*	
H2n24	0.405605	0.165163	0.368142	0.0844*	
H1n25	0.899514	0.648151	0.199161	0.1595*	
H2n25	0.743569	0.675794	0.218794	0.1595*	
H1n26	0.842345	0.790609	0.143457	0.2028*	
H2n26	0.006855	0.764236	0.163654	0.2028*	
H1o1	0.30388	0.472759	0.323952	0.08*	
H1c1	0.986116	0.055999	0.054174	0.0999*	
H2c1	0.028105	0.99541	0.066213	0.0999*	

Table A-16 Continued.

Atom	*x*	*y*	*z*	U_{eq}	*occ*
H1c2	0.998151	0.023543	0.149558	0.0577*	
H2c2	0.960847	0.089389	0.137564	0.0577*	
H1c3	0.6601	0.984027	0.136184	0.0351*	
H2c3	0.702393	0.063245	0.174489	0.0351*	
H1c4	0.719048	0.052557	0.072717	0.0443*	
H2c4	0.539515	0.016281	0.052258	0.0443*	
H1c5	0.340008	0.240015	0.237332	0.048*	
H2c5	0.522773	0.270439	0.242668	0.048*	
H1c6	0.362181	0.292324	0.16146	0.0544*	
H2c6	0.501172	0.248124	0.140648	0.0544*	
H1c7	0.062981	0.611072	0.16163	0.0365*	
H2c7	0.169777	0.569914	0.20677	0.0365*	
H1c8	0.92434	0.512967	0.166408	0.0359*	
H2c8	0.948973	0.514699	0.097658	0.0359*	
H1c9	0.136956	0.389678	0.935993	0.0423*	
H2c9	0.319694	0.414624	0.973282	0.0423*	
H1c10	0.089068	0.333854	0.01003	0.0499*	
H2c10	0.250522	0.309178	0.982974	0.0499*	
H1c11	0.688536	0.55413	0.128469	0.0334*	
H2c11	0.677473	0.474037	0.121709	0.0334*	
H1c12	0.648574	0.51872	0.218084	0.0471*	
H2c12	0.516774	0.566652	0.194774	0.0471*	
H1c13	0.996585	0.632653	0.3541	0.0427*	0.60(2)
H2c13	0.142995	0.634045	0.315977	0.0427*	0.60(2)
H1c13'	0.072959	0.618998	0.388357	0.0427*	0.4023
H2c13'	0.031502	0.639399	0.320858	0.0427*	0.4023
H1c14	0.101837	0.742007	0.363325	0.0395*	0.56(2)
H2c14	0.140908	0.721304	0.432495	0.0395*	0.56(2)
H1c14'	0.062327	0.735022	0.398496	0.0395*	0.4412
H2c14'	0.205582	0.736874	0.359351	0.0395*	0.4412

Table A-16 Continued.

Atom	*x*	*y*	*z*	U_{eq}	*occ*
H1c15	0.39682	0.336622	0.446329	0.0579*	0.60(3)
H2c15	0.559888	0.34092	0.414657	0.0579*	0.60(3)
H1c15'	0.449386	0.345153	0.41206	0.0579*	0.4032
H2c15'	0.61861	0.3283	0.450952	0.0579*	0.4032
H1c16	0.496584	0.446725	0.457691	0.0509*	0.55(2)
H2c16	0.668652	0.43139	0.491173	0.0509*	0.55(2)
H1c16'	0.592092	0.444167	0.456229	0.0509*	0.4458
H2c16'	0.454031	0.434983	0.501718	0.0509*	0.4458
H1c17	0.833394	0.673235	0.387667	0.0807*	0.58(3)
H2c17	0.69767	0.70367	0.351038	0.0807*	0.58(3)
H1c17'	0.780875	0.692482	0.353774	0.0807*	0.423
H2c17'	0.773905	0.668186	0.420159	0.0807*	0.423
H1c18	0.692412	0.600485	0.306154	0.0864*	0.59(3)
H2c18	0.695793	0.57593	0.369889	0.0864*	0.59(3)
H1c18'	0.743192	0.583777	0.333907	0.0864*	0.4126
H2c18'	0.574989	0.613558	0.309466	0.0864*	0.4126
H1c19	0.969899	0.138733	0.570024	0.0429*	
H2c19	0.110037	0.102238	0.536475	0.0429*	
H1c20	0.138093	0.211934	0.541035	0.0609*	
H2c20	0.952368	0.209313	0.507535	0.0609*	
H1c21	0.823316	0.062943	0.263473	0.0564*	
H2c21	0.98201	0.033673	0.236971	0.0564*	
H1c22	0.825916	0.951683	0.260446	0.0565*	
H2c22	0.001504	0.963964	0.301023	0.0565*	
H1c23	0.738856	0.153803	0.31273	0.0882*	
H2c23	0.843507	0.200489	0.377124	0.0882*	
H1c24	0.610225	0.227834	0.411029	0.0844*	
H2c24	0.626487	0.252015	0.349146	0.0844*	
H1c25	0.048774	0.72924	0.253204	0.2332*	
H2c25	0.948704	0.742806	0.301004	0.2332*	

Table A-16 Continued.

Atom	*x*	*y*	*z*	U_{eq}	*occ*
H1c26	0.962353	0.826076	0.252539	0.1246*	
H2c26	0.76704	0.789947	0.236491	0.1246*	
H1c27	0.565281	0.448602	0.340634	0.0913*	
H2c27	0.417006	0.387573	0.322362	0.0913*	
H3c27	0.51254	0.405378	0.268128	0.0913*	

Table A-17 Atomic displacement parameters (Å^2) for $Fe_{20}Se_{24}(en)_{13}$(MeOH).

Atom	U_{11}	U_{22}	U_{33}	U_{12}	U_{13}	U_{23}
Se1	0.0266(17)	0.0342(17)	0.0300(17)	0.0055(13)	0.0072(14)	0.0061(13)
Se2	0.0381(18)	0.0286(17)	0.0340(18)	-0.0001(14)	0.0131(14)	0.0107(14)
Se3	0.0250(16)	0.0300(17)	0.0316(17)	-0.0051(13)	0.0075(13)	0.0046(13)
Se4	0.0437(19)	0.0222(16)	0.0314(17)	-0.0055(14)	0.0096(14)	0.0049(13)
Se5	0.0244(16)	0.0237(15)	0.0315(17)	-0.0047(13)	0.0078(13)	0.0048(13)
Se6	0.0357(18)	0.0284(16)	0.0369(18)	0.0055(14)	0.0117(14)	0.0088(14)
Se7	0.0312(17)	0.0316(17)	0.0267(17)	0.0008(13)	0.0061(14)	0.0038(13)
Se8	0.0254(16)	0.0246(16)	0.0322(17)	-0.0024(13)	0.0080(13)	0.0057(13)
Se9	0.0362(18)	0.0228(16)	0.0380(18)	-0.0050(13)	0.0052(14)	0.0054(13)
Se10	0.0391(18)	0.0234(16)	0.0275(17)	-0.0039(13)	0.0072(14)	0.0051(13)
Se11	0.0314(17)	0.0269(16)	0.0276(17)	-0.0082(13)	0.0030(14)	0.0057(13)
Se12	0.0321(18)	0.0378(18)	0.0287(17)	0.0002(14)	0.0057(14)	0.0049(14)
Se13	0.0421(19)	0.0317(17)	0.0290(17)	0.0053(14)	0.0047(14)	0.0064(13)
Se14	0.0384(18)	0.0246(16)	0.0292(17)	-0.0014(14)	0.0066(14)	0.0056(13)
Se15	0.067(2)	0.0213(16)	0.0331(18)	-0.0079(15)	0.0087(16)	0.0038(14)
Se16	0.074(2)	0.0248(17)	0.0287(18)	-0.0024(16)	0.0136(16)	0.0048(14)
Se17	0.0413(19)	0.0259(16)	0.0317(17)	-0.0035(14)	0.0073(15)	0.0038(13)
Se18	0.042(2)	0.0411(19)	0.0334(18)	0.0121(15)	0.0032(15)	0.0025(14)
Se19	0.047(2)	0.064(2)	0.039(2)	0.0222(17)	-0.0011(16)	-0.0076(17)
Se20	0.0315(17)	0.0254(16)	0.0317(17)	-0.0047(13)	0.0033(14)	0.0037(13)
Se21	0.068(2)	0.0245(16)	0.0275(18)	-0.0045(15)	0.0120(16)	0.0042(13)

Table A-17 Continued.

Atom	U_{11}	U_{22}	U_{33}	U_{12}	U_{13}	U_{23}
Se22	0.074(2)	0.0214(17)	0.0364(19)	-0.0048(16)	-0.0009(17)	0.0064(14)
Se23	0.0301(17)	0.0288(16)	0.0278(17)	-0.0071(13)	0.0070(13)	0.0039(13)
Se24	0.0308(18)	0.0320(17)	0.0322(17)	0.0021(14)	0.0057(14)	0.0025(14)
Fe1	0.023(2)	0.027(2)	0.028(2)	-0.0030(18)	0.0101(18)	0.0064(18)
Fe2	0.027(2)	0.024(2)	0.028(2)	0.0009(18)	0.0077(19)	0.0057(18)
Fe3	0.028(2)	0.027(2)	0.029(2)	0.0018(18)	0.0107(19)	0.0065(18)
Fe4	0.030(2)	0.019(2)	0.028(2)	-0.0028(18)	0.0060(19)	0.0024(18)
Fe5	0.027(2)	0.023(2)	0.033(2)	-0.0041(18)	0.0093(19)	0.0042(19)
Fe6	0.034(2)	0.022(2)	0.026(2)	-0.0034(18)	0.0060(19)	0.0002(18)
Fe7	0.031(2)	0.025(2)	0.025(2)	-0.0035(18)	0.0065(19)	0.0049(18)
Fe8	0.042(3)	0.020(2)	0.028(2)	-0.0051(19)	0.008(2)	0.0049(18)
Fe9	0.039(3)	0.022(2)	0.027(2)	-0.0012(19)	0.004(2)	0.0051(18)
Fe10	0.042(3)	0.023(2)	0.028(2)	-0.0027(19)	0.009(2)	0.0036(18)
Fe11	0.044(3)	0.024(2)	0.029(2)	-0.0001(19)	0.005(2)	0.0030(19)
Fe12	0.038(3)	0.027(2)	0.031(2)	0.003(2)	0.004(2)	0.0041(19)
Fe13	0.044(3)	0.025(2)	0.028(2)	0.001(2)	0.006(2)	0.0036(19)
Fe14	0.034(3)	0.029(2)	0.031(2)	-0.0014(19)	0.005(2)	0.0014(19)
Fe15	0.032(2)	0.022(2)	0.030(2)	-0.0031(18)	0.0084(19)	0.0022(18)
Fe16	0.029(2)	0.024(2)	0.031(2)	-0.0022(18)	0.0044(19)	0.0043(18)
Fe17	0.028(2)	0.027(2)	0.036(3)	-0.0009(19)	0.0060(19)	0.0086(19)
Fe18	0.028(2)	0.030(2)	0.041(3)	-0.0006(19)	0.014(2)	0.0115(19)
Fe19	0.028(2)	0.027(2)	0.045(3)	-0.0068(19)	0.007(2)	0.008(2)
Fe20	0.071(3)	0.050(3)	0.030(3)	0.024(3)	0.001(2)	0.004(2)
N1	0.036(13)	0.15(2)	0.052(15)	-0.038(14)	0.004(11)	0.005(14)
N2	0.018(11)	0.055(14)	0.075(15)	-0.011(9)	0.019(10)	0.018(12)
N3	0.032(10)	0.021(10)	0.034(11)	-0.006(9)	0.004(9)	0.008(8)
N4	0.028(11)	0.037(10)	0.052(12)	-0.006(9)	0.003(9)	0.028(10)
N5	0.041(12)	0.038(11)	0.035(11)	0.011(9)	-0.015(9)	0.010(10)
N6	0.025(11)	0.049(13)	0.066(14)	0.008(9)	0.001(10)	0.026(11)
N7	0.009(9)	0.036(11)	0.047(12)	-0.004(8)	0.003(8)	0.014(9)
N8	0.040(11)	0.036(11)	0.016(10)	0.007(9)	0.003(8)	0.011(9)

Table A-17 Continued.

Atom	U_{11}	U_{22}	U_{33}	U_{12}	U_{13}	U_{23}
N9	0.032(11)	0.026(10)	0.049(12)	-0.007(9)	0.010(9)	0.011(8)
N10	0.049(13)	0.038(11)	0.050(12)	0.022(10)	0.028(10)	0.019(10)
N11	0.034(11)	0.025(10)	0.025(10)	0.001(8)	-0.006(8)	0.016(9)
N12	0.041(12)	0.052(13)	0.032(11)	0.018(9)	0.015(10)	0.015(10)
N13	0.011(7)	0.041(9)	0.056(9)	-0.009(6)	0.001(6)	0.019(7)
N13'	0.011(7)	0.041(9)	0.056(9)	-0.009(6)	0.001(6)	0.019(7)
N14	0.033(8)	0.033(8)	0.029(7)	-0.007(7)	0.005(6)	0.003(6)
N14'	0.033(8)	0.033(8)	0.029(7)	-0.007(7)	0.005(6)	0.003(6)
N15	0.058(10)	0.057(10)	0.032(9)	0.006(8)	0.005(7)	0.016(7)
N15'	0.058(10)	0.057(10)	0.032(9)	0.006(8)	0.005(7)	0.016(7)
N16	0.014(8)	0.031(8)	0.081(11)	-0.005(6)	0.002(7)	0.016(8)
N16'	0.014(8)	0.031(8)	0.081(11)	-0.005(6)	0.002(7)	0.016(8)
N17	0.067(12)	0.046(10)	0.097(14)	-0.006(8)	0.050(10)	0.011(9)
N17'	0.067(12)	0.046(10)	0.097(14)	-0.006(8)	0.050(10)	0.011(9)
N18	0.048(10)	0.096(13)	0.064(12)	-0.025(10)	0.021(9)	0.000(9)
N18'	0.048(10)	0.096(13)	0.064(12)	-0.025(10)	0.021(9)	0.000(9)
N19	0.024(11)	0.041(12)	0.042(12)	0.004(8)	0.003(8)	0.010(9)
N20	0.086(16)	0.028(11)	0.046(12)	0.008(10)	0.026(12)	0.015(10)
N21	0.072(15)	0.034(12)	0.029(11)	0.004(10)	0.005(10)	-0.002(8)
N22	0.020(11)	0.078(15)	0.036(12)	-0.005(10)	0.003(9)	-0.001(11)
N23	0.090(17)	0.048(15)	0.097(19)	0.019(13)	0.048(14)	0.022(12)
N24	0.043(13)	0.067(16)	0.11(2)	0.006(11)	0.025(13)	0.023(14)
O1	0.072(16)	0.041(13)	0.087(17)	-0.014(12)	0.033(13)	0.005(12)
C1	0.036(13)	0.15(2)	0.052(15)	-0.038(14)	0.004(11)	0.005(14)
C2	0.018(11)	0.055(14)	0.075(15)	-0.011(9)	0.019(10)	0.018(12)
C3	0.032(10)	0.021(10)	0.034(11)	-0.006(9)	0.004(9)	0.008(8)
C4	0.028(11)	0.037(10)	0.052(12)	-0.006(9)	0.003(9)	0.028(10)
C5	0.041(12)	0.038(11)	0.035(11)	0.011(9)	-0.015(9)	0.010(10)
C6	0.025(11)	0.049(13)	0.066(14)	0.008(9)	0.001(10)	0.026(11)
C7	0.009(9)	0.036(11)	0.047(12)	-0.004(8)	0.003(8)	0.014(9)

Table A-17 Continued.

Atom	U_{11}	U_{22}	U_{33}	U_{12}	U_{13}	U_{23}
C8	0.040(11)	0.036(11)	0.016(10)	0.007(9)	0.003(8)	0.011(9)
C9	0.032(11)	0.026(10)	0.049(12)	-0.007(9)	0.010(9)	0.011(8)
C10	0.049(13)	0.038(11)	0.050(12)	0.022(10)	0.028(10)	0.019(10)
C11	0.034(11)	0.025(10)	0.025(10)	0.001(8)	-0.006(8)	0.016(9)
C12	0.041(12)	0.052(13)	0.032(11)	0.018(9)	0.015(10)	0.015(10)
C13	0.011(7)	0.041(9)	0.056(9)	-0.009(6)	0.001(6)	0.019(7)
C14	0.033(8)	0.033(8)	0.029(7)	-0.007(7)	0.005(6)	0.003(6)
C15	0.058(10)	0.057(10)	0.032(9)	0.006(8)	0.005(7)	0.016(7)
C16	0.014(8)	0.031(8)	0.081(11)	-0.005(6)	0.002(7)	0.016(8)
C17	0.067(12)	0.046(10)	0.097(14)	-0.006(8)	0.050(10)	0.011(9)
C18	0.048(10)	0.096(13)	0.064(12)	-0.025(10)	0.021(9)	0.000(9)
C19	0.024(11)	0.041(12)	0.042(12)	0.004(8)	0.003(8)	0.010(9)
C20	0.086(16)	0.028(11)	0.046(12)	0.008(10)	0.026(12)	0.015(10)
C21	0.072(15)	0.034(12)	0.029(11)	0.004(10)	0.005(10)	-0.002(8)
C22	0.020(11)	0.078(15)	0.036(12)	-0.005(10)	0.003(9)	-0.001(11)
C23	0.090(17)	0.048(15)	0.097(19)	0.019(13)	0.048(14)	0.022(12)
C24	0.043(13)	0.067(16)	0.11(2)	0.006(11)	0.025(13)	0.023(14)
C27	0.04(2)	0.09(3)	0.09(3)	0.03(2)	0.01(2)	0.01(2)

Chemical analysis

The chemical composition of $Fe_{20}Se_{24}(en)_{13}(MeOH)$ was examined by CHN elemental analysis and energy-dispersive spectroscopy measurements [EDS]. Since no phase pure sample was obtained, the measured CHN values were corrected by the amount of side phase [10 wt% $Fe_3Se_4(en)_3$] determined by Rietveld refinement of powder X-ray diffraction data [see Figure 2-18]. Table A-18 shows the measured and corrected mass fractions compared to the nominal values for $Fe_{20}Se_{24}(en)_{13}(MeOH)$.

Table A-18 Measured and corrected mass fractions [in wt%] from CHN elemental analysis compared to nominal values for $Fe_{20}Se_{24}(en)_{13}(MeOH)$.

	C	H	N
measured	9.15	2.90	10.33
corrected	8.35	2.63	9.40
nominal	8.48	2.85	9.52

For EDS measurements 20 crystals of $Fe_{20}Se_{24}(en)_{13}(MeOH)$ were selected which gave a ratio Fe : Se : N = 22(1) : 24 : 26(12). Due to absorbed oxygen from the atmosphere on the surface of the crystals, the O content could not be determined.

Phase diagram

Solvothermal syntheses with methanol as diluent were carried out between 180 °C and 220°C and 0% and 50% methanol content. Table A-19 shows the composition of the products calculated from powder X-ray diffraction data by Rietveld refinement.

Table A-19 Composition of the products [in wt%] from solvothermal synthesis at different temperatures and different degrees of dilution with methanol. Weight percentages were determined by Rietveld refinement from powder X-ray diffraction data [Cu-$K_{\alpha1}$ or Mo-$K_{\alpha1}$ radiation].

Temperature (°C)	% methanol	α-$Fe_3Se_4(en)_3$	β-$Fe_3Se_4(en)_3$	$Fe_3Se_4(en)_2$	$Fe_{10}Se_{12}(en)_7$	$Fe_{20}Se_{24}(en)_{13}(MeOH)$	$FeSe(en)_{0.3}$	$FeSe_2$
220	0	-	100	-	-	-	-	-
220	10	-	-	43	29	28	-	-
220	20	-	-	4	8	88	-	-
220	50	-	-	-	-	-	100	-
210	0	-	100	-	-	-	-	-
210	10	-	-	86	-	14	-	-
210	20	-	-	28	15	57	-	-
210	50	-	-	12	-	5	78	5
200	0	-	100	-	-	-	-	-
200	10	-	-	87	-	13	-	-
200	20	-	-	19	-	81	-	-
200	30	-	-	44	-	56	-	-
200	50	-	-	30	-	15	55	-

Table A-19 Continued.

Temperature (°C)	% methanol	α-$Fe_3Se_4(en)_3$	β-$Fe_3Se_4(en)_3$	$Fe_3Se_4(en)_2$	$Fe_{10}Se_{12}(en)_7$	$Fe_{20}Se_{24}(en)_{13}(MeOH)$	$FeSe(en)_{0.3}$	$FeSe_2$
190	0	10	-	59	31	-	-	-
190	10	-	-	74	-	26	-	-
190	20	-	-	48	-	52	-	-
190	50	-	-	20	-	41	39	-
180	0	52	5	-	43	-	-	-
180	10	33	-	51	-	16	-	-
180	20	-	-	37	-	63	-	-
180	50	-	-	38	-	47	15	-

Pressure measurement

Table A-20 and Table A-21 show the results of the temperature dependent pressure measurement for 0%, 20%, 40% and 60% of *glycerol* or methanol dilution, respectively. The given values for temperature and pressure were taken within the reaction zone of the high pressure reactor. Recorded pressures were corrected by 0.61 bar, since the setup showed this offset at each measurement. Systematic errors for the absolute values of Δp = 1 bar up to 2 bar and Δp = 0.3 bar above 2 bar are assumed.

Table A-20 Corrected pressure values for glycerol dilution measured in a high pressure reactor. The *en* : *glycerol* ratio [in %] is given at the head of each column.

T (°C)	*p* (bar)			
	100 : 0	80 : 20	60 : 40	40 : 60
150	2.14	1.22	1.22	0.92
155	2.44	1.83	1.22	1.22
160	2.44	2.14	1.53	1.53
165	3.36	2.44	1.83	1.53
170	3.36	2.75	2.14	1.53
175	4.27	3.97	2.75	1.83
180	4.58	4.58	3.05	2.14
185	5.19	5.80	3.66	2.44
190	6.62	6.72	6.10	2.75

Table A-21 Corrected pressure values for methanol dilution measured in a high pressure reactor. The *en* : methanol ratio [in %] is given at the head of each column.

T (°C)	*p* (bar)			
	100 : 0	80 : 20	60 : 40	40 : 60
150	2.14	1.83	3.36	3.97
155	2.44	2.14	3.66	4.88
160	2.44	2.75	4.58	5.49
165	3.36	3.36	4.88	6.41
170	3.36	3.66	6.1	7.63
175	4.27	4.27	6.72	8.85
180	4.58	4.88	7.94	9.77
185	5.19	5.8	9.16	11.29
190	6.62	7.02	-	13.13

A.4 $Fe_{2.3}GeTe$ – a new layered ferromagnetic telluride

Data from single crystal structure determination of $Fe_{2.3}GeTe$ are given in Table A-22 to Table A-24.

Table A-22 Crystal data, data collection parameters and refinement parameters for $Fe_{2.3}GeTe$.

Crystal data	
Chemical formula	$Fe_{2.355}Ge_{0.992}Te$
M (g·mol^{-1})	331.1
Crystal system, Space group (No.)	Trigonal, *P*3*m*1 (164)
a, c (Å)	3.9891(6), 10.766(3)
V (Å^3), ρ_{calc} (g·cm^{-3})	148.37(6), 7.412
T (K), μ (mm^{-1})	293, 30.60
Z	2
Radiation type	Mo-K_α (λ = 0.71073 Å)
θ range (°)	12.4-47.9
Data collection	
Diffractometer, Monochromator	Bruker CCD diffractometer, graphite
Absorption correction	multi-scan *SADABS* 2014/5
No. of reflections (measured, independent, with I>3σ(I))	6185, 400, 347
R_{int}	0.029
Index range	$-7 \le h \le 7$, $-7 \le k \le 6$, $-19 \le l \le 18$
θ range (°)	3.8-39.8

Table A-22 Continued.

Refinement	
Refinement on	F^2
Data, Restraints, Parameters, Constraints	400, 0, 23, 0
R_1 ($I>2\sigma(I)$), $wR(F^2)$ ($I>2\sigma(I)$)	0.030, 0.069
Goodness of fit on F^2	2.21
$\Delta\rho$ (max; min) ($e\cdot Å^{-3}$)	2.29; -3.41

Table A-23 Fractional atomic coordinates, equivalent isotropic displacement parameters ($Å^2$) and site occupation for $Fe_{2.3}GeTe$.

Atom	***x***	***y***	***z***	U_{eq}	***occ***
Te1	2/3	1/3	0.86543(4)	0.01215(12)	
Ge1	0.3599(7)	0.6401(7)	0.61034(10)	0.0150(7)	0.3307(18)
Fe1	0	0	0.73872(9)	0.0118(2)	
Fe2	0	0	0.5	0.0106(3)	
Fe3	2/3	1/3	0.62759(11)	0.0116(3)	0.792(6)
Fe4	0	0	0	0.010(3)	0.125(7)

Table A-24 Atomic displacement parameters ($Å^2$) for $Fe_{2.3}GeTe$.

Atom	U_{11}	U_{22}	U_{33}	U_{12}	U_{13}	U_{23}
Te1	0.01266(15)	0.01266(15)	0.01112(19)	0.00633(8)	0	0
Ge1	0.0109(9)	0.0109(9)	0.0135(4)	-0.0018(6)	0.0020(3)	-0.0020(3)
Fe1	0.0115(3)	0.0115(3)	0.0125(4)	0.00575(14)	0	0
Fe2	0.0098(3)	0.0098(3)	0.0123(5)	0.00489(17)	0	0
Fe3	0.0114(4)	0.0114(4)	0.0118(5)	0.0057(2)	0	0
Fe4	0.013(4)	0.013(4)	0.005(4)	0.0066(18)	0	0

Figure A-2 shows SAED images of two tilt series of an embedded crystal of $Fe_{2.3}GeTe$ in comparison with simulated ED images for the corresponding zone axis. Very weak diffuse intensities along [001]* and occasional additional reflections are observed.

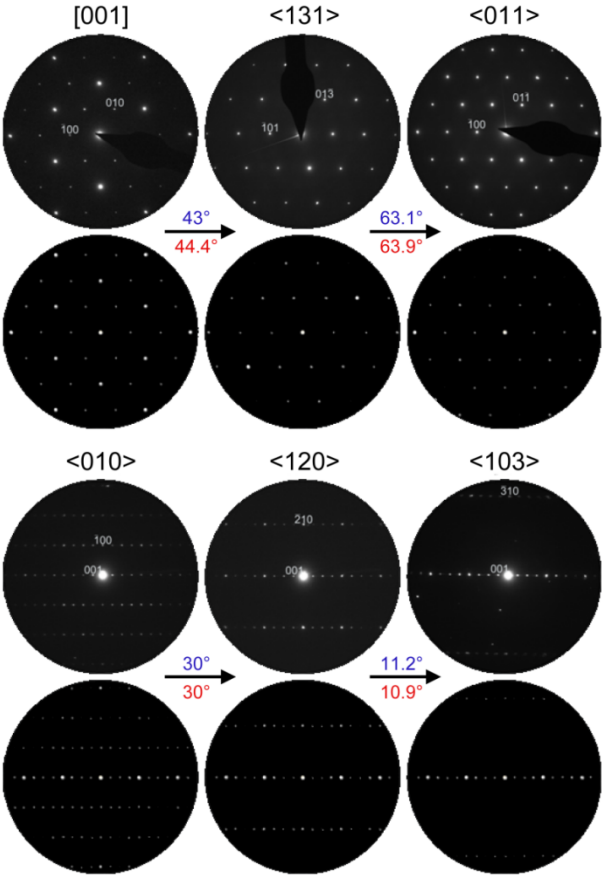

Figure A-2 Experimental SAED patterns [top] along different zone axis compared with simulated ED patterns [bottom] of an embedded crystal of $Fe_{2.3}GeTe$ with experimental tilt angles given in blue and tilt angles based on the structure model given in red.

A.5 The van der Waals Ferromagnets $Fe_{5-\delta}GeTe_2$ and $Fe_{5-\delta-x}Ni_xGeTe_2$ – Crystal Structure, Stacking Faults, and Magnetic Properties

Crystal structure

Data from single crystal structure determination of $Fe_{5-\delta}GeTe_2$ are given in Table A-25 to Table A-27.

Table A-25 Crystal data, data collection parameters and refinement parameters for $Fe_{5-\delta}GeTe_2$.

Crystal data	
Chemical formula	$Fe_{4.623}GeTe_2$
M (g·mol^{-1})	586
Crystal system, Space group (No.)	Trigonal, *R*3*m* (160)
a, c (Å)	4.0376(4), 29.194(6)
V (Å^3), ρ_{calc} (g·cm^{-3})	412.16(10), 7.082
T (K), μ (mm^{-1})	293, 27.54
Z	3
Radiation type	Mo-K_α (λ = 0.71073 Å)
θ range (°)	8.4-55.5
Data collection	
Diffractometer, Monochromator	Bruker CCD diffractometer, graphite
Absorption correction	multi-scan *SADABS* 2014/5
No. of reflections (measured, independent, with I>3σ(I))	3184, 579, 512
R_{int}	0.038
Index range	$-6 \le h \le 5$, $-6 \le k \le 6$, $-47 \le l \le 47$
θ range (°)	4.2-35.6

Table A-25 Continued.

Refinement	
Refinement on	F^2
Data, Restraints, Parameters, Constraints	579, 0, 28, 3
R_1 (I>2σ(I)), $wR(F^2)$ (I>2σ(I))	0.036, 0.080
Goodness of fit on F^2	2.06
$\Delta\rho$ (max; min) (e·Å^{-3})	3.76; -1.90

Table A-26 Fractional atomic coordinates, equivalent isotropic displacement parameters (Å^2) and site occupation for $Fe_{5-\delta}GeTe_2$.

Atom (layer)	***x***	***y***	***z***	U_{eq}	*occ*
Te1 (A')	0	0	0.2795(1)	0.016(1)	1
Te2 (A)	2/3	1/3	0.0509(1)	0.016(1)	1
Ge1 (C)	1/3	2/3	0.1516(2)	0.011(1)	0.5
Ge1' (C)	1/3	2/3	0.1733(2)	0.011(1)	0.5
Fe1 (B)	0	0	0.1031(1)	0.024(1)	1
Fe2 (B)	0	0	0.1895(1)	0.015(1)	1
Fe3 (C)	2/3	1/3	0.1415(1)	0.017(1)	0.898(14)
Fe4 (D)	2/3	1/3	0.2294(2)	0.026(1)	1
Fe5 (D)	1/3	2/3	0.2377(1)	0.008(1)	0.725(7)

Table A-27 Atomic displacement parameters (Å^2) for $Fe_{5-\delta}GeTe_2$.

Atom (layer)	U_{11}	U_{22}	U_{33}	U_{12}	U_{13}	U_{23}
Te1 (A')	0.0153(4)	0.0153(4)	0.0169(6)	0.0077(2)	0	0
Te2 (A)	0.0156(4)	0.0156(4)	0.0167(6)	0.0078(2)	0	0
Ge1 (C)	0.0080(3)	0.0080(3)	0.0163(15)	0.0040(2)	0	0
Ge1' (C)	0.0080(3)	0.0080(3)	0.0163(15)	0.0040(2)	0	0
Fe1 (B)	0.0290(12)	0.0290(12)	0.0145(15)	0.0145(6)	0	0
Fe2 (B)	0.0191(11)	0.0191(11)	0.0067(13)	0.0096(6)	0	0
Fe3 (C)	0.0167(14)	0.0167(14)	0.0159(19)	0.0084(7)	0	0
Fe4 (D)	0.0296(11)	0.0296(11)	0.0187(15)	0.0148(6)	0	0
Fe5 (D)	0.0056(7)	0.0056(7)	0.0127(14)	0.0028(4)	0	0

The 0*kl* and *h*0*l* plane single crystal diffraction patterns in Figure A-3 show distinct streaks along [001] due to stacking disorder.

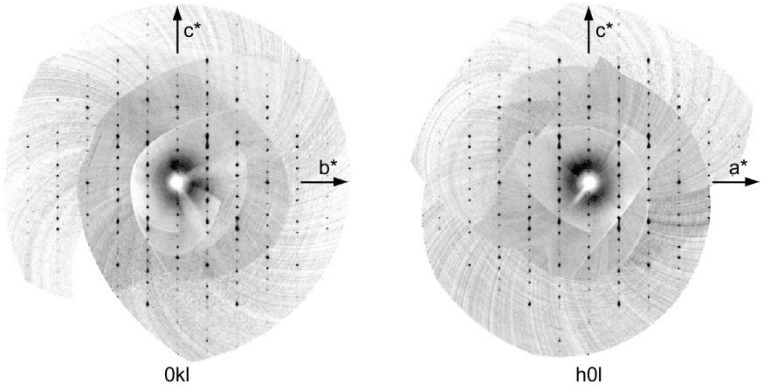

Figure A-3 0*kl* and *h*0*l* plane diffraction patterns.

Figure A-4 to Figure A-6 show the Rietveld refinement plots of the powder diffraction patterns [Mo-$K_{\alpha 1}$ radiation] for all samples of the solid solution $Fe_{5-\delta-x}Ni_xGeTe_2$. The given stoichiometry corresponds to the result of the EDS analysis [see Table A-28]. The amount of Ni substitution for the side phases $Fe_{3-y}Ni_yGeTe2$ is not determined.

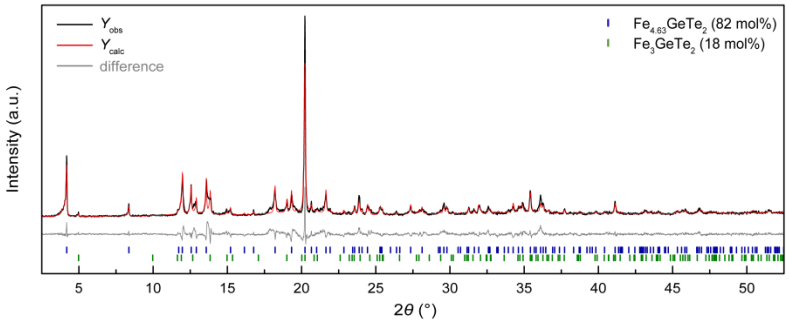

Figure A-4 Rietveld refinement of a powder diffraction pattern [Mo-$K_{\alpha 1}$ radiation] of $Fe_{4.63}GeTe_2$ [blue positions], with Fe_3GeTe_2 [green positions] as side phase.

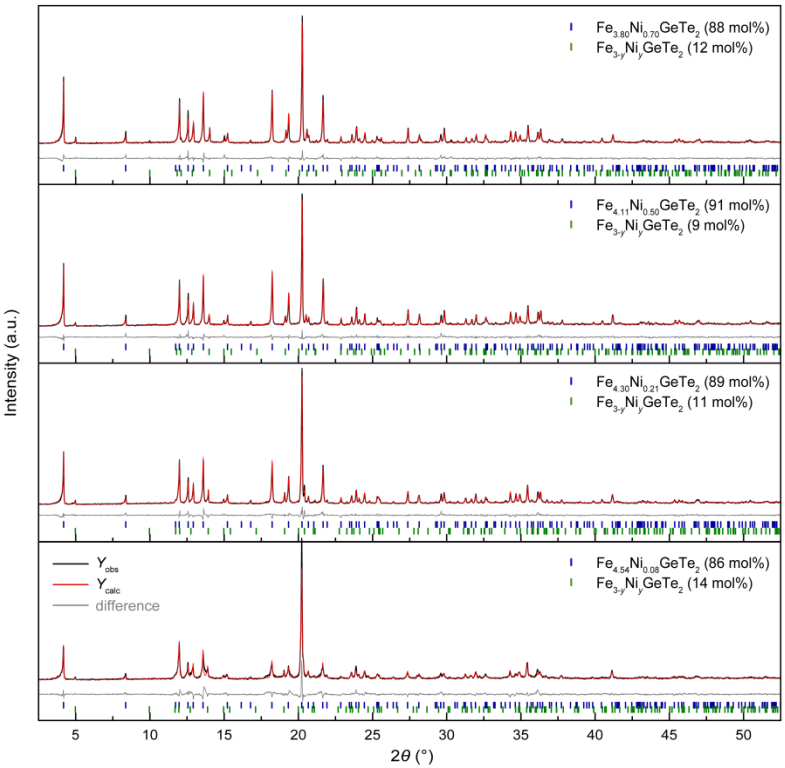

Figure A-5 Rietveld refinements of powder diffraction patterns [Mo-$K_{\alpha 1}$ radiation] of $Fe_{5-\delta-x}Ni_xGeTe_2$ with x = 0.08, 0.21, 0.50 and 0.70 [from bottom to top; blue positions], with $Fe_{3-y}Ni_yGeTe_2$ [green positions] as side phase.

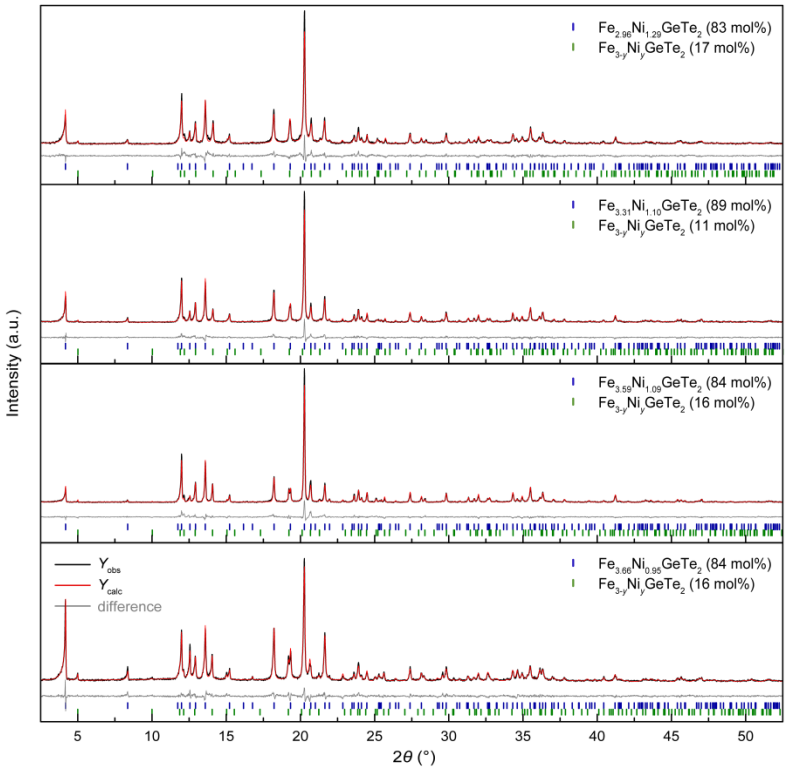

Figure A-6 Rietveld refinements of powder diffraction patterns [Mo-$K_{\alpha 1}$ radiation] of $Fe_{5-\delta-x}Ni_xGeTe_2$ with x = 0.95, 1.09, 1.10 and 1.29 [from bottom to top; blue positions], with $Fe_{3-y}Ni_yGeTe_2$ [green positions] as side phase.

The compositions of the $Fe_{5-\delta-x}Ni_xGeTe_2$ samples from EDS measurement are given in Table A-28 in comparison to the nominal values. For Ge a deviation of about 0.1 is observed, however, this phenomenon is known for similar compounds of the Fe-Ge-Te system. No occupational deficiency of the Ge site is found in powder or single crystal diffraction for various samples.

Table A-28 Composition of the samples $Fe_{5-\delta-x}Ni_xGeTe_2$ from EDS measurement [20-25 data points] normalized to Te = 2.

Fe		Ni		Ge		Te	
nominal	EDS	nominal	EDS	nominal	EDS	nominal	EDS
4.5	4.63(14)	0	0	1	0.93(5)	2	2
4.4	4.54(16)	0.1	0.08(1)	1	0.93(5)	2	2
4.25	4.30(13)	0.25	0.21(2)	1	0.92(4)	2	2
4.0	4.11(13)	0.5	0.50(4)	1	0.90(4)	2	2
3.75	3.80(20)	0.75	0.70(5)	1	0.90(4)	2	2
3.5	3.66(13)	1.0	0.95(5)	1	0.93(6)	2	2
3.4	3.59(12)	1.1	1.09(13)	1	0.96(5)	2	2
3.25	3.31(21)	1.25	1.10(9)	1	0.90(5)	2	2
3.0	2.96(20)	1.5	1.29(9)	1	0.87(5)	2	2

Stacking disorder

One block ABCBDA' of the $Fe_{5-\delta}GeTe_2$ structure was used as base layer for construction of different stacking variants. Lattice parameters and occupation of the base layer were extracted from Rietveld refinement of the measured powder pattern and atom coordinates and equivalent isotropic displacement were taken from single crystal refinement [Table A-29].

Table A-29 Structure data for the base layer used for stacking variants.

Crystal data		Atom	*x*	*y*	*z*	U_{eq} (Å^2)	*occ*
Crystal system	Trigonal	Te1	0	0	0.8384	0.016(1)	1
a (Å)	4.0387	Te2	2/3	1/3	0.1528	0.016(1)	1
c (Å)	9.7234	Ge1	1/3	2/3	0.4547	0.011(1)	0.5
Unit cell volume (Å^3)	137.35	Ge1'	1/3	2/3	0.5199	0.011(1)	0.5
Space group	*P*1	Fe1	0	0	0.3094	0.024(1)	1
Z	1	Fe2	0	0	0.5686	0.015(1)	1
		Fe3	2/3	1/3	0.4244	0.017(1)	0.95
		Fe4	2/3	1/3	0.6882	0.026(1)	1
		Fe5	1/3	2/3	0.7132	0.008(1)	0.71

To determine the stacking disorder, powder patterns were first simulated with increasing S2 stacking up to 40%, which are shown left in Figure A-7 in comparison to a measured pattern. Thereby, the blue line depicts the simulation of the ordered [faultless] structure with only S1 stacking. Based on the shoulders of the 10*l* and 01*l* reflections in the measured pattern together with the broadening of these reflections with increasing number of *stacking faults*, an occurrence of domains with different probabilities is assumed for $Fe_{5-\delta}GeTe_2$. Due to the broadness of

the shoulders, a combination of faultless domains and domains with 20% S2 stacking is considered. To determine the ratio of the domains, simulations with different ratios were compared to the measured diffraction pattern [Figure A-7 right]. For this, the transition probabilities between the domains used for DIFFaX were chosen such that the domain sizes correspond at least to the coherence length of the X-ray radiation [> 1µm]. Otherwise domains would not be visible in the powder diffractograms. As can be seen from Figure A-7, the most fitting description of the experimental data is obtained at a ratio of faultless domains : 20% faulted domains = 1 : 2.

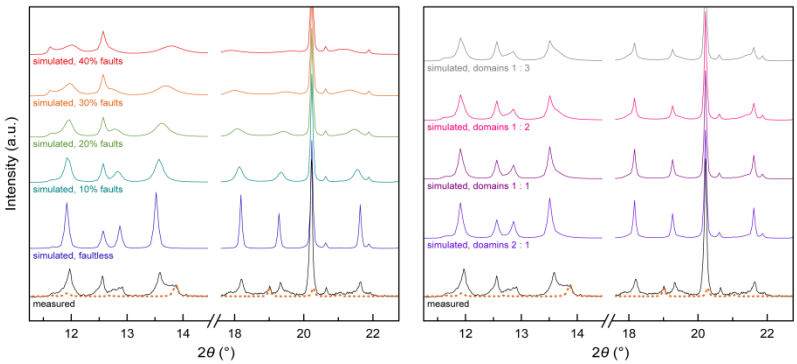

Figure A-7 Excerpts of simulated powder patterns with differing percentage of S2 stacking [left] and differing ratio of faultless : 20% faulted domains [right] in comparison to a measured powder pattern [Mo-$K_{\alpha 1}$ radiation] with side phase Fe_3GeTe_2 given in orange dashed line.

Magnetic properties

The Curie temperatures T_C of the solid solutions $Fe_{5-\delta-x}Ni_xGeTe_2$ were taken from the points of inflection of susceptibility measurements at 100 Oe [Figure A-8 left]. For this, the data was derived twice and the zero points were determined. $Fe_{5-\delta-x}Ni_xGeTe_2$ with increased δ [x = 1.1 and 1.3] are already ordered above the measured temperature range (1.8-400 K). Isothermal magnetization curves at 400 K [Figure A-8 right] show ferromagnetic hysteresis with μ = 0.35 μ_B for x = 1.1 and μ = 0.71 μ_B for x = 1.3 per Fe atom at 50 kOe. Saturation of the magnetic moment is not achieved up to 50 kOe and additionally a splitting of the curves is observed, which settles at repeated measurements. This indicates that the curves were measured close to the magnetic ordering temperature.

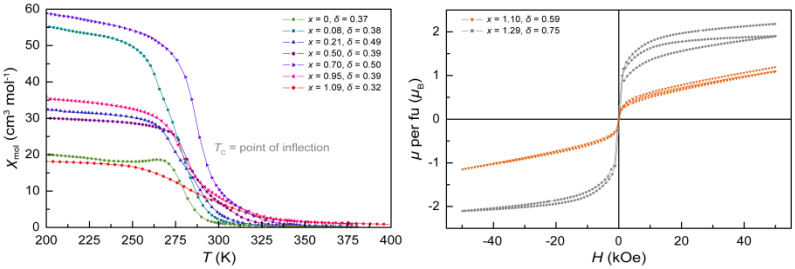

Figure A-8 Left: Magnetic susceptibility of $Fe_{5-\delta-x}Ni_xGeTe_2$ [x = 0-1.1] measured at 100 Oe. Right: Isothermal magnetization per formula unit of $Fe_{5-\delta-x}Ni_xGeTe_2$ [x = 1.1-1.3] measured at 400 K.

A.6 CCDC Numbers

Crystallographic information files [CIF] of the investigated structures in this thesis have been deposited with the Cambridge Crystallographic Data Centre [CCDC]. Copies of the data can be obtained on quoting the depository numbers in Table A-30.

Table A-30 Deposition numbers for the Cambridge Crystallographic Data Centre.

Compound	Deposition Number
α-$Fe_3Se_4(en)_3$	1813199
β-$Fe_3Se_4(en)_3$	1953047
$Fe_{10}Se_{12}(en)_7$	1813200
$FeSe(en)_{0.3}$	1553156
$Fe_{20}Se_{24}(en)_{13}(MeOH)$	1953049
$Fe_{2.3}GeTe$	1953048
$Fe_{4.6}GeTe_2$	1874246

Scientific Contributions

Publications within this thesis

Systematic dimensional reduction of the layered β-FeSe structure by solvothermal synthesis

Juliane Stahl, Evgeniya Shlaen, Helena Singer and Dirk Johrendt

Dalton Transactions **2018**, *47*, 3264-3271.

$Fe_{2.3}GeTe$ – a new layered ferromagnetic telluride [*abstract*]

Juliane Stahl, Lukas Neudert, Oliver Oeckler and Dirk Johrendt

Zeitschrift für Anorganische und Allgemeine Chemie **2016**, *642*, 989–996.

The van der Waals Ferromagnets $Fe_{5-\delta}GeTe_2$ and $Fe_{5-\delta-x}Ni_xGeTe_2$ – Crystal Structure, Stacking Faults, and Magnetic Properties

Juliane Stahl, Evgeniya Shlaen and Dirk Johrendt

Zeitschrift für Anorganische und Allgemeine Chemie **2018**, *644*, 1923-1929.

Publications beyond this thesis

Orange-Emitting $Li_4Sr_4[Si_4O_4N_6]O:Eu^{2+}$ - a Layered Lithium Oxonitridosilicate Oxide

Robin Niklaus, Lukas Neudert, Juliane Stahl, Peter J. Schmidt and Wolfgang Schnick

Inorganic Chemistry **2018**, *57*, 14304-14313.

Na_3GaF_6 – A crystal chemical and solid state NMR spectroscopic study

David Böhnisch, Stefan Seidel, Christopher Benndorf, Thomas Jansen, Lena Funke, Rolf-Dieter Hoffmann, Lukas Heletta, Juliane Stahl, Dirk Johrendt, Hellmut Eckert, Thomas Jüstel and Rainer Pöttgen

Zeitschrift für Kristallographie - Crystalline Materials **2018**, *233*, 479-487.

Abrupt Europium Valence Change in $Eu_2Pt_6Al_{15}$ around 45 K

Mathis Radzieowski, Frank Stegemann, Theresa Block, Juliane Stahl, Dirk Johrendt and Oliver Janka

Journal of the American Chemical Society **2018**, *140*, 8950-8957.

Extended magnetic dome induced by low pressures in superconducting $FeSe_{1-x}S_x$

Stefan Holenstein, Juliane Stahl, Zurab Shermadini, Gediminas Simutis, Vadim Grinenko, Dmitriy A. Chareev, Rustem Khasanov, Jean-Christophe Orain, Alex Amato, Hans-Henning Klauss, Elvezio Morenzoni, Dirk Johrendt, and Hubertus Luetkens

Physical Review Letters **2019**, *123*, 147001.

Temperature Induced Valence Phase Transition in Intermediate-Valent $YbPd_2Al_3$

Frank Stegemann, Juliane Stahl, Simon Gausebeck, Manfred Bartsch, Hellmut Zacharias, Dirk Johrendt and Oliver Janka

Chemical Science **2019**, *10*, 11086-11094.

Conference contributions

Das Fe-Ge-Te-System - Strukturen und Eigenschaften [*talk*]

Juliane Stahl, Lukas Neudert, Vladimir Pomjakushin, Oliver Oeckler and Dirk Johrendt

2. Obergurgl-Seminar Festkörperchemie, Obergurgl, Austria, **2016**.

Superconductivity and Crystal Structures in Solvothermally Synthesized Fe*X* and [(Li,Fe)OH]Fe*X* (*X*= S, Se) [*invited talk*]

Ursula Pachmayr, Juliane Stahl and Dirk Johrendt

MRS Spring Meeting & Exhibit, Phoenix, Arizona, USA, **2016**.

$Fe_{2.3}GeTe$ – a new layered ferromagnetic telluride [*poster*]

Juliane Stahl, Lukas Neudert, Oliver Oeckler and Dirk Johrendt

18. Vortragstagung Fachgruppe Festkörperchemie und Materialforschung der GDCh, Innsbruck, Austria, **2016**.

Solvothermalsynthese von Fe-Se-*en*-Verbindungen [*talk*]

Juliane Stahl and Dirk Johrendt

Hirschegg-Seminar Festkörperchemie, Hirschegg, Austria, **2017**.

Control over tetrahedra connectivity by dilution of the solvent in solvothermal synthesis [*poster*]

Juliane Stahl and Dirk Johrendt

16th European Conference on Solid State Chemistry, Glasgow, UK, **2017**.

Fe_5GeTe_2 - zwei Jahre später [*talk*]

Juliane Stahl and Dirk Johrendt

3. Obergurgl-Seminar Festkörperchemie, Obergurgl, Austria, **2018**.